Title

Relaxation, Data Processing, and Confinement: Spanning the Spectrum of NMR Problems

Author

Parziale, Matthew James

Publication Date

2024

Peer reviewed|Thesis/dissertation

Relaxation, Data Processing, and Confinement:
Spanning the Spectrum of NMR Problems

By

MATTHEW JAMES PARZIALE

DISSERTATION

Submitted in partial satisfaction of the requirements for the degree of

DOCTOR OF PHILOSOPHY

in

Chemistry

in the

OFFICE OF GRADUATE STUDIES

of the

UNIVERSITY OF CALIFORNIA

DAVIS

Approved:

Matthew Augustine, Chair

Michael McCarthy

Kyle Crabtree

Committee in Charge

2024

Abstract

Several topics in the realm of Nuclear Magnetic Resonance (NMR) spectroscopy are discussed in this dissertation. These topics can be divided into two major sections. The first section considers the treatment of data from standard NMR relaxation and diffusion experiments. The current standard for the analysis of transients in low-field NMR is the Inverse Laplace Transform (ILT). Often leading to an inconsistency in the stability of results, the ILT tends to be an ill-posed problem like many other inversion methods. Alternative data processing methods have recently been introduced in an attempt to improve the resolution, stability, and accuracy of results for both discrete and continuous sets of recovered constants.

The application of the Matrix Pencil Method (MPM), a generalized eigenvalue-based algorithm, to NMR transients has recently gained traction as a reliable processing method with low computational costs. Here, the MPM is first extended to the resolution and quantitative analysis of multiple longitudinal (T_1) relaxation components from data acquired by a stray-field sensor. A comparison of MPM to ILT is conducted by testing several combinations of Gd^{3+}-doped 0.9% saline samples with an array of concentrations. It is shown that MPM not only has a greater ability to resolve than ILT at low SNR, but the resulting time constants and relative component weights are also closer to their expected values.

The results of the stray-field study brings about two questions: What are the true limitations of the MPM resolution capabilities and how can experiments be optimized to gain the most information possible from the data? The MPM provides exact solutions for noise-free transients with few discrete components. These solutions increasingly deviate as the SNR of the transient decreases. Numerical and analytical methods are developed to use this knowledge at a given SNR to predict the prime sampling interval to obtain the maximum resolution and accuracy possible.

The second major section concerns the effects of spatial confinement on diffusion and chemical exchange. Two-site exchange has been exhaustively studied and its dynamics are well understood. Three-site exchange, on the other hand, is a drastically different story. Recent kinetics studies on three-site systems have revealed asymmetric exchange behavior when subjected to restrictive environments. This asymmetry

is indicative of a violation of detailed balance which states that all pairs of relaxation sites should experience equivalent exchange at thermal equilibrium. An investigation on the effects of confinement on three-site exchange is conducted using two 2D numerical methods, a Monte-Carlo vacancy diffusion simulation and a molecular dynamics gas diffusion simulation with elastic particles. These simulations reveal that this asymmetry indeed arises when the diffusive motion is driven away from standard Brownian dynamics. Under this driven equilibrium, a circular flux between relaxation sites develops which goes against detailed balance. The cyclical diffusive behavior potentially arises from the excitation of the diffusive eigenmodes of a pore.

Table of Contents

Acknowledgements

First and foremost, I need to thank my mom and brother for their continuous support through this journey. From poverty to never-ending health struggles, I know the last 20 years have been brutal for the three of us, but we are slowly making our way out of the trenches. Thank you, mom, for the countless sacrifices you have made to give Jason and me an opportunity to progress in life. None of my accomplishments would have been possible without you.

I owe a great deal of thanks to my advisor, Dr. Matt Augustine. Thank you for taking me into your group and introducing me to the wonderland that is low field NMR. I know it is often hard to read my emotions, but I truly enjoy our late night scientific discussions when we both refuse to leave the lab. The excitement for science that you exude is inspiring and I always look forward to the next experiment that pops into your head. I am ready to head back into the lab and grind out those projects.

To my wonderful girlfriend, Mary, thank you for all the love and support you have given me in these last 2 years. The amount of patience you have demonstrated with me is nothing short of astonishing. You are always there to remind me that I should be doing my work instead of sleeping. I promise that a black cat is in our future, and he shall be dubbed *Void*. I look forward to annoying you for many years to come, my best friend!

Of course, I need to thank the man that brought me to Davis in the first place, Dr. David Saiki. Before I met you, graduate school never even crossed my mind. But you gave me my first real taste of spectroscopy, and then my trajectory was set. The amount of passion you put into discussing physical chemistry topics was enough for me to finally figure out what I wanted to do. After years of working with Matt, I can see where that enthusiasm comes from.

Finally, I would like to thank the current and past members of the Augustine group. The Augustine group has been home to some of the coolest nerds that I've ever met. From the sage wisdom of Javier to the objectively great taste in music of Brandon, to the intellectual curiosity of Sophia and Dan, you have all made the graduate experience an interesting one. Thank you to Julia and Sam who really helped bring me out of my introverted shell. I couldn't have picked a better lab.

Chapter 1: The Essence of NMR and Relaxation

1.1 Introduction

From the humble one-dimensional proton spectrum of simple organic molecules to the convoluted multi-dimensional transients of complex systems, nuclear magnetic resonance (NMR) spectroscopy has long been used as a ubiquitous analytical tool in the physical and biological sciences [1-3]. New hardware developments are rapidly pushing NMR at low magnetic fields out of the lab and into nature [4]. NMR often lacks the spectral resolution required for structure elucidation at these weak magnetic field strengths. However, the utility of the technique is not lost as a trove of information on the dynamics and chemical landscape of a system can be recovered from various experiments. The following chapter aims to give the foundational knowledge necessary to understand the significance of the parameters to be considered throughout the data processing portion of this dissertation. This chapter is also intended to serve as a bridge to the discussion of diffusion and exchange in the latter chapters.

1.2 Tiny Magnets in a Polarizing World

The most basic of NMR experiments can be broken down into two simple steps – an initial perturbation of the sample by an external magnetic field followed by an excitation by radiofrequency radiation. Development of this technique was driven by a few experiments spanning over twenty years [5].

1.2.1 Quantization of Angular Momentum and the Stern-Gerlach Experiment

At the onset of the 20th century, Arnold Sommerfeld proposed an amendment to Niels Bohr's model of electrons circularly orbiting the nucleus of an atom [6]. By confining the number of possible orientations of the z-component of angular momentum, the model for electron motion could also encompass elliptical orbits. Electrons at the same principal energy level with different orbits could possess the same energies unless perturbed by an additional force. This theoretical extension brought about the concept of

quantum degeneracy and allowed for further explanation of the fine structure that appeared in atomic Hydrogen spectra.

In the early 1920's, Otto Stern and Walther Gerlach developed an apparatus to explore this theory of "space quantization" that would help lead to an unintended realization [7-9]. The experimental method was simple: generate a beam of electrically neutral silver atoms, pass the beam through an inhomogeneous magnetic field, and detect the atoms on a screen following deflection. If angular momentum is quantized, the magnetic dipole arising from the orbital angular momentum of the single unpaired electrons would deflect the atoms in one of two directions on the experimental z-axis, up or down. The results showed the beam split in two producing two separate bands on the screen. "Space quantization" was successfully proven and appeared to verify the Bohr-Sommerfeld model.

While this theory was proven to be correct in general, the assertion that the partisan deflection occurred due to the orbital angular momentum of the unpaired silver electron was not. The number of degenerate states for any angular momentum quantum number (J) was later predicted to be $2J+1$. The unpaired electron in silver was later discovered to possess no orbital angular momentum meaning that it did not have any degenerate orbits. If the beam splitting did not come from the orbital angular momentum, it must come from another source of angular momentum with $J = 1/2$. This angular momentum was formally postulated to be an intrinsic property of both elementary and composite quantum particles with no classical analogue by George Uhlenbeck and Samuel Goudsmit [10]. A heavily scrutinized concept suggested by Ralph Kronig just months prior, it was suggested that electrons rotate in space generating a magnetic dipole moment just as orbital angular momentum does for a point charge [11]. While is it now understood that these quantum particles are not really rotating, this intrinsic angular momentum has been dubbed "spin" and it is at the core of all of magnetic resonance.

1.2.2 Zeeman Splitting and Larmor Precessions

The Stern-Gerlach experiment is a direct application of the anomalous Zeeman effect [12]. In the presence

of an external magnetic field, the energy of the interaction with a magnetic dipole moment ($\vec{\mu}$) can be described by the classical equation

$$E = -\vec{\mu} \cdot \vec{B}. \tag{1.1}$$

Equation. 1.1 can be translated to a relevant quantum variant via the Wigner-Eckart theorem which states that there is a scalar relationship between the magnetic dipole and angular momentum ($\vec{J}$) as

$$E = -\gamma \vec{J} \cdot \overrightarrow{B}. \tag{1.2}$$

The gyromagnetic ratio, γ, is the resulting proportionality constant and is dependent on the charge and mass of the particle the interaction.

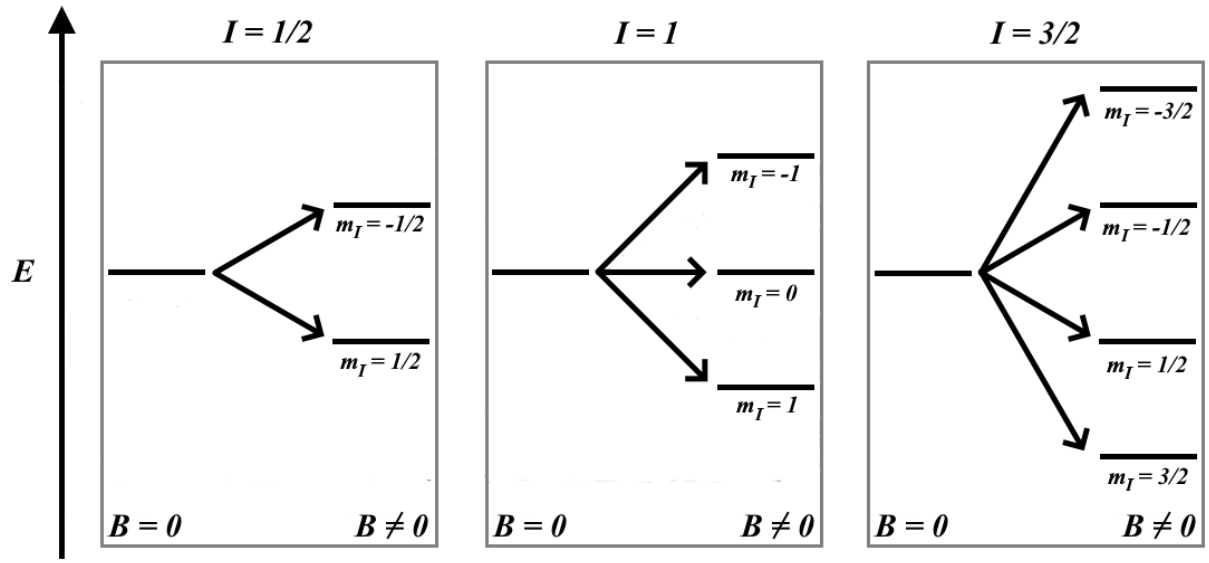

Figure 1.1. *Diagram of the energy levels for nuclear spins of 1/2, 1, and 3/2 before and after applying a magnetic field.*

The interaction of the magnetic dipole with a magnetic field lifts the degeneracies for a system with non-zero angular momentum in a symmetric manner as shown in Fig. 1.1 [13]. For the case of a particle with a nuclear spin of I = 1/2, two projections of the angular momentum exist on the z-axis as m_I = 1/2 and -1/2. These projections subject the particle to a decrease or increase in energy respectively due to the parallel and antiparallel interactions with the magnetic field. This pattern continues for all half-integer spins such as I = 3/2 with m_I = 3/2, 1/2, -1/2, and -3/2 with the extent of each energy shift governed by the projections.

Particles with integer spins undergo a similar splitting of degeneracies, but additionally possess a projection of $m_I = 0$ that is unaffected by the external magnetic field much like orbital angular momentum of the silver atom in the Stern-Gerlach experiment.

Consider the behavior of a common macroscopic object with a net magnetic moment in an external magnetic field, such as a compass needle in Earth's magnetic field. A torque is imposed on the magnetic moment forcing the object to rotate as governed by Eq. 1.3.

$$\vec{\tau} = \vec{\mu} \times \vec{B} \tag{1.3}$$

The minimum energy for the interaction is achieved when the needle reorients the magnetic moment to be aligned parallel to the Earth's field. Once the moment is polarized the needle ceases movement.

Table 1.1. *Gyromagnetic ratios (γ) of common NMR active nuclei.*

Nucleus	Nuclear Spin (*I*)	γ [MHz/T]
^{1}H	1/2	42.58
^{2}H	1	6.54
^{13}C	1/2	10.71
^{14}N	1	3.08
^{15}N	1/2	-4.32
^{19}F	1/2	40.08
^{31}P	1/2	17.24

The situation is similar for a spin in a magnetic field, but the motion is altered by the presence of a constant angular momentum. The magnetic moment will always maintain contributions in the x and y directions that is dependent on the initial orientation of the spin with respect to the direction of the magnetic field. The applied torque forces the spin to move about the principal axis of the magnetic field at a fixed angle, forming a cone. This is behavior that is easily modelled by the classical case of a spinning top under the tug of gravity and is referred to as precession. The rate of this precession, called the Larmor frequency, is proportional to the magnitude strength of the static magnetic field, B_0.

$$\omega_0 = -\gamma B_0 \tag{1.4}$$

γ determines both the direction of the motion and the extent of the magnetic field's influence on the particle. A majority of nuclear spins possess a positive gyromagnetic ratio which causes the magnetic moment to precess in a clockwise motion according to Eq. 1.4 and the right-hand rule.

1.2.3 Rabi's Contributions

The next crucial experiment in the development of magnetic resonance came from the mind of Isidor Rabi [14]. The Stern-Gerlach experimental setup was initially designed to isolate magnetic moments of different orientations as a sort of quantum state selector, but by placing a second apparatus in series it can be used to reconverge the separated beams for detection. Rabi took advantage of this fact in attempts to measure the nuclear magnetic moments of lithium compounds. An addition to the state selection and detection deflecting fields, a static electromagnet which generated homogeneous fields was placed in between with a solenoid coil situated in the electromagnet parallel to the molecular beam.

The coil introduces a radiofrequency (RF) oscillating magnetic field to the situation. By fixing the frequency of the oscillating field, ω_1, and varying the magnetic field strength of the electromagnet, B_0, Rabi saw a drastic decrease in beam intensity at a specific field strength similar to Fig. 1.2. This drop corresponds to a tuning of the Larmor frequency of the nuclear spins to the applied oscillating frequency, or magnetic resonance.

As is the case with the phenomenon of the Zeeman effect, the oscillating field applies a torque which effectively reorients the spin [12]. The RF field induces a transition between spin states which will change how the particle is deflected resulting in varying intensities at the detector. The resonance experiment demonstrates that the transition probability is at a maximum where the recorded beam intensity is at a minimum, but can still be non-zero when the oscillating field is near-resonance.

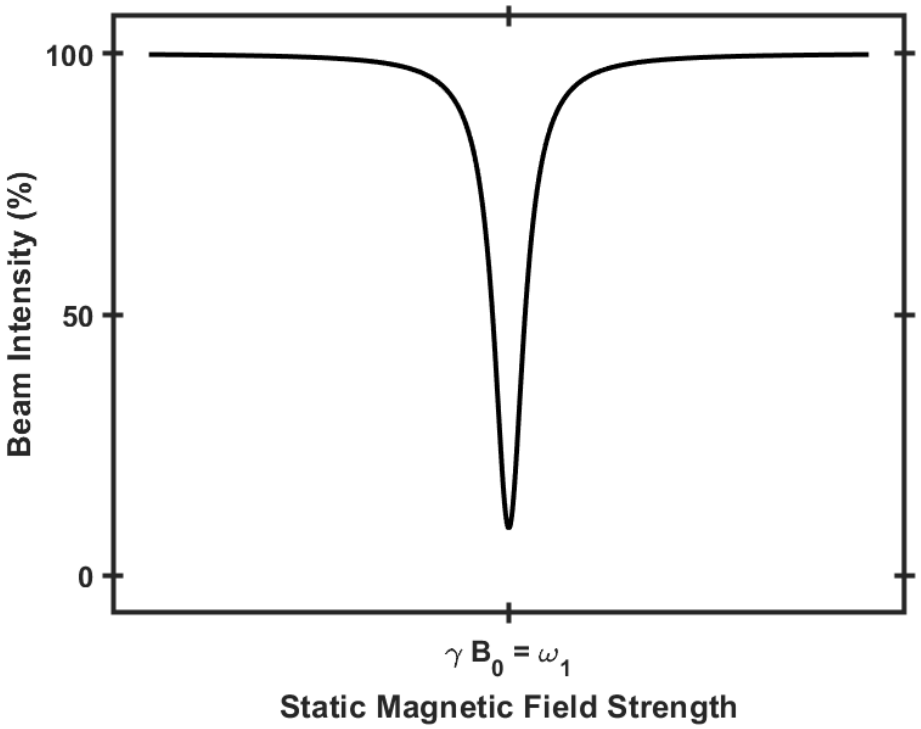

Figure 1.2. *Simplified reconstruction of Rabi's experimental results. Maximum transition probability is found at resonance where $\gamma B_0 = \omega_1$, shown here as a minimum in molecular beam intensity.*

Rabi's experiment serves as the blueprint for all magnetic resonance experiments today. Modern systems do not require specific spin state selection and thus, the Stern-Gerlach components are no longer used. Instead, most experiment use only the homogeneous magnetic field and the coil introduced by Rabi in which the coil acts as both the RF transmitter and the detector [15].

1.3 The Classical Equations of Motion for Magnetization

1.3.1 Net Magnetization and Free Precession

Up to the mid-1940's, all magnetic resonance experiments had been conducted on individual gas phase particles in a molecular beam [5,15]. In this context, the particles in question are not subjected to the macroscopic and bulk interactions that come from a more natural environment. The first successful experiments on condensed matter were performed by Edward Purcell and Felix Bloch [16,17]. When

discussing the behavior of an ensemble of spins undergoing a typical magnetic resonance experiment, Bloch proposed a classical approach.

It was suggested that the resultant magnetic moment of all spins in a set volume, dubbed the net magnetization, $\vec{M}$, undergoes a torque in a magnetic field much like individual spins do This is easily demonstrated by the substitution of $\vec{M}$ into Eq. 1.3.

$$\vec{\tau} = \vec{M} \times \vec{B} \tag{1.5}$$

The realization that torque in Eq. 1.5 is linearly proportional to the time variation of the net magnetization reveals the following differential equation:

$$\frac{d\vec{M}}{dt} = \gamma \vec{M} \times \vec{B} \tag{1.6}$$

The so-called Bloch equations provide a simple, yet effective model for the behavior of an ensemble of spins under several common scenarios [17].

The first case to be investigated is the net magnetization purely under the influence of the static magnetic field, B_0. The principal axis of the classical model, the z-axis, is defined by the direction of the B_0 field. At equilibrium, the solution to the Bloch equation is trivial as the net magnetization sits static on average in the z-direction. However, if $\vec{M}$ is forced into the x-y plane, a more interesting conclusion is drawn. Reorienting $\vec{M}$ to possess non-zero transverse components and solving the Bloch equations yields the following set of relationships:

$$\begin{aligned} M_x &= M_{xy} \sin(\omega_0 t) \\ M_y &= M_{xy} \cos(\omega_0 t) \\ M_z &= constant \end{aligned} \tag{1.7}$$

where M_{xy} represents the magnitude of the net magnetization in the x-y plane and ω_0 is the Larmor precession as defined in Eq. 1.4. These results shows that the magnetization precesses about z-axis at a fixed angle the in the absence of additional forces as seen in Fig. 1.3.

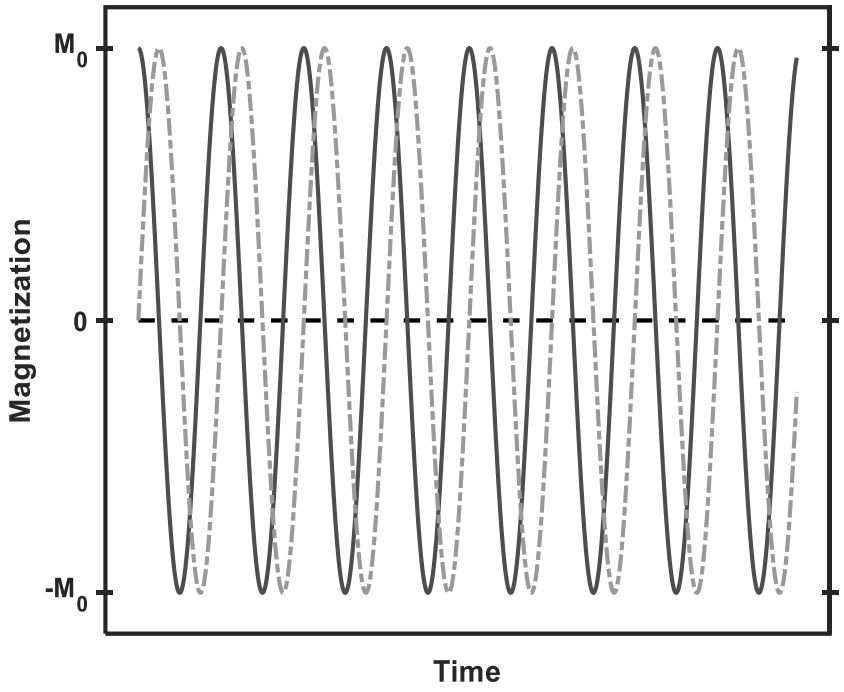

Figure 1.3. *The free precession solution to the Bloch equations in the laboratory frame for the x- (dark grey solid line), y- (light grey dash-dotted line), and z-components (black dashed line) of magnetization. M_0 is the magnitude of the net magnetization.*

1.3.2 Moving to the Rotating Frame of Reference

All discussions about motion up to this point have been viewed from the perspective of an outside observer, or the so called "laboratory frame." In a scenario consisting of only one source of motion, such as the pure Larmor precession case discussed in the previous section, the Bloch equations yield easily understood solutions. As additional perturbations are introduced, the effects of the individual influences become difficult to separate.

Consider the addition of an RF excitation source in a typical NMR experiment, depicted by

$$\frac{d\vec{M}}{dt} = \gamma\vec{M} \times \left(\overrightarrow{B_0} + 2\overrightarrow{B_1}\cos(\omega_c t)\right). \tag{1.8}$$

With the application of two magnetic fields, the static B_0 and the linearly polarized, oscillating B_1 with a carrier frequency of ω_c, it is reasonable to expect that the magnetization will precess about both fields simultaneously. However, comprehending these results from the Bloch equations becomes increasingly difficult with each perturbation that is added. For the purposes of this thesis, the phase term of the oscillating field is neglected as the relevant pulses that will be discussed will be aligned along axes.

To simplify the picture that is drawn it is common practice to switch to another frame of reference. Rotating the x and y components of the coordinate system in the complementary direction to the Larmor precession near the resonant frequency essentially inhibits the impact of the B_0 field. From the perspective of this new coordinate system, the static field appears to reduce in strength in accordance with

$$B_{eff} = B_0 - \frac{\omega_{rot}}{\gamma} \tag{1.9}$$

where ω_{rot} represents the frequency at which the x- and y- axes rotate. This is referred to as the "rotating frame" of reference.

A secondary assumption is made to further simplify calculations. Radiofrequency pulses are typically applied in the xy-plane and oscillates parallel to the plane. The radiation could be mathematically decomposed into two circularly polarized sources rotating in opposing directions within the xy-plane given by Eq. 1.10 and 1.11.

$$\overrightarrow{B_{1A}} = \overrightarrow{B_1}[\cos(\omega_c t)\,\hat{x} + \sin(\omega_c t)\,\hat{y}] \tag{1.10}$$

$$\overrightarrow{B_{1B}} = \overrightarrow{B_1}[\cos(\omega_c t)\,\hat{x} - \sin(\omega_c t)\,\hat{y}] \tag{1.11}$$

Given that B_{1A} *and* B_{1B} in the same plane as the rotating coordinates, moving to the rotating frame also changes how these fields appear.

Like Larmor precession, the B_{1A} component rotates counterclockwise, and thus the apparent frequency in the rotating frame is reduced. The opposite is true for the clockwise B_{1B} which appears to move faster. When the carrier frequency is close to the transition frequency, B_{1A} becomes nearly static while B_{1B} moves with almost double the initial frequency. The latter field oscillates too quickly to have any appreciable effect on the magnetization and thus can be neglected leaving only the reduced B_{1A}. By keeping

only one rotating field the effective B_1 magnitude in the rotating frame is halved. This is the rotating wave approximation.

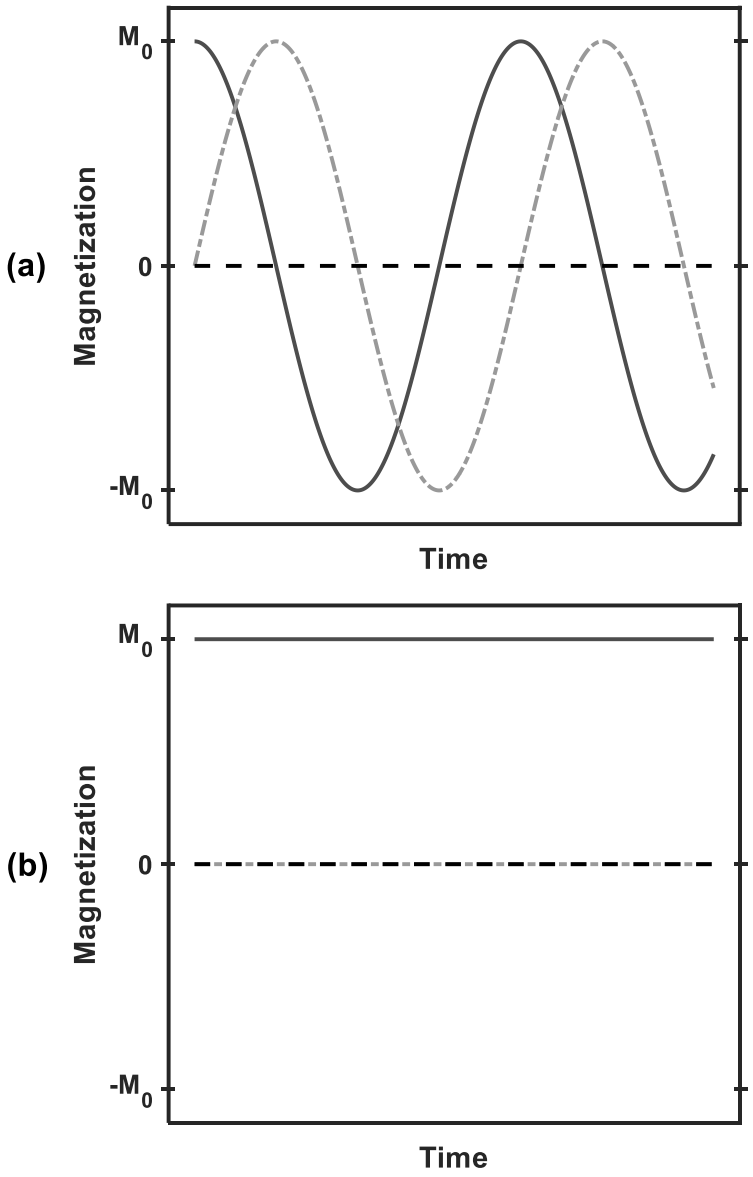

Figure 1.4. *The off-resonance (a) and on-resonance (b) free precession solutions to the Bloch equations in the rotating frame for the x- (dark grey solid line), y- (light grey dash-dotted line), and z-components (black dashed line) of magnetization. M_0 is the magnitude of the net magnetization.*

Combining the rotating frame transformation and rotating wave approximation, the Bloch equations expressed in Eq. 1.8 modifies to the form

$$\frac{d\overrightarrow{M'}}{dt} = \gamma\overrightarrow{M'} \times \left(\overrightarrow{B'_{eff}} + \overrightarrow{B'_1}\cos((\omega_0 - \omega_c)t)\right). \tag{1.12}$$

Through the remainder of this chapter, the tick mark will be used to represent the Bloch equations in the rotating frame [12]. In the condition where ω_{rot} and ω_c are in resonance with the Larmor frequency, Eq. 1.10 reduces to the form

$$\frac{d\overrightarrow{M'}}{dt} = \gamma\overrightarrow{M'} \times \overrightarrow{B'_1}, \tag{1.13}$$

where the Bloch equation for the effects of an RF pulse is similar to the free precession scenario in the laboratory frame. That is, the net magnetization rotates about the axis of the perturbation at a frequency of ω_1 as the Larmor precession piece becomes constant as seen in Fig. 1.4(b). For simple two-level systems, such as ^{1}H NMR, the frequency of this nutation, ω_1, is equivalent to the Rabi frequency, or the rate of population cycling between the spin up and spin down states.

1.3.3 Applying a sequence of RF pulses

Modern NMR spectroscopy utilizes various sequences of RF pulses to coax out the physical properties of an analyte. Armed with a clear image of the effect of RF on the net magnetization, keeping track of the current position of $\vec{M}$ when applying multiple pulses can be further simplified. Consider the matrices for the elemental rotations of vectors in linear algebra:

$$\boldsymbol{R_x}(\alpha) = \begin{bmatrix} 1 & 0 & 0 \\ 0 & \cos(\alpha) & -\sin(\alpha) \\ 0 & \sin(\alpha) & \cos(\alpha) \end{bmatrix}$$

$$\boldsymbol{R_y}(\alpha) = \begin{bmatrix} \cos(\alpha) & 0 & \sin(\alpha) \\ 0 & 1 & 0 \\ -\sin(\alpha) & 0 & \cos(\alpha) \end{bmatrix} \tag{1.14}$$

$$\boldsymbol{R_z}(\alpha) = \begin{bmatrix} \cos(\alpha) & -\sin(\alpha) & 0 \\ \sin(\alpha) & \cos(\alpha) & 0 \\ 0 & 0 & 1 \end{bmatrix}$$

where α is the angle of rotation to be referred to as the flip angle from here on. In the rotating frame, these matrices provide a general solution to any RF pulse along the Cartesian axes [13].

The flip angle of the magnetization is dependent on the duration of the applied pulse, τ_p, as determined by

$$\alpha = \omega_1 \tau_p \tag{1.15}$$

In most routine experiments, including those to be discussed in this chapter, pulses are referred to by their direction and the flip angle. The most prevalent perturbations are due to π/2 and π pulses, corresponding to 90° and 180°, respectively.

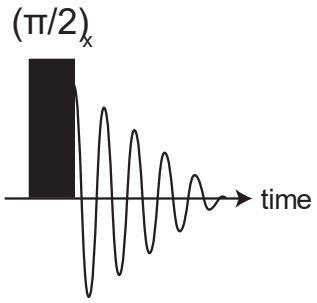

Figure 1.5. *The Free Induction Decay Pulse Sequence. The black rectangle represents a π/2 RF pulse in the x-direction. The damped oscillating function represents the time window for acquisition of the signal.*

Fig. 1.5 depicts the simplest pulse sequence in NMR, the Free Induction Decay (FID) experiment [15]. This experiment consists of a single π/2 pulse applied in the x-direction which according to Eq. 1.14 rotates the magnetization vector to align in the -y-direction. The receiver is then opened to acquire signal over some period of time. This signal is the basis for structure elucidation by one-dimensional NMR and will be explored briefly in a future section.

1.4 Relaxation: Returning to Equilibrium

The final piece of the Bloch model required to describe routine NMR experiments is a mechanism for energy loss. As with any form of spectroscopy, the energy absorbed from a photon is eventually dispersed to return the system back to its equilibrium state. For example, in electronic spectroscopy, an

electron may shed excess energy via radiation-based methods like fluorescence and phosphorescence, or even radiationless processes such as intersystem crossings. Bloch suggested two parameters for the relaxation of the magnetization along the z-axis and in the xy-plane.

1.4.1 Spin-Lattice Relaxation

The first type of relaxation mentioned by Bloch is the return of the z-component of the magnetization to equilibrium, M_0 [17]. The spin-lattice, or longitudinal, relaxation characteristic time constant, is denoted as T_1 and only contributes to the recovery of M_z. To account for this in the Bloch equations, Eq. 1.12 is added to the overall time evolution of M_z.

$$\frac{dM_z}{dt} = \frac{(M_0 - M_z)}{T_1} \tag{1.15}$$

Solving the spin-lattice term independently yields a result akin to first-order chemical kinetics – the system approaches the equilibrium state exponentially as

$$M_z = M_0\left(1 - e^{-\frac{t}{T_1}}\right) \tag{1.16}$$

Most standard NMR instruments possess a single detection channel perpendicular to the B_0 field, thus direct detection of magnetization parallel to the static field is not possible [15]. In order to measure T_1, alternative methods are required. One such experiment is the technique of Inversion Recovery as shown in Fig. 1.6.

The concept of the Inversion Recovery pulse sequence is simple: a π-pulse rotates $\vec{M}$ to be anti-parallel to the direction of the static field and the z-component is monitored over several time increments t_1 as it relaxes through zero and eventually returns to M_0 [19]. To measure the current value of M_z, a π/2-pulse is necessary prior to acquisition to rotate this component into the plane of detection. The signal reflects the exponential behavior of the Bloch solution, albeit with a slight amplitude modification as the signal begins at $-M_0$ rather than zero.

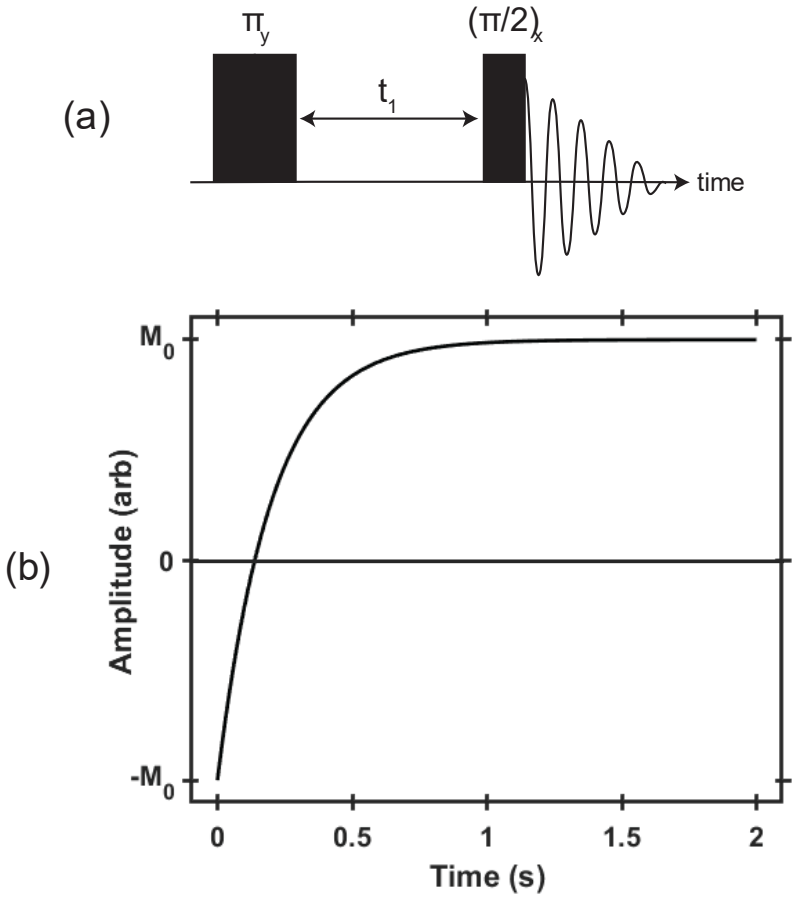

Figure 1.6. *The Inversion Recovery pulse sequence (a) and the corresponding transient (b) for a spin-lattice relaxation time of 0.2 s.*

$$M_z = M_0\left(1 - 2e^{-\frac{t}{T_1}}\right) \tag{1.17}$$

Another technique for measuring T_1 is the Saturation Recovery pulse sequence [20]. By applying a train of rapid π/2-pulses, the magnetization in the sample can effectively be destroyed allowing for an experiment that begins at $M_z = 0$. Similar to the Inversion Recovery method, M_z is allowed to relax over some time increment before a π/2-pulse allows for detection. The signal produced from the Saturation Recovery technique more closely matches Eq. 1.13.

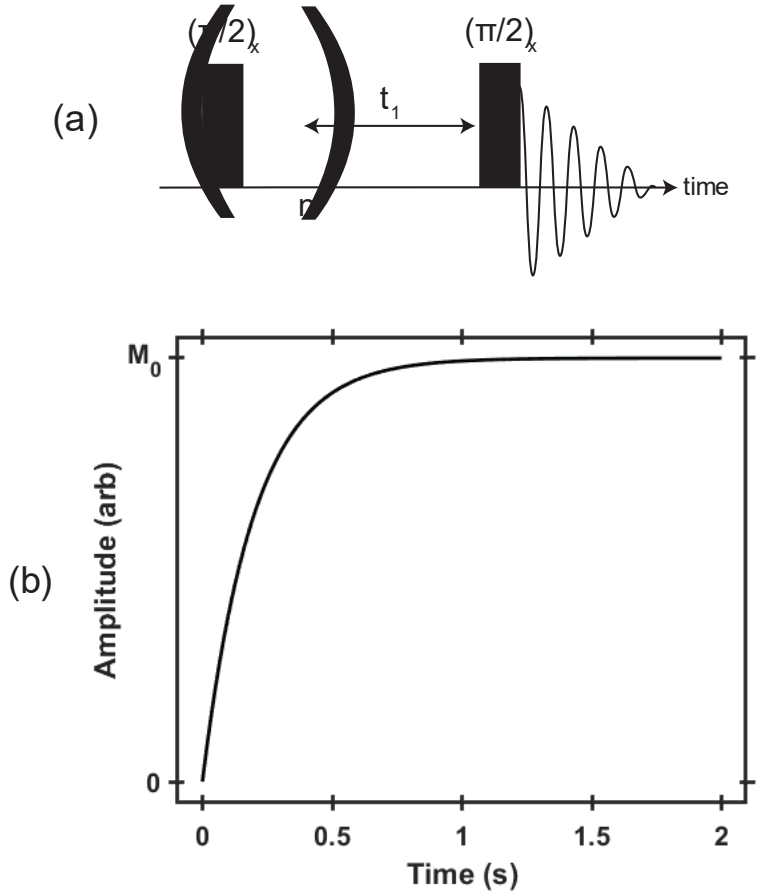

Figure 1.7. *The Saturation Recovery pulse sequence (a) and the corresponding transient (b) for a spin-lattice relaxation time of 0.2 s.*

1.4.2 Spin-Spin Relaxation

The second type of relaxation is spin-spin, or transverse, relaxation which is characterized by the time constant T_2. In contrast to spin-lattice relaxation, spin-spin relaxation is concerned with depletion of the x- and y-components of the magnetization. The rate of decay in both directions is equivalent resulting in similar terms for the respective Bloch equations.

$$\frac{dM_x}{dt} = \frac{-M_x}{T_2} \tag{1.18}$$

$$\frac{dM_y}{dt} = \frac{-M_y}{T_2} \tag{1.19}$$

Like the spin-lattice solution, solving these differential equations provide simple exponential solutions.

$$M_x = M_0 e^{-\frac{t}{T_2}} \tag{1.20}$$

$$M_y = M_0 e^{-\frac{t}{T_2}} \tag{1.21}$$

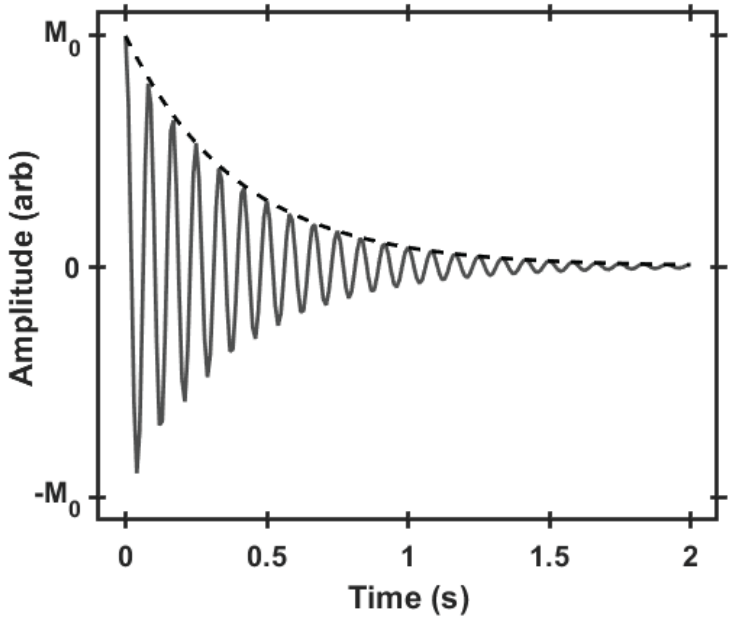

Figure 1.8. *The FID signal in the laboratory (solid) and rotating (dashed) frames. All oscillations are removed in the rotating frame leaving only the exponential which decays with a spin-spin relaxation time of 0.4 s.*

M_x and M_y are directly detectable in most instruments unlike M_z [15]. The most obvious visual for the effect of spin-spin relaxation is the FID signal mentioned in section 1.3.3. By applying a π/2 pulse along the x-axis, the entirety of $\vec{M}$ is flipped to the -y-direction. When monitoring M_y from the laboratory frame, the signal is the product of two functions, the oscillation of free precession and the decay of the transverse relaxation solution. This signal simplifies to the pure exponential piece in the rotating frame as demonstrated by Fig. 1.8.

According to the Bloch equations, one should be easily able to determine T_2 by investigating the envelope of the FID signal. Two potential methods for recovering this parameter are by fitting or by Fourier

transforming to the frequency domain. In the latter case, T_2 is inversely proportional to the full width at half height of the frequency spectrum. These methods are generally not preferred as any inhomogeneity in the magnetic field causes deviations from the true value of T_2:

$$\frac{1}{T_2^*} = \frac{1}{T_2} + \frac{1}{T_{inhom}}. \tag{1.22}$$

T_2^* is the effective transverse relaxation time constant which is always shorter than the true T_2 [15]. Without a method to disentangle T_2 from the effects of field inhomogeneity, T_{inhom}, this apparent time constant yields no significant information about the dynamics of the sample. As a consequence, using an FID to determine T_2 risks the introduction of error and faulty characterization of an analyte.

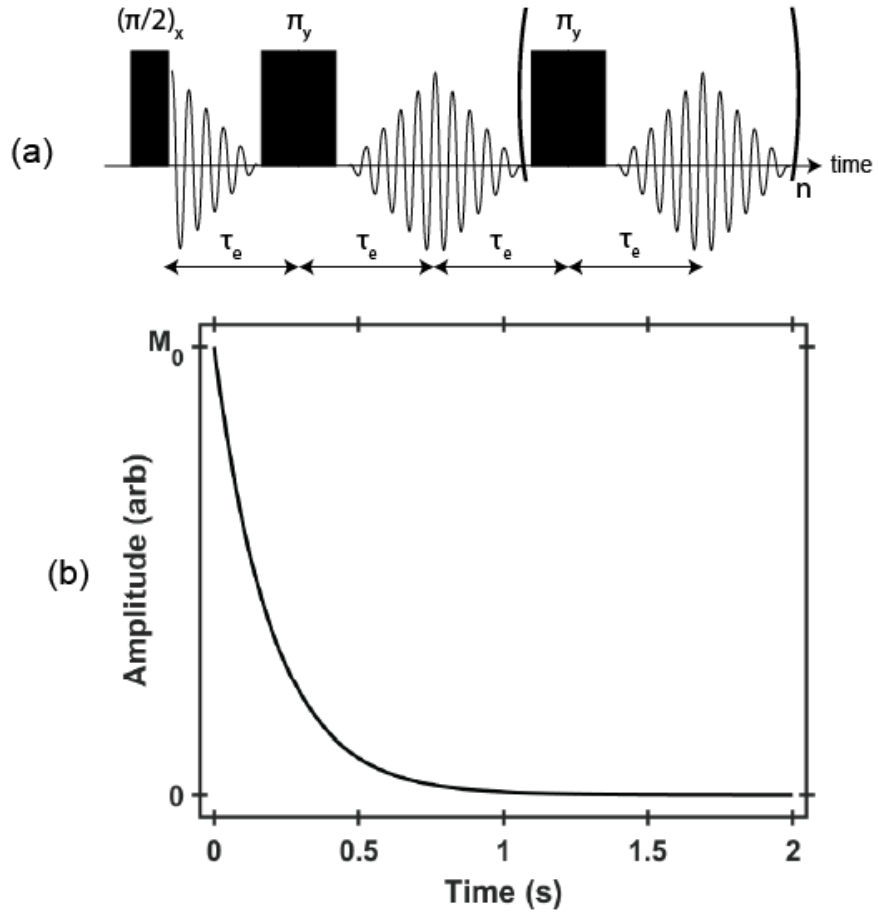

Figure 1.9. *The Carr-Purcell-Meiboom-Gill pulse sequence (a) and the corresponding transient (b) for a spin-spin relaxation time of 0.4 s.*

To ensure the proper measurement of T_2, another pulse sequence dominates the relaxation market. The Carr-Purcell-Meiboom-Gill (CPMG) sequence, shown in fig. 1.9, is applied to cancel out the effects of dephasing [21,22]. To understand the CPMG pulse sequence, a brief discussion about spin echoes is necessary[23].

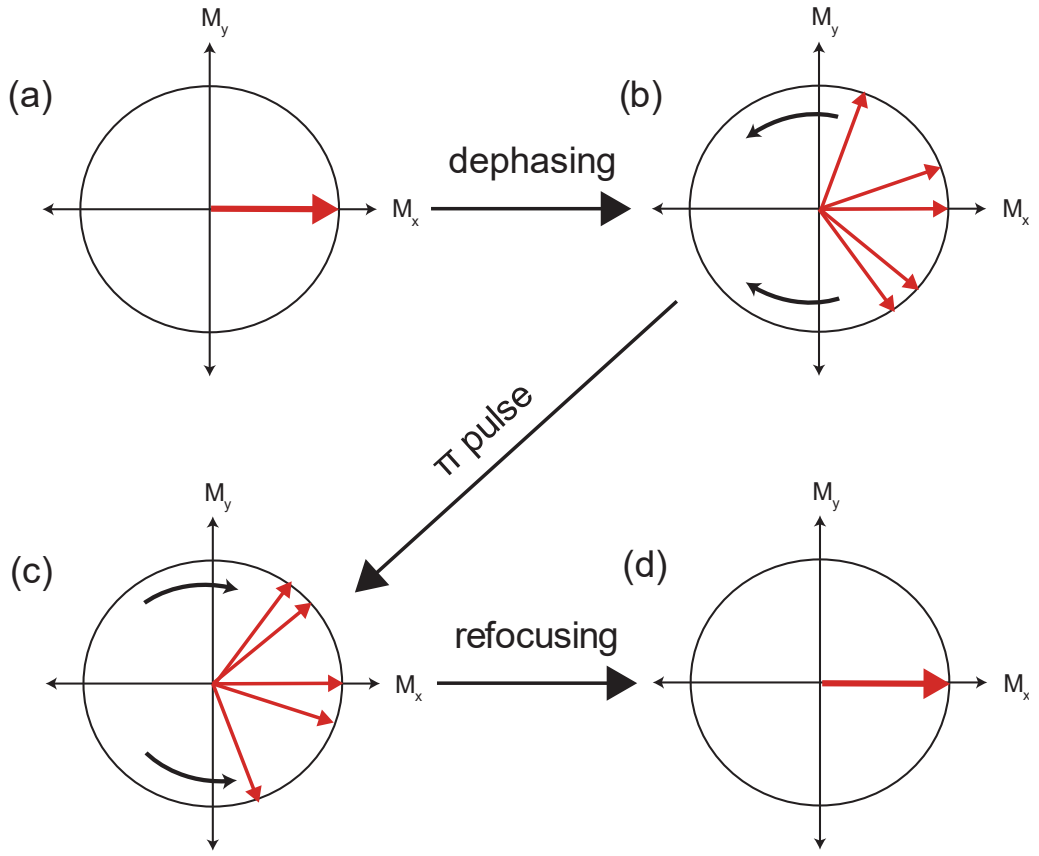

Figure 1.10. *The behavior of spins in the xy-plane during a spin echo. (a) is the moment immediately after the π/2 pulse. (b) shows the effect of inhomogeneity as the spins dephase from each other. (c) depicts the reflection due to the pi pulse which maintains the frequency of each spin. (d) is the point at which the spins are refocused.*

In the instant immediately after applying a π/2 pulse, all spins are roughly parallel in the transverse plane. If these spins are allowed to evolve in time, one would expect that all spins precess with the same frequency and direction in the plane. However, the spins all experience a slightly different field strength depending on their position with respect to the magnetic field, and therefore each spin rotates with not only

different frequencies, but potentially different directions. While this may seem difficult to correct, it is as simple as the application of a π-pulse.

By applying a π pulse along the complimentary transverse axis to the initial π/2 pulse, the magnetic moments reflect across the axis. Assuming this process happens faster than the translation of the molecules, each spin will maintain its frequency and direction of precession. This means that the magnetic moments that were departing from each other will now be moving towards each other, almost as if time was reversed. These spins will come back in phase for one moment before spreading out once again. The refocusing of these spins is the spin echo.

The CPMG sequence utilizes this concept to cancel out the inhomogeneity effects, yielding a transient akin to an FID in the rotating frame with an appropriate decay rate. As depicted in fig. 1.10(a), the first two pulses are a spin echo sequence with a π/2 x-pulse, followed by an evolution time, τ_e, then a π y-pulse. An acquisition window is opened to detect the maximum of the echo at twice the evolution time as the time to refocus is equivalent to the amount of time the spins had to dephase. The key to the CPMG sequence looking at a train of echoes to monitor the maximum magnitude of the transverse magnetization at several points in time as it decreases to 0. This is achieved by looping through the steps after the π/2 pulse. Following the spin echo, the spins are allowed to dephase over τ_e again, another π y-pulse is applied, and the next echo is detected before repeating until the signal is near 0.

1.4.3 Autocorrelation and Spectral Density

The Bloch equations provide a sufficient model to describe the effect of relaxation on the net magnetization of the sample. However, the relaxation term of these equations of motion is a phenomenological approximation and does not give any physical intuition about the mechanisms of relaxation. It is beneficial to take a more stochastic approach to understanding the processes that drive relaxation [13,2].

Neglected up to this point are the small local magnetic fields experienced by each spin at any given moment. It is these local interactions that provide opportunities for returning to the equilibrium state. Due

to the constant motions and tumbling of molecules, these fields fluctuate rapidly and randomly and thus the average local field felt by the spins over a long period of time approaches zero [25]. However, by looking at these fluctuations from moment to moment, it is possible to develop a model that gives more insight to the significance of measuring time constants.

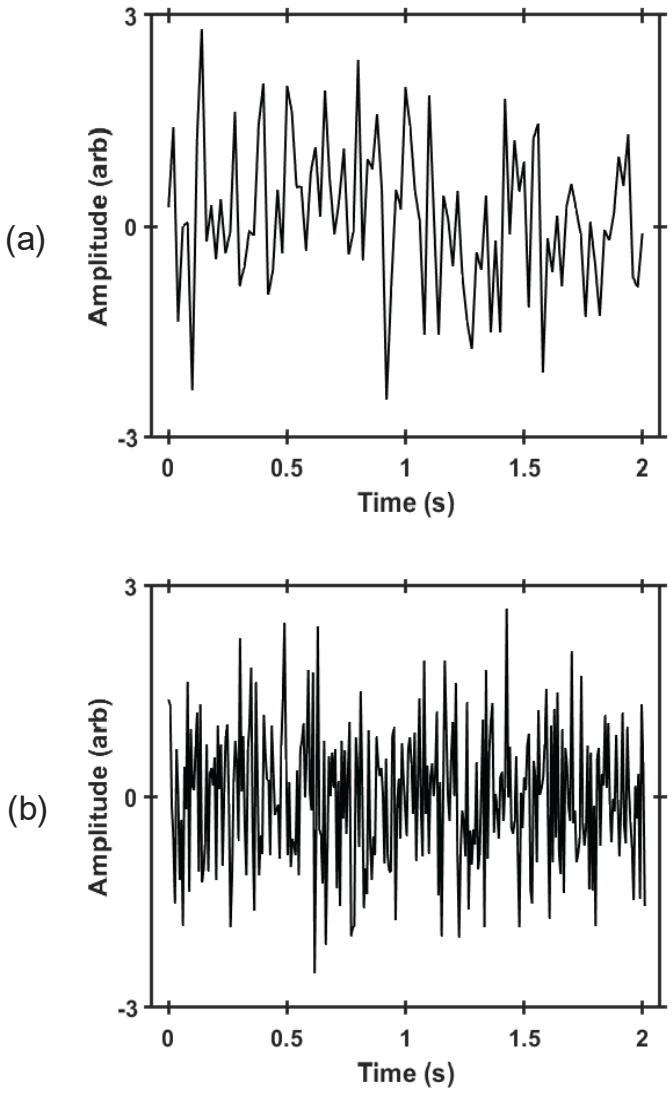

Figure 1.11. *Two random functions describing the behavior of locally fluctuating fields along the x-axis. Function (a) fluctuates less rapidly than function (b) which leads to different correlation times.*

Consider two functions which behave randomly over time, one of which appears to fluctuate more rapidly than the other as shown in fig. 1.11. If two points are taken from the function with slower fluctuations, one would expect no relationship between the two points as it is random. However, it may be noted that with sufficiently short times intervals, the strength of the fields at random pairs of time points often possess the same sign and close magnitudes. As the time interval, τ, is increased, this trend becomes less prevalent. The faster fluctuating function experiences similar behavior, but it is clear that the seemingly correlated behavior of the local fields falls off faster.

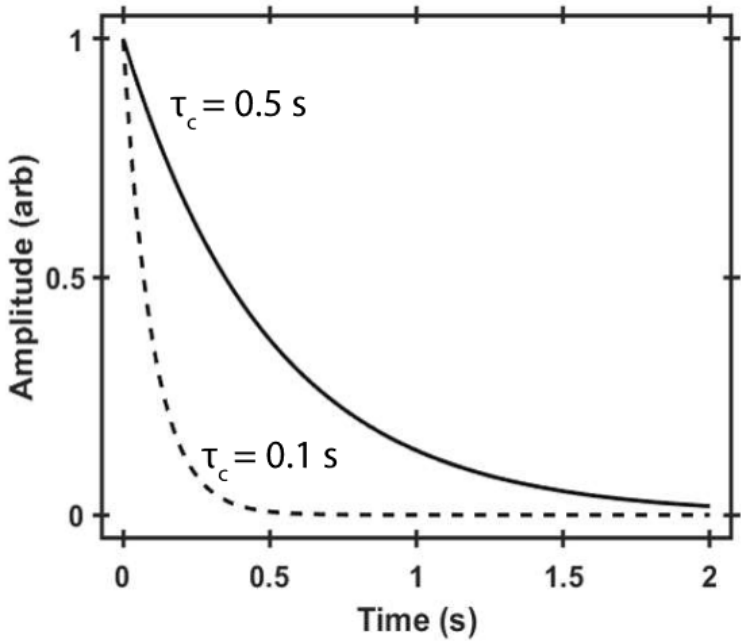

Figure 1.12. *The corresponding autocorrelation functions for a fast fluctuating function (solid) and a slow fluctuating function (dashed) with respective correlation times of 0.1 s and 0.5 s.* $\langle B^2 \rangle$ *is set to 1 for this simulation.*

To better explain this concept, it is useful to look at all pairs of points with the same interval. This is achieved by the autocorrelation function:

$$G(\tau) = \langle B(t)B(t+\tau) \rangle = \langle B^2 \rangle e^{-\frac{|\tau|}{\tau_c}}. \tag{1.23}$$

When the products of the fields at a given interval are averaged, a clearer time-dependent correlation appears. This function decays exponentially at a rate of $1/\tau_c$, where τ_c is the correlation time, as shown in Fig. 1.11. The rate of decay is strongly influenced by the rate of fluctuations in the random function.

Recall that how fast the local fields fluctuate is tied to the tumbling of molecules. It should be no surprise that faster tumbling equals faster fluctuations as the orientations of the molecules with respect to each other rapidly vary. In other words, faster motions yield shorter correlation times. This is captured by an alternative definition of τ_c – the time it takes for the molecule to tumble one radian. The measurement of correlation times reveals information about the dynamics of a sample. For liquids, which are the focus of the research conducted in this thesis, the Stokes-Einstein-Debye equation

$$\tau_c = \frac{\eta V}{k_B T} \tag{1.24}$$

relates τ_c to the viscosity (η), volume (V), and temperature (T) of the sample where k_B is the Boltzmann constant [26].

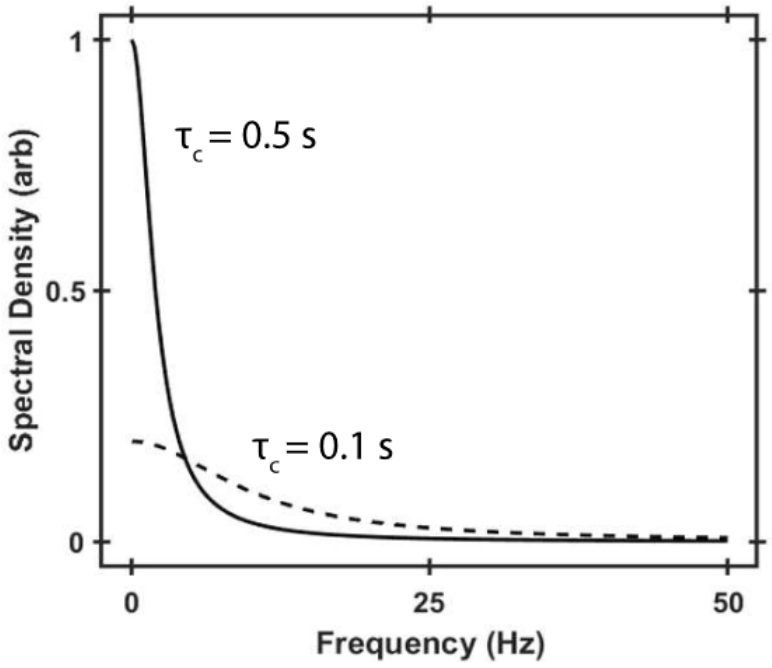

Figure 1.13. *The corresponding spectral density functions for the slow fluctuating function (solid) and fast fluctuating function (dashed) with respective correlation times of 0.1 s and 0.5 s.* $\langle B^2 \rangle$ *is set to 1 for this simulation.*

It is also useful to look at the frequency counterpart to the autocorrelation function. The Fourier transform of the autocorrelation function yields the spectral density function.

$$J(\omega) = 2\int_0^\infty \langle B^2\rangle e^{-\frac{|\tau|}{\tau_c}} e^{i\omega t} dt = 2\langle B^2\rangle \frac{\tau_c}{1+\omega^2\tau_c^2} \tag{1.25}$$

This function yields the probability of finding a spin tumbling with a specific frequency given the amount of motion as defined by τ_c. The spectral density function holds the key to predicting the relaxation time constants for a given sample.

Armed with spectral density functions and the Stokes-Einstein-Debye relation, a simple model is available to predict relaxation time constants based on the nature of a sample. The first step to applying this model is the realization that the relaxation process for a spin is just a transition between states. Just as a spin must be excited at the Larmor frequency, emission requires the spin to feel the local fluctuating fields at the Larmor frequency, or at $J(\omega_0)$ [13].

In theme with the excitation of a spin, spin-lattice relaxation requires the precession of the components of $\vec{M}$ to induce a transition between states. Thus, only local fields perpendicular to the spin contribute to the process. For the case of spin-lattice relaxation, T_1 is dependent on the transverse components of the fluctuating fields giving rise to the following relationship:

$$\frac{1}{T_1} = 2\gamma^2\langle B_x^2 + B_y^2\rangle \frac{\tau_c}{1+\omega^2\tau_c^2} \tag{1.26}$$

In contrast, spin-spin relaxation is accomplished by demolishing the coherence of spins, adding some slight complexity. The annihilation of coherence can be accomplished in two ways, taking the spin out of the transverse plane and dephasing. The first is achieved in the same way as the spin-lattice case, the transverse elements of the local fields cause spin flips which provides the non-secular piece of T_2. The latter contribution was mentioned in the previous section, field inhomogeneity. Dephasing does not require a direct transition between states, and thus is not dependent on the Larmor frequency. Rather the maximum

of the spectral density, $J(0)$, is used to determine the secular piece of the relationship. The total equation for predicting T_2 is

$$\frac{1}{T_2} = \gamma^2\langle B_z^2\rangle\tau_c + \gamma^2\langle B_x^2 + B_y^2\rangle\frac{\tau_c}{1+\omega^2\tau_c^2} \tag{1.27}$$

Note that T_2 is always related to T_1 by

$$\frac{1}{T_2} = \gamma^2\langle B_z^2\rangle\tau_c + \frac{1}{2T_1}, \tag{1.28}$$

where the factor of 1/2 in the T_1 term arises from the consideration that the x- and y- magnetization is only influenced by fields of the opposite transverse component.

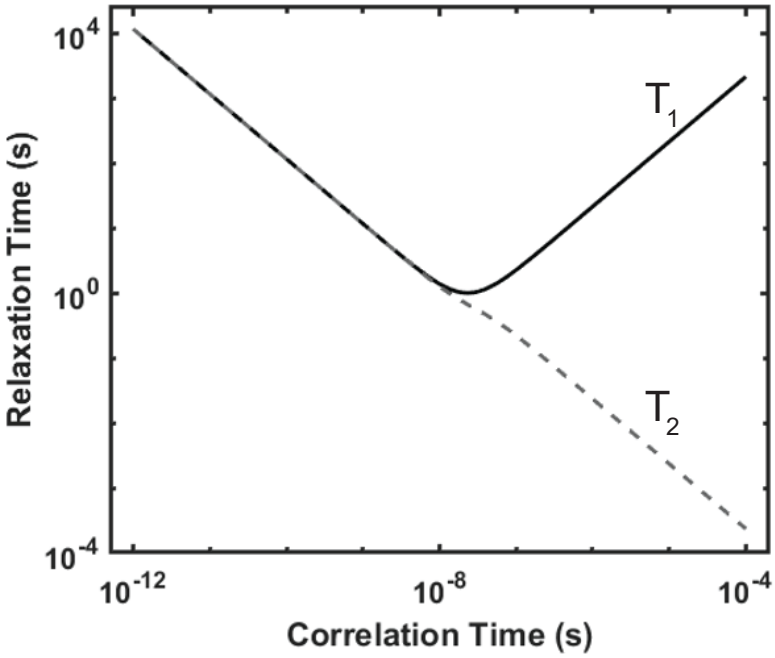

Figure 1.14. *A comparison of the spin-lattice (solid) and spin-spin (dashed) relaxation rates as a function of correlation time. Note that the spin-spin rate continues decreasing due to the effects of the field fluctuations in the z-direction.*

Fig. 1.14 shows the dependence of T_1 and T_2 on the correlation time which is a useful comparison for the prediction of relaxation rates for a given set of conditions. When motions are slow, or τ_c is long,

there is a large deviation in the relaxation time constants that is caused by the linear secular term of Eq. 1.26. This is typically the regime of solid-state NMR and low temperature experiments. On the opposite extreme is the fast motion regime that is characteristic of liquids and high temperature experiments. The region in which T_1 and T_2 are approximately equivalent is known as "the extreme narrowing limit." This is the limit where the conditions of the experiments conducted in this thesis lie [13].

1.5 Relaxation Mechanisms

With some background to the factors that affect relaxation rates, this chapter concludes with a brief overview of some of the most important mechanisms involved in the relaxation of spin-1/2 nuclei [27]. Generally, relaxation is driven by a single prevailing force which can be dependent on things such as the state of matter, spin, and impurities.

1.5.1 Dipolar Coupling

The most obvious fluctuating fields come from the dipole-dipole coupling of magnetic dipoles between nuclear spins [28]. The strength of the dipolar coupling is dependent on both the distance between spins, r_{IS}, and the orientation of a vector passing through both spins with respect to the static field, Θ_{IS}.

$$d_{IS} = -\frac{\mu_0 \gamma_I \gamma_S \hbar}{4\pi r_{IS}^3}(3\cos^2(\Theta_{IS}) - 1) \tag{1.29}$$

The radial piece of this secular dipolar coupling constant falls off quickly as $1/r_{IS}^3$ requiring spins to be within close range to each other.

In solid-state NMR, the angular component of dipolar coupling gives rise to interesting line shapes. As molecular tumbling is slow in solids, orientation-dependent interactions are prevalent appearing in the form of broad doublet known as the Pake pattern [29]. It is a common practice to narrow these spectral peaks by canceling out dipolar couplings. This is accomplished by rapidly spinning the solid at 54.74°, the so-called "magic angle," with respect to the static field [30]. When the frequency of spinning is sufficiently high, this angle sends the angular piece of the dipolar coupling constant to zero as all anisotropic interactions

average out. In contrast, liquids tumble fast enough to average out dipolar effects on their own, thus no broadening appears. In both solids undergoing magic angle spinning and liquids, despite the cancellation of effects on average, the radial piece of the dipolar coupling still plays an important role in relaxation. These *through-space* interactions are typically the dominant relaxation mechanism in the majority spin-1/2 systems.

1.5.2 Paramagnetism

One of the few interactions which can trump the strength of nuclear dipolar coupling is the dipolar coupling between a nuclear spin and the spin of an unpaired electron [30]. Consider the gyromagnetic ratios of nuclei and an electron to be used in the calculation of Eq. 1.29. Whereas γ for nuclei are usually in the range of 1-100 MHz/T, electron spins precess much faster in a static field with a γ of about 28 GHz/T. As a result, the dipolar coupling constant for the interaction of a nuclear spin with an electron spin is anywhere from 100 to 10,000 times greater than that of the coupling between two nuclei. The relaxation time constants shorten drastically with the introduction of ions to a solution where more unpaired electrons in an electron induce a stronger effect. Often this is used experimentally to control the relaxation rate of a substance by the dissolution of a salt. The relaxation of the samples in the experiments described in chapters 3 and 4 of this thesis are primarily driven by these paramagnetic interactions.

1.5.3 J-coupling and Scalar Relaxation

NMR is most widely used for the structure elucidation of complex molecules. In strong static fields, the spectra produced by a simple FID experiment are high resolution. Depending on the neighboring nuclear environment, the spectral peaks split into several hyperfine peaks [32]. This is the result of *J*-coupling, an indirect, *through-bond* interaction. In liquids, the *J*-coupling constant is isotropic and therefore scalar leading to the alternative term of scalar coupling.

The basic mechanism of scalar coupling is the polarization of electrons due to interactions with nuclear magnetic dipoles [33]. The resonant frequency of a nuclear spin is slightly shifted when the magnetic moment of a nearby electron is changed. An example of this process is nucleus *A* polarizes an associated electron *A* forcing electron *B* to flip its spin according to the Pauli exclusion principle. Because there are two equally probable spin flips, two hyperfine transition lines appear for each nucleus in the spectrum.

In the context of relaxation, there are two ways in which scalar couplings can contribute to the relaxation process [34]. First, if spins are exchanging at a rate faster than the *J*-coupling constant, scalar couplings may fluctuate allowing for relaxation to occur. This is referred to as "scalar relaxation of the first kind." The second case occurs when one nucleus is coupled to another nucleus with a faster relaxation rate. The changes of the second nucleus induces a modulation which can drive faster relaxation for the first nucleus. This is referred to as "scalar relaxation of the second kind." These scalar relaxation processes seldom overpower dipolar mechanisms for relaxation.

References

[1] B. I. Ionin, B. A. Ershov, *NMR Spectroscopy in Organic Chemistry* (Plenum Press, New York, USA, 1970)

[2] F. Chao, R. A. Byrd, Protein dynamics revealed by NMR relaxation methods. Emerg. Top Life Sci. **2**, 93-105 (2020)

[3] K. J. Packer, C. Rees, Pulsed NMR studies of restricted diffusion: I. Droplet size distributions in emulsions. J. Colloid Interface Sci. **40**, 206-218 (1971)

[4] M. Baias, Mobile NMR: An essential tool for protecting our cultural heritage. Magn. Reson. Chem. **55**, 33-37 (2017)

[5] E. D. Becker, A brief history of nuclear magnetic resonance. Anal. Chem. **65**, 295A-302A (1993)

[6] A. Sommerfeld, Zur Quantentheorie der Spektrallinien. Ann. Phys, **51**, 1-94 (1916)

[7] W. Gerlach, O. Stern, Der experimentelle Nachwies des magnetischen moments des silberatoms. Z. Phys. **8**, 110-111 (1922)

[8] W. Gerlach, O. Stern, Der experimentelle Nachwies der Richtungsquentelung im magnetfeld. Z. Phys. **8**, 349-352 (1922)

[9] W. Gerlach, O. Stern, Das magnetischen moments des silberatoms. Z. Phys. **9**, 353-355 (1922)

[10] G. E. Uhlenbeck, S. Goudsmit, Ersetzung der hypothese vom unmechanischen zwang durch eine Forderung bezüglich des inneren verhaltens jedes einzelnen elektrons. Sci. Nat. **13**, 953-954 (1925)

[11] E. D. Commins, Electron spin and its history. Annu. Rev. Nucl. Part. Sci. **62**, 133-157 (2012)

[12] R. Schumacher, *Magnetic Resonance* (W. A. Benjamin, New York, USA, 1970)

[13] M. H. Levitt, *Spin Dynamics: Basics of Nuclear Magnetic Resonance* (John Wiley and Sons, West Sussex, UK, 2008)

[14] I. I. Rabi, J. R. Zacharias, S. Millman, P. Kusch. A new method of measuring nuclear magnetic moment. Phys. Rev. **53**, 318-319 (1938)

[15] E. Fukushima, S. B. W. Roeder, *Experimental Pulse NMR: A Nuts and Bolts Approach* (Addison-Wesley, Massachusetts, USA, 1981)

[16] E. M. Purcell, H. C. Torrey, R. V. Pound, Resonance absorption by nuclear magnetic moments in a solid. Phys. Rev. 69, 37-38 (1946)

[17] F. Bloch, Nuclear induction, Phys. Rev. **70**, 460-474 (1946)

[18] A. Ellis, M. Feher, T. Wright, *Electronic and Photoelectron Spectroscopy* (University Press, Cambridge, UK, 2005)

[19] E. L. Hahn, An accurate nuclear magnetic resonance method for measuring spin-lattice relaxation times. **76**, 145-146 (1949)

[20] J. E. Anderson, R. Ullman, Saturation-recovery method for determining nuclear spin-lattice relaxation times. J. Phys. Chem. **71**, 4133-4134 (1967)

[21] H. Y. Carr, E. M. Purcell, Effects of diffusion on free precession in nuclear magnetic resonance experiments. Phys. Rev. **94**, 630-638 (1954)

[22] S. Meiboom, D. Gill, Modified spin-echo method for measuring nuclear relaxation times. Rev. Sci. Instrum. **29**, 688-691 (1958)

[23] E. L. Hahn, Spin echoes. Phys. Rev. **80**, 580-594 (1950)

[24] N. Bloembergen, E. M. Purcell, R. V. Pound, Relaxation effects in nuclear magnetic resonance absorption, Phys. Rev. **73**, 679-715 (1947)

[25] N. Ohtori, Y. Kondo, Y. Ishii, Molecular size and shape effects: Rotational diffusion and the Stokes-Einstein-Debye relation. J. Mol. Liq. **314**, 113764 (2020)

[26] A. Einstein, Über die von der moleukularkinetischen Theorie der Wärme geforderte Bewegung von in ruhenden Flüssigkeiten suspendierten Teilchen. Ann. Phys. **322**, 549-560 (1905)

[27] I. Solomon, Relaxation processes in a system of two spins. Phys. Rev. **99**, 559-566 (1955)

[28] F. Kramer, M. V. Deshmukh, H. Kessler, S. J. Glaser, Residual dipolar coupling constants: An elementary derivation of key equations. Concepts Magn. Reson. Part A. **21**, 10-21 (2004)

[29] G. E Pake, Nuclear resonance absorption in hydrated crystals: Fine structure of the proton line. J. Chem. Phys. **16**, 327-336 (1948)

[30] T. Polenova, R. Gupta, A. Goldbourt, Magic angle spinning NMR spectroscopy: A versatile technique for structural and dynamic analysis of solid-phase systems. Anal. Chem. **87**, 5458-5469 (2015)

[31] N. Bloembergen, L. O. Morgan, Proton relaxation times in paramagnetic solutions. Effects of electron spin relaxation. J. Chem. Phys. **34**, 842-850 (1961)

[32] H. S. Gutowsky, D. W. McCall, C. P. Slichter, Coupling among nuclear magnetic dipoles in molecules. Phys. Rev. **84**, 589-590 (1951)

[33] N. F. Ramsey, E. M. Purcell, Interactions between nuclear spins in molecules. Phys. Rev. **85**, 143-144 (1952)

[34] J. Kowalewski, L. Mäler, *Nuclear Spin Relaxation in Liquids: Theory, Experiments, and Applications. 2nd Ed*. (Taylor & Francis, Florida, USA, 2018)

Chapter 2: Rapid Descents: Data Processing in NMR

2.1 Introduction

As explained in the prior chapter, the time-domain signals of NMR relaxometry experiments recover or damp exponentially according to the solutions of the Bloch equations [1]. With a wide range of possible interactions driving relaxation, transients may vary anywhere in complexity from a simple monoexponential decay to a seemingly continuous distribution of damping exponentials. A wealth of physical insights exists hidden in the acquired data which leads to one of the primary problems of relaxometry – how does one reliably analyze such complex data? Several algorithms have been employed to varying degrees of success in attempts to retrieve as much information as possible from these transients. This chapter aims to explore common data analysis methods in NMR relaxometry to help contextualize the advancements in data processing which serve as the focus of the first major section of this dissertation.

2.2 Least Squares Regression

2.2.1 Ordinary Least Squares

The tried and true methods of ordinary least squares (OLS) regression and non-linear least squares regression dominated data analysis in the early years of NMR relaxometry [2,3]. For systems with a single relaxation environment, linearization of the data is easily achieved by taking the logarithm of the time-dependent signal, *s(t)*, yielding the relationship

$$\ln[s(t)] = -Rt \tag{2.1}$$

where the slope is the desired relaxation rate, R. This makes single component data a prime candidate for the application of linear regression models [4,5].

Consider a univariate linear regression model with a y-intercept of 0, $y_k = x_k\beta + \varepsilon_k$, with the kth observation of the dependent variable y_k, independent variable x_k, residuals ε_k, and coefficient β, In an ideal scenario, the fit "predicted" by $x_k\beta$ is exact with $\varepsilon_k = 0$. The responses of real experiments, however,

always have some degree of unpredictable variation due to noise which must be considered. Ordinary Least Squares, as well as all other forms of least squares regression to be discussed, uses the sum of square residuals (SSR) as a goodness-of-fit test.

$$SSR(\beta) = \sum_{k=1}^{K} |y_k - x_k\beta|^2 = \sum_{k=1}^{K} |\varepsilon_k|^2 \tag{2.2}$$

The "best" fit is estimated to occur when β minimizes SSR as this is effectively equivalent to minimizing the variance therefore reducing the variables which cannot be accounted for by the model.

$$\hat{\beta} = \underset{\beta}{\operatorname{argmin}}\, SSR(\beta) \tag{2.3}$$

When this global minimum is found, the coefficient $\hat{\beta}$ is referred to as the OLS estimator. The OLS estimator is only considered valid and unbiased when three key assumptions are made according to the Gauss-Markov theorem: the mean of the noise is the zero, all errors are uncorrelated, and the variance of the noise is finite and static. Most noise in NMR relaxometry experimental data meets these requirements making this simple OLS regression model a suitable algorithm for the estimation of a single relaxation component by a simple substitution of Eq. 2.1 into Eq. 2.3

$$\hat{R} = \underset{R}{\operatorname{argmin}} \sum_{k=1}^{K} |\ln[S(t)]_k - t_k R|^2 . \tag{2.4}$$

OLS regression is easily extended to complex, multivariate linear problems. To account for Q individual regressors $x_{q,k}$ for a given data point k, the general linear model is defined by

$$y_k = \beta_0 + x_{1,k}\beta_1 + x_{2,k}\beta_2 + \cdots + x_{Q,k}\beta_Q + \varepsilon_k \tag{2.5}$$

where β_0 corresponds to the estimate of the y-intercept. Expressing this model in matrix form, Eq. 2.6, makes the solution to the multivariate form of OLS more apparent.

$$\vec{y} = \boldsymbol{X}\vec{\beta} + \vec{\varepsilon} \tag{2.6}$$

The $K\times 1$ vectors $\vec{y}$ and $\vec{\varepsilon}$ represent the dependent variable and errors for K total observations. $\boldsymbol{X}$ is a $K\times Q$ matrix of the set of regressors with a corresponding vector $\vec{\beta}$ of coefficients of size $1\times Q$. For data anticipated to possess a non-zero y-intercept, all elements of the first column must possess a value of one

in accordance with Eq. 2.5. Similar to the prior linear model, the OLS estimator is determined by finding the set of coefficients which minimizes SSR.

$$\hat{\beta} = \underset{\vec{\beta}}{\operatorname{argmin}} \left\| \vec{y} - \boldsymbol{X}\vec{\beta} \right\|^2 = \underset{\vec{\beta}}{\operatorname{argmin}} \|\vec{\varepsilon}\|^2 \tag{2.7}$$

The solution to this minimization problem takes on the final form of

$$\hat{\beta} = \vec{\beta} + (\boldsymbol{X}^T\boldsymbol{X})^{-1}\boldsymbol{X}^T\vec{\varepsilon}. \tag{2.8}$$

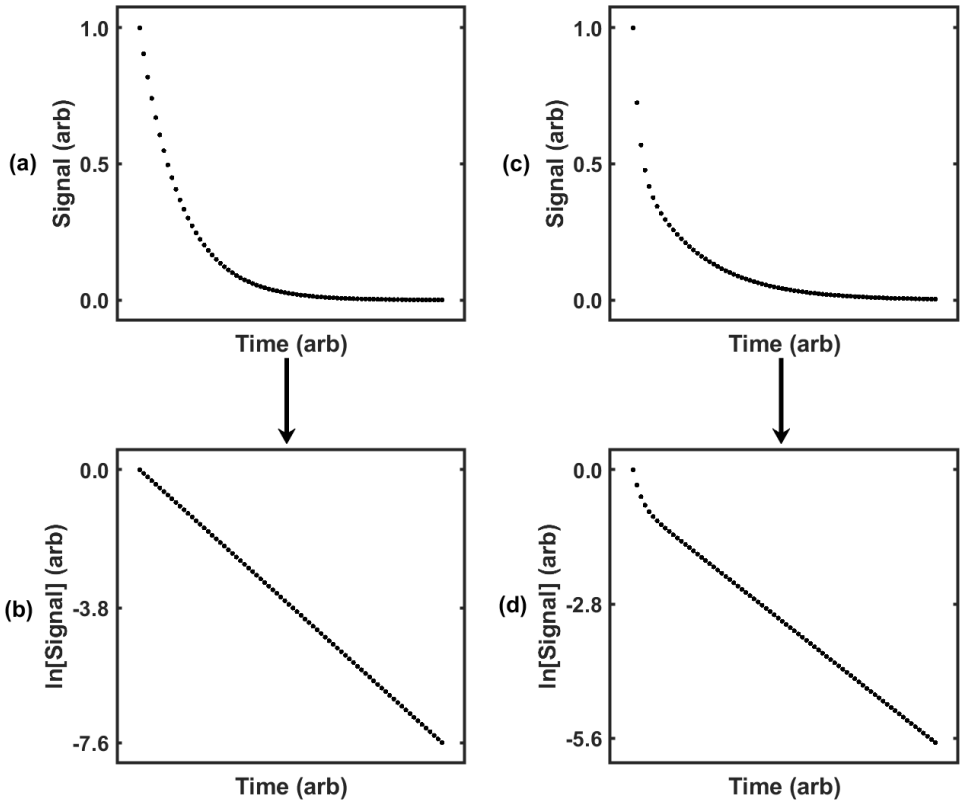

Figure 2.1. *Comparison of (a) monoexponential and (c) biexponential decays and their corresponding logarithms, (b) and (d).*

Unfortunately, the OLS method is not applicable to more complicated relaxometry signals. As demonstrated by plots Figs. 2.1(c) and 2.1(d), systems with more than one relaxation component do not linearize when the logarithm of the transient is taken. The non-linearity is a consequence of the additive nature of each environment's signal contribution [3]. The total signal is modelled by

$$s(t) = \sum_{n=0}^{N} A_n e^{-R_n t} \tag{2.9}$$

where R_n is the n^{th} relaxation rate out of N total components and A_n is the respective weight of the contribution. Alternative non-linear data processing methods, such as non-linear least squares regression, must be contemplated.

2.2.2 Non-linear Least Squares

Briefly mentioned in the previous section, the non-linear least squares (NLS) method shares the same goal as OLS [4]. That is the "best" fit estimator for NLS is determined by minimization of SSR. The simplicity of the OLS model makes it an analytically solvable problem, a feature that is absent in nonlinear problems. Consider briefly the smallest multicomponent relaxation system described by the equation

$$s(t) = A_1 e^{-R_1 t} + A_2 e^{-R_2 t}. \tag{2.10}$$

Whereas the single component scenario possesses only one unknown variable, the two component case is underdetermined with 4 coefficients and one equation. With no way to linearize the function, it is not possible to analytically solve for all unknown variables. This leads to the main difference in how linear and non-linear data must be treated – the NLS method takes an iterative approach to find the best fit as a function of each variable [5].

One common algorithm for the application of NLS is the Levenberg-Marquardt algorithm [6,7]. The Levenberg-Marquardt algorithm is an amalgamation of the Gauss-Newton and Gradient Descent routines for optimization [8,9]. As is standard for many iterative approaches, an initial guess for each parameter to be fit is required. The difference between these three optimization methods is how the parameters are adjusted at each step.

The Gauss-Newton method assumes the solution $\hat{\beta}$ is near the current guess $\vec{\beta}_q$ [8]. For sufficiently small adjustments of the parameters, the non-linear problem can be recontextualized as a linear problem using a first-order Taylor expansion of $\vec{\varepsilon}$ about the current guess.

$$\vec{\beta}_{q+1} = \underset{\vec{\beta}}{\operatorname{argmin}} \left\| \vec{\varepsilon}_q + \boldsymbol{J}(\vec{\varepsilon}_q)(\vec{\beta} - \vec{\beta}_q) \right\|^2 \tag{2.11}$$

Here, $\boldsymbol{J}$ is the Jacobian matrix of first-order partial derivatives. With the return to a linear format, solving for the new guess vector, $\vec{\beta}_{q+1}$, can be treated as an OLS problem yielding the following solution:

$$\vec{\beta}_{q+1} = \vec{\beta}_q - \left(\boldsymbol{J}(\vec{\varepsilon}_q)^T \boldsymbol{J}(\vec{\varepsilon}_q) \right)^{-1} \boldsymbol{J}(\vec{\varepsilon}_q)^T \vec{\varepsilon}_q \tag{2.12}$$

Taking $\vec{\beta}_{q+1} - \vec{\beta}_q$ leaves the correction that determines the guess vector for the next iteration, $\vec{\delta}_{GN}$.

$$\vec{\delta}_{GN} = -\left(\boldsymbol{J}(\vec{\varepsilon}_q)^T \boldsymbol{J}(\vec{\varepsilon}_q) \right)^{-1} \boldsymbol{J}(\vec{\varepsilon}_q)^T \vec{\varepsilon}_q \tag{2.13}$$

The key selling point of the Gauss-Newton method is bypassing the calculation of Hessian matrices which heavily increase computational costs. With a proper guess, this algorithm converges rapidly. However, in the event that the initial guess is too far from the solution, the core approximation of this method is no longer valid, and the algorithm may fail to converge as tiny steps are taken.

On the opposite end of the optimization grid, is the gradient descent algorithm which increments the guess parameters proportionally to the steepest slope of a locally linear function [9]. Here the adjustment to $\vec{\beta}_q$ is calculated simply as

$$\vec{\delta}_{GD} = -\gamma_q \boldsymbol{J}(\vec{\varepsilon}_q) \tag{2.14}$$

where γ_q is the learning rate of the algorithm. While this method always drives towards minimum, the efficiency strongly depends on the choice of learning rate. If the learning rate is too high, divergent behavior may arise due to jumps that are too large. If the learning rate is too low, it may not only take eons to reach a solution, but the chance of falling into a local minimum increases.

The Levenberg-Marquardt method modifies the Gauss-Newton algorithm by introducing a scalar damping parameter, λ, in the form of a penalty term where the identity matrix, $\boldsymbol{I}$, adds bias towards solutions with smaller norms [6,7].

$$\vec{\beta}_{q+1} = \underset{\vec{\beta}}{\operatorname{argmin}} \left(\left\| \vec{\varepsilon}_q + \boldsymbol{J}(\vec{\varepsilon}_q)(\vec{\beta} - \vec{\beta}_q) \right\|^2 + \left\| \lambda \boldsymbol{I} \vec{\beta}_q \right\|^2 \right) \tag{2.15}$$

The adjustment to $\vec{\beta}_q$ is now calculated as

$$\vec{\delta}_{LM} = -\left(\boldsymbol{J}(\vec{\varepsilon}_q)^T \boldsymbol{J}(\vec{\varepsilon}_q) + \lambda \boldsymbol{I}\right)^{-1} \boldsymbol{J}(\vec{\varepsilon}_q)^T \vec{\varepsilon}_q. \tag{2.16}$$

By tuning λ, the strengths of both the Gauss-Newton and gradient descent can be utilized. After each step, λ is actively altered by an additional factor, υ, to reflect the current change in SSR. Note that as λ decreases, Eq. 2.15 approaches the standard solution to the Gauss-Newton algorithm. Conversely, if λ is significantly increased, the damping term overwhelms the Hessian approximation, $\boldsymbol{J}^{\mathrm{T}}\boldsymbol{J}$, and Eq. 2.15 approaches the gradient descent solution.

Figure 2.2 summarizes the standard procedure for the Levenberg-Marquardt algorithm. First, the parameters $\vec{\beta}_q$ and λ are initialized and the value of υ is set. The residuals and the corresponding Jacobian matrix for the initial guess are calculated and the adjustment $\vec{\delta}_{LM}$ is determined and added to $\vec{\beta}_q$. The residuals for $\vec{\beta}_{q+1}$ are calculated and the SSR is compared to the previous step. A decrease in SSR at the new step suggests that the algorithm is converging towards a minimum, thus the damping parameter is decreased by a factor of υ to accelerate the process. $\vec{\beta}_{q+1}$ is accepted as the new guess parameter and the algorithm moves to the next iteration. If SSR has increased, the new guess parameter is rejected and λ is instead increased by a factor of υ. The next iteration then calculates a new parameter adjustment using the new damping parameter, but the old coefficient guess. This algorithm repeats until a set tolerance is satisfied. The Levenberg-Marquardt algorithm has become a standard method for the analysis of nonlinear transients in NMR. However, the performance of this algorithm is dependent on not only the initialized parameters, but the model function for the data must also be guessed. Combined with the introduction of constraints to ensure only physical solutions, NLS can easily accumulate in computation cost and solution variability.

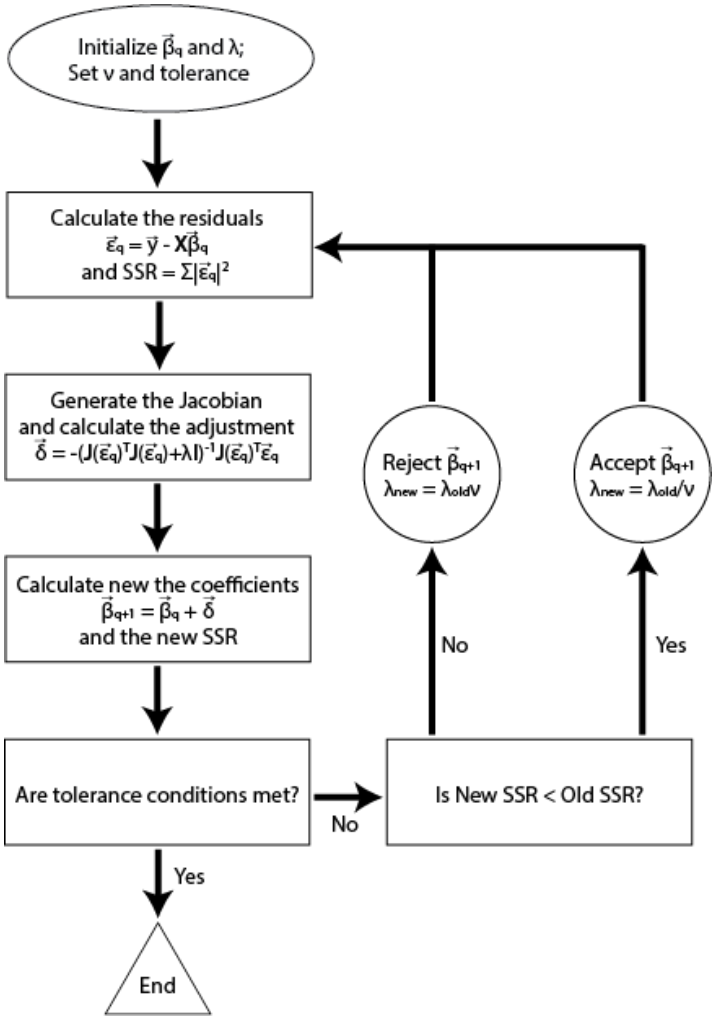

Figure 2.2. *The Levenberg-Marquardt algorithm for the method of non-linear least squares regression.*

2.3 Inverse Laplace Transforms

While the treatment of relaxation rates thus far has assumed a discrete distribution, in reality there is far more nuance in the environments of spins [10]. The relaxation rates which are typically reported are an average of the rates experiences by spins in similar environments [11]. When viewed from this perspective, it becomes clear that the distribution of rates may be more continuous in nature. By summing all of these possible rates, the total signal can be expressed as

$$s(t) = \int_0^\infty P(R)e^{-Rt}dR \tag{2.17}$$

where $P(R)$ is the probability distribution of possible rates. Note the similarity to an inverse Fourier transform (Eq. 2.18) in which a function of frequency is converted to a function of time.

$$f(t) = \frac{1}{2\pi} \int_{-\infty}^{\infty} F(\omega) e^{-i\omega t} d\omega \tag{2.18}$$

Fourier transforms can be considered to be a special case of another transformation, the Laplace transform.

The main divergence between these transformations is related to the frequency domain [12]. Whereas the Fourier transform only observes frequencies from the imaginary axis, the Laplace transform looks at the full complex domain of frequencies. This crucial difference is clear when comparing the exponential functions of Eq. 2.17 and 2.18. For the case of relaxation, the signal as a continuous distribution of rates is a special form of the inverse Laplace Transform (ILT) in which only the real axis of frequencies are considered.

With a continuous set of rates, it is only necessary to calculate the relative weights for each rate to model the total signal. Once again, the signal cannot be linearized and obtaining an analytical solution is not possible. This problem must be approximated using discretized, non-linear methods, such as NLS. However, it is possible to restrict the scope of this problem to improve computational costs and the accuracy of results. Returning to Eq. 2.10, consider the physical values that are possible for each parameter [11]. A_1 and A_2 are the populations of particles undergoing the respective relaxation rates of R_1 and R_2. Note that all of these parameters must be positive values in order to reflect a physical system. If the least squares algorithm is constrained to coefficients greater than or equal to zero, this becomes a non-negative least squares (NNLS) problem [4].

2.3.1 Lawson-Hanson Algorithm

One of the most prevalent algorithms for solving NNLS problems is the Lawson-Hanson algorithm as described in figure 2.3 [4,13]. This algorithm keeps track of which coefficients presently satisfy the

constraint conditions by defining two sets of indices. Set $\mathbb{P}$, called the passive set, possess the indices of coefficients which are positive and the active set $\mathbb{R}$ contains the remaining indices. Consider a least square problem with *K* observations and *Q* coefficients. In the initialization of this algorithm, $\mathbb{P}$ is a null set and $\mathbb{R}$ = {1, 2, …, *Q*}. The initial guess of parameters $\vec{\beta}_q$ is a vector of zeros. The final piece of the initialization is the calculation of

$$\vec{w} = \boldsymbol{X}^T\left(\vec{y} - \boldsymbol{X}\vec{\beta}_q\right) \tag{2.19}$$

The vector $\vec{w}$ functions as a set of Lagrange multipliers with subvectors $\vec{w}_{\mathbb{P}}$ and $\vec{w}_{\mathbb{R}}$ composed of only the elements corresponding to their respective index sets.

The primary loop of the Lawson-Hanson algorithm continues until two conditions are met – the active set is null and the highest valued element of $\vec{w}_{\mathbb{R}}$ is below a set tolerance. The iterative process solves the least squares problem for a newly defined subset of regressors**,** $\boldsymbol{X}_{\mathbb{P}}$**,** at each step until an optimized solution is found. The routine starts by choosing an index *n* to transfer from set $\mathbb{R}$ to $\mathbb{P}$ via

$$n = \text{argmax}(\vec{w}_{\mathbb{R}})\,. \tag{2.20}$$

$\boldsymbol{X}_{\mathbb{P}}$ is then generated by taking the regressors corresponding to the indices in set $\mathbb{P}$. A respective subset of coefficients $\vec{\beta}_{\mathbb{P}}$ are calculated in a standard least squares fashion.

$$\vec{\beta}_{\mathbb{P}} = \left(\boldsymbol{X}_{\mathbb{P}}^T\boldsymbol{X}_{\mathbb{P}}\right)^{-1}\boldsymbol{X}_{\mathbb{P}}^T\vec{y} \tag{2.21}$$

The complimentary subset $\vec{\beta}_{\mathbb{R}}$ is a vector of zeros. The new vector of coefficients $\vec{\beta}_{q+1}$ is then constructed by the combination of $\vec{\beta}_{\mathbb{P}}$ and $\vec{\beta}_{\mathbb{R}}$. However, this least squares solution is unconstrained meaning there is a small chance that the calculated coefficients are negative.

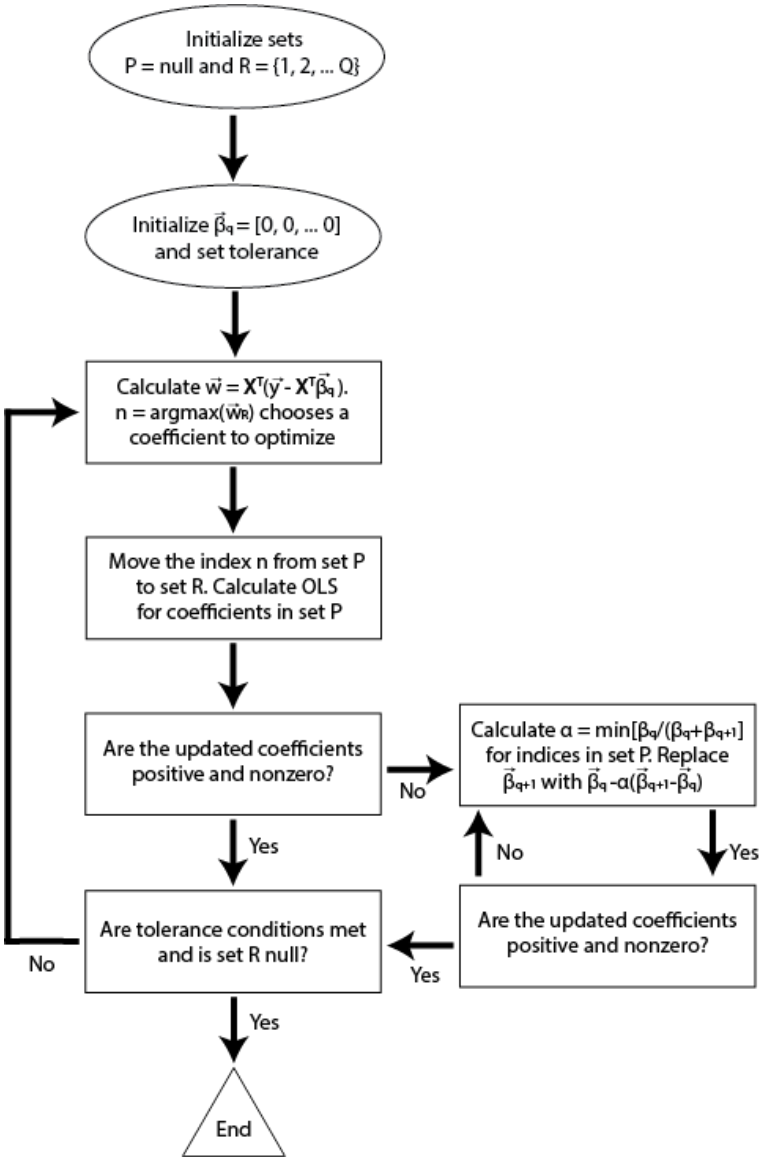

Figure 2.3. *The Lawson-Hanson algorithm for the method of non-negative least squares regression.*

In the event that any coefficient is negative or zero, a subroutine is opened to determine a new set of coefficients which satisfy the constraints while also improving the fit. In this inner loop, an alternative set of coefficients is calculated by utilizing both the unconstrained solution and the previous guess. $\vec{\beta}_q$ is replaced by the calculation of $\vec{\beta}_q - \alpha(\vec{\beta}_{q+1} - \vec{\beta}_q)$ where the new parameter α is dependent on the $\mathbb{P}$ subsets of the new and old coefficients.

$$\alpha = \min\left(\frac{\vec{\beta}_{q,\mathbb{P}}}{\vec{\beta}_{q,\mathbb{P}} - \vec{\beta}_{q+1,\mathbb{P}}}\right) \tag{2.22}$$

The index sets are updated based on the new values of $\vec{\beta}_q$ where the indices of any remaining zero or negative coefficients are moved to $\mathbb{R}$ and a new $\vec{\beta}_{q+1}$ is calculated via the prior method. This inner loop continues until all coefficients of $\vec{\beta}_{q+1}$ are positive. Once a solution is acceptable, $\vec{w}$ is calculated for the new parameters and the algorithm loops until the end conditions of the main loop are satisfied.

The ILT currently serves as the gold standard of transient analysis in NMR relaxometry [14]. This method excels in very complex environments where many relaxation rates are expected. The utility of the ILT has helped extend the scope of low field NMR towards not only distributions of relaxation rates, but into looking at the physical properties of porous materials, emulsions, and other complicated samples [15,16]. However, the ILT suffers from a few significant drawbacks: 1) large data sets can often accumulate high computational cost, 2) the solutions yield continuous estimations even for discrete systems, and 3) the solutions can be incredibly unstable with respect to noise when unmodified.

As is common with inversion problems, the ILT is an ill-posed problem [14]. The set of exponential functions that build the regressor matrix are closely related in decay rates. As a consequence, several solutions may provide a sufficient fit to the signal making it difficult to discern the correct one. Additionally, issues arise from the physical constraints imposed on the exponentials. In the analysis of a CPMG transient, for example, all functions in the regressor are decaying such that the slope of the tangent line at each point is always negative. In contrast, real data possesses noise which causes an apparent random fluctuation in slopes. Attempting to model this behavior with only decaying functions leads to increased instability.

2.3.2 Tikhonov Regularization

Several methods have been applied to enhance the stability of the ILT, however regularization is a dominating presence in NMR data analysis. An example of regularization is the Levenberg-Marquardt algorithm and the introduction of the penalty term to the Gauss-Newton method [6,7]. By introducing a

bias to the least squares problem, the number of possible solutions are reduced thereby increasing the stability of the algorithm. Regularization comes in multiple flavors which highlight different features of modelled data [18].

The easiest to implement and most common in NMR is L2 regularization, also known as Tikhonov regularization or Ridge regression [19-22]. Tikhonov regression adds a penalty term to the least squares problem which is related to the square of the Euclidian norm of the coefficients.

$$\hat{\beta} = \underset{\vec{\beta}}{\operatorname{argmin}} \left(\left\| \vec{y} - \boldsymbol{X}\vec{\beta} \right\|^2 + \lambda \left\| \boldsymbol{\Gamma}\vec{\beta} \right\|_2^2 \right) \tag{2.23}$$

L2 regression for a linear least squares fit is exactly solvable yielding:

$$\hat{\beta} = (\boldsymbol{X}^T\boldsymbol{X} + \lambda\boldsymbol{\Gamma}^T\boldsymbol{\Gamma})^{-1}\boldsymbol{X}^T\vec{y} \tag{2.24}$$

The regularization matrix, $\boldsymbol{\Gamma}$, enforces a preference towards more unique solutions by dampening the functions which are most influenced by the noise. This effect appears as a strong reduction of certain coefficients in the solution.

Typically, as demonstrated in the Levenberg-Marquardt case, $\boldsymbol{\Gamma}$ is often chosen to be the identity matrix reducing Eq. 2.24 to

$$\hat{\beta} = (\boldsymbol{X}^T\boldsymbol{X} + \lambda\boldsymbol{I})^{-1}\boldsymbol{X}^T\vec{y}. \tag{2.25}$$

This is referred to as the standard form of Tikhonov regularization. Other common choices for the regularization matrix are the finite difference matrix operators which approximate derivatives. The finite difference matrices function as smoothing operators, thus highlighting more continuous features. The choice in $\boldsymbol{\Gamma}$ for NMR data analysis comes down to *a priori* knowledge about the complexity of the sample. A sample with a discrete set of relaxation rates prefers the standard form of Tikhonov regularization.

The regularization parameter, λ, acts as the Lagrange multiplier of the newly imposed constraints. As λ increases, the less desirable elements of the coefficients decrease more effectively diminishing the contribution of certain functions to the final solution. The choice of λ is crucial as too much regularization can lead to underfitting. In the case of L2 regression, no coefficient can be completely reduced to zero and

thus $\hat{\beta}$ remains dense. As a consequence, L2 solutions for discrete relaxation systems will always present as broadened peaks.

2.3.3 Lasso Regression

Another form of regularization is L1 regression, or lasso regression [20,23]. Similar to L2 regression, a penalty term is introduced to the least squares problem.

$$\hat{\beta} = \underset{\vec{\beta}}{\operatorname{argmin}} \left(\left\| \vec{y} - \boldsymbol{X}\vec{\beta} \right\|^2 + \lambda \left\| \boldsymbol{\Gamma}\vec{\beta} \right\|_1 \right) \tag{2.26}$$

Here, the absolute value norm is introduced to constrain the vector of coefficients. Unlike L2 regression, the elements of $\hat{\beta}$ may be reduced to zero thus introducing sparsity. This is beneficial to simple systems such as a mixture with few relaxation rates as the solutions will tend to present narrower peaks more reminiscent of the true distribution. However, L1 regression has a two notable drawbacks. First is that it is not analytically solvable. Consequently, additional numerical methods must be applied to reach a solution. Second, while this regularization does reduce the number of possible solutions, there is no guarantee that a unique solution exists. If two or more possible solutions exist, one is chosen at random.

2.3.3 Elastic Net Regularization

In cases where distributions have both discrete and continuous features, L1 and L2 regularization will tend to lean heavily towards one property. There exists a hybrid of the two methods that allows for an intermediate degree of sparsity known as naïve elastic net regularization [24].

$$\hat{\beta} = \underset{\vec{\beta}}{\operatorname{argmin}} \left(\left\| \vec{y} - \boldsymbol{X}\vec{\beta} \right\|^2 + \lambda_1 \left\| \boldsymbol{\Gamma}\vec{\beta} \right\|_1 + \lambda_2 \left\| \boldsymbol{\Gamma}\vec{\beta} \right\|_2^2 \right) \tag{2.27}$$

Here, both the lasso and Tikhonov penalty terms are included with their own regularization parameters. The naïve elastic net problem can be broken into two steps – first the L2 term is used to group highly correlated coefficients which express more continuous features, then the L1 term performs the role of variable selection. At each stage of the calculation, the coefficients undergo shrinkage which in turn introduces

additional bias that is not present when solely utilizing L1 or L2 methods. The naïve elastic net tends to underperform as a result of this double shrinkage, only providing reasonable results when the regular parameters approach one of the regression extremes. A standard method to account for this increased bias is to simply scale $\hat{\beta}$ by the following:

$$\hat{\beta}' = (1 + \lambda_2)\hat{\beta} \tag{2.28}$$

This minute modification maintains all the properties of the naïve elastic net solution, but greatly enhances the predictive power. This scaled version of the problem is referred to as elastic net regularization.

2.4 The Matrix Pencil Method

While the ILT has proven to be a powerful force in NMR analysis, in most situations it is a case of applying a continuous method to a discrete system. Between stability issues and, especially for large data sets, high computational costs, alternative methods have recently entered the NMR space. One such method is the matrix pencil method (MPM) [25,26]. MPM is a relatively young technique which has found prominence in time-domain signal analysis due to its ability to handle the complex exponential functions which are central to this thesis [27].

Consider the signal for a sample with a single relaxation component and the relationship at two points in time,

$$e^{-Rt_2} = e^{-R(t_1+\Delta t)} \tag{2.29}$$

where Δt is a fixed increment between the two points. Using the properties of exponents, Eq. 2.29 can also be expressed as

$$e^{-Rt_2} = e^{-R\Delta t}e^{-Rt_1}. \tag{2.30}$$

Because the relaxation rate and the time increment are fixed values, $e^{-R\Delta t}$ is a scalar quantity which will now denoted as λ. This revelation reveals that any two points in a monoexponentially decaying function are proportional to each other. In other words, Eq. 2.30 can be treated as a linear relationship.

$$s(t_1) = \lambda s(t_2) \tag{2.31}$$

Barring noise, one only needs two points in a data set to calculate λ which can itself be used to calculate the exponential decay rate via

$$R = -\frac{\Delta t}{\ln(\lambda)} \tag{2.32}$$

This is the core concept behind the function of the matrix pencil method.

Moving to a mixture of two relaxation components, it becomes immediately clear that that solving for these rates is no longer so easy.

$$A_1 e^{-R_1 t_2} + A_2 e^{-R_2 t_2} = \lambda_1 A_1 e^{-R_1 t_1} + \lambda_2 A_2 e^{-R_2 t_1}. \tag{2.33}$$

There are now individual scalars and weights for each exponential that makes up the overall signal which, as discussed in section 2.1, is not analytically solvable with only one equation. Consider now, that the total signal is a linear combination of linear equations, or a linear system of equations. By detangling each contribution and looking at these linear problems individually, each term in the signal can be treated in a similar manner to Eq. 2.32.

To accomplish this, the MPM method starts by expressing the total signal as a matrix, to be denoted as $\boldsymbol{Y}$.

$$\boldsymbol{Y} = \begin{pmatrix} Y(1,1) & \cdots & Y(1,m) \\ \vdots & \ddots & \vdots \\ Y(n,1) & \cdots & Y(n,m) \end{pmatrix} \tag{2.34}$$

Two-dimensional data sets are inherently matrices, while one-dimensional data sets are vectors. In line with the content of this thesis, the one-dimensional variant of MPM will be discussed. Generally, the one-dimensional transients are transformed into the form of a Hankel matrix with dimensions $n \times n$ for this context. The matrix $\boldsymbol{Y}$ can be broken into two submatrices which represent a shift in time reflective of the two points in time in Eq. 2.31:

$$\boldsymbol{Y_1} = \begin{pmatrix} Y(1,1) & \cdots & Y(1,m-1) \\ \vdots & \ddots & \vdots \\ Y(n,1) & \cdots & Y(n,m-1) \end{pmatrix} \tag{2.35}$$

and

$$\boldsymbol{Y_2} = \begin{pmatrix} Y(1,2) & \cdots & Y(1,m) \\ \vdots & \ddots & \vdots \\ Y(n,2) & \cdots & Y(n,m) \end{pmatrix}. \tag{2.36}$$

This pair of equally-sized submatrices are referred to as a matrix pencil [28]. This name stems from an old definition of pencil which refers to a convergence of properties, in this case these submatrices are related in time.

From this matrix form, the signal can now be decomposed into its individual contributions by a transformation into a generalized eigenvalue problem [28].

$$\boldsymbol{Y_2}\vec{p}_i = \lambda_i \boldsymbol{Y_1}\vec{p}_i \tag{2.37}$$

$\vec{p}_i$ is the eigenvector corresponding to a specific relaxation component and λ_i is the respective eigenvalue. By rearranging Eq. 2.37, a familiar equation appears:

$$\boldsymbol{Y_1}^{-1}\boldsymbol{Y_2}\vec{p}_i = \lambda_i \vec{p}_i. \tag{2.37}$$

This is the standard eigenvalue problem which is solved by diagonalization methods. Here, the eigenvalues represent the same scalars presented previously, thus all relaxation rates can be calculated via Eq. 2.32. It is important to note that $\boldsymbol{Y_1}^{-1}$ often cannot be directly calculated, so the pseudoinverse is used in its place.

To calculate the relative weights for each relaxation component, consider an alternative way to model the signal for N relaxation:

$$s(i-1) = \sum_{n=1}^{N} A_n \lambda_n^{i-1} \tag{2.38}$$

Because the time increments are constant for MPM, the total signal can be built purely by the powers of the eigenvalues. By constructing a pair of Vandermonde matrices from these powers of eigenvalues up to P time points, $\mathbf{Z_L}$ and $\mathbf{Z_R}$, the amplitude matrix is calculated via

$$\boldsymbol{A} = \boldsymbol{Z_L^{-1}} \boldsymbol{Y} \boldsymbol{Z_R^{-1}} \tag{2.39}$$

For a one-dimensional transient, $\mathbf{Z_R}$ is the transpose of $\mathbf{Z_L}$ where

$$\boldsymbol{Z_L} = \begin{pmatrix} \lambda_1^0 & \cdots & \lambda_N^0 \\ \vdots & \ddots & \vdots \\ \lambda_1^P & \cdots & \lambda_N^P \end{pmatrix} \tag{2.40}$$

To effectively apply the matrix pencil method, it is important to note how noise presents itself in the MPM solutions. As mentioned previously, the decay rates of these models only represent physical relaxation rates when real and positive which means ideal behavior is monotonic. The data begins to fluctuate resulting in additional complex decay rates once noise is introduced. As a consequence, some eigenvalues produced by MPM may become complex themselves. Keeping all of these eigenvalues will result in an exact model of the noisy data, however, very little information can be gained about the physical properties of the system. The underlying monotonic behavior of the data is masked due to an increase in matrix rank when noise is added.

To account for this, the rank of the data matrix must be reduced to a predicted size based on an estimated number of relaxation components prior to solving the generalized eigenvalue problem. This reduction is accomplished by the application of Singular Value Decomposition (SVD) as a filter [29]. SVD functions similar to an eigenvalue decomposition as it factorizes a matrix into its characteristic vectors, however SVD is not restricted to square matrices and therefore the diagonal matrix can include singular values [30]. $\boldsymbol{Y}$ is deconstructed into the left and right matrices of singular vectors, $\boldsymbol{U}$ and $\boldsymbol{V}$, and the singular value matrix $\boldsymbol{\Sigma}$.

$$\boldsymbol{Y} = \boldsymbol{U}\boldsymbol{\Sigma}\boldsymbol{V}^{*} \qquad (\mathbf{2.41})$$

If the size of each matrix is restricted by the number of relaxation components, such as reducing S to 2×2 for two physical rates, the corresponding reconstruction of the data matrix will be reduced in both noise and rank

Proper SVD filtering will prompt MPM to produce only physical eigenvalues. The computational cost of the MPM algorithm is very low, so typically one can just iterate through several guesses for the number of rates based on *a priori* information. The best rank results in the highest number of real and positive eigenvalues. Methods such as minimum description length have been employed previously to determine the optimal rank without the need for prior information, but these methods have not been utilized in the work to be discussed [26].

When comparing ILT and MPM, one cannot be treated as objectively superior. The ILT does suffer from much higher computational costs and more instability than MPM, however ILT shines when solutions are expected to be dense. For continuous distributions, MPM runs into the opposite issue of ILT in that a discrete solution is applied to a continuous problem. The transient for a system with hundreds relaxing components can often be reasonably modeled by a reduced set of exponentials. The MPM algorithm tends to find a solution with the minimum number of rates required to effectively reconstruct the signal. As a consequence, attempting to recover the rates for a continuous distribution yields only a fraction of the components, generally no more than about 10 rates. Thus, the current power of MPM lies in the analysis of simpler systems. However, there is still a desire to try to implement MPM to the analysis of these dense problems.

2.5 Filtering

To conclude this chapter on techniques for NMR data analysis, a couple of filtering methods will be briefly discussed. Most relaxometry experiments are conducted at low magnetic fields, a regime which is notorious for poor signal-to-noise [31]. In some situations, the trade-off between the amount of noise reduction by signal averaging and the total experimental time are unconscionable. Denoising methods are often applied prior to fitting the data in order to help ensure reliable characterization of the sample.

2.5.1 Apodization

The most common technique applied for noise reduction in NMR is apodization, often referred to as a Fourier filter [31]. Typically, noise in the time domain appears as high frequency artefacts in the frequency domain. By eliminating these high frequency features, the signal noise is effectively reduced in noise. This can be accomplished by the use of appropriate windowing functions. For relaxometry data, the corresponding Fourier transform takes on the shape of a Lorentzian function centered about zero. To maintain the core signal, this spectrum must be convoluted with a function which maintains the center of

the Lorentzian while decreasing any activity on the outer edges. An obvious solution is to use a smooth function with similar behavior such as a Gaussian. With a comparable choice of width, the Gaussian function will reduce any fluctuations at the higher frequencies and keep the main structure. The major drawback to the Fourier filter is that it is highly sensitive. Too much smoothing will inevitably affect the core signal resulting in aliasing as demonstrated in Fig. 2.5. In this situation, it is common to discard the first and last point of the data set.

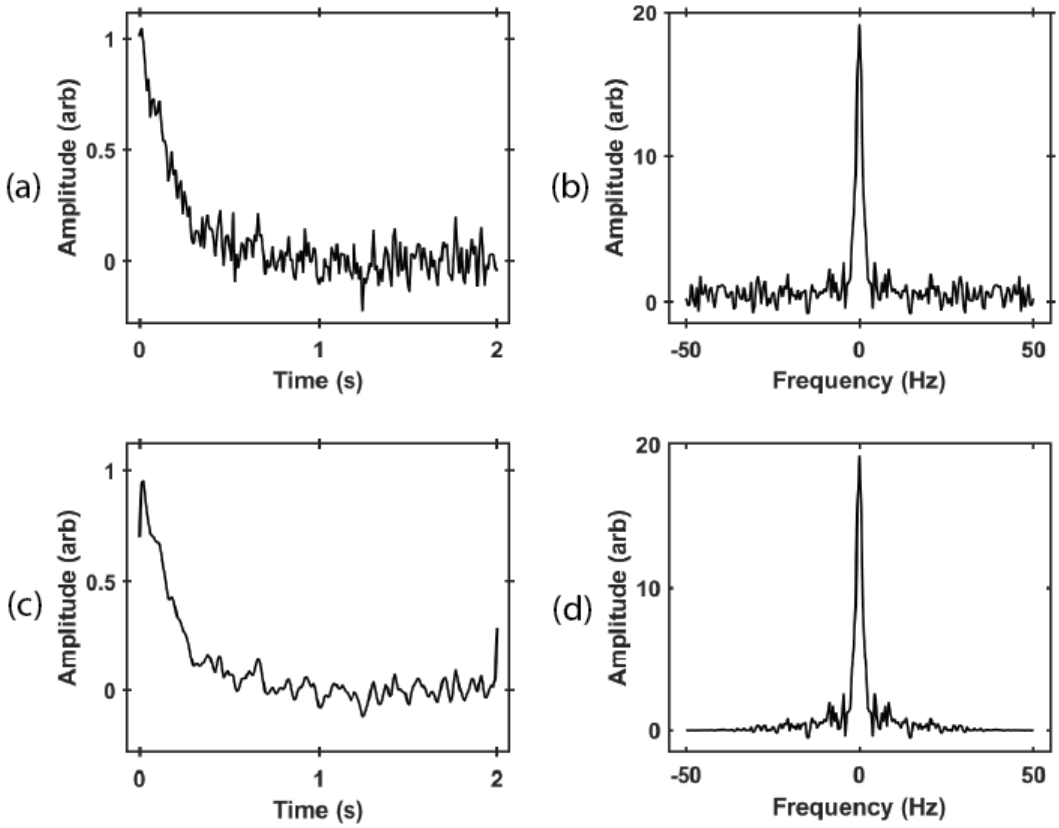

Figure 2.5. *Denoising of a noisy transient by the Fourier filter. Plots (a) and (b) are the raw signal and respective frequency spectrum. Plots (c) and (d) are the results of apodization. Note that while noise has decreased, the end points of the data no longer fit the function.*

2.5.2 Matrix Pencil Filter

A new application of MPM has recently been suggested to bypass the aliasing issue of the Fourier filter [32]. The eigenvalues of the full rank MPM reveals a lot of information about the signal. As mentioned

previously, noise takes on the form of complex eigenvalues with MPM. This in turn produces complex decay rates in which the imaginary component describes a piece of the noise. Discarding the rates with the highest imaginary frequencies and reconstructing the signal eliminates much of the noise. In this way, the MPM can function as a bandpass filter much like the Fourier filter.

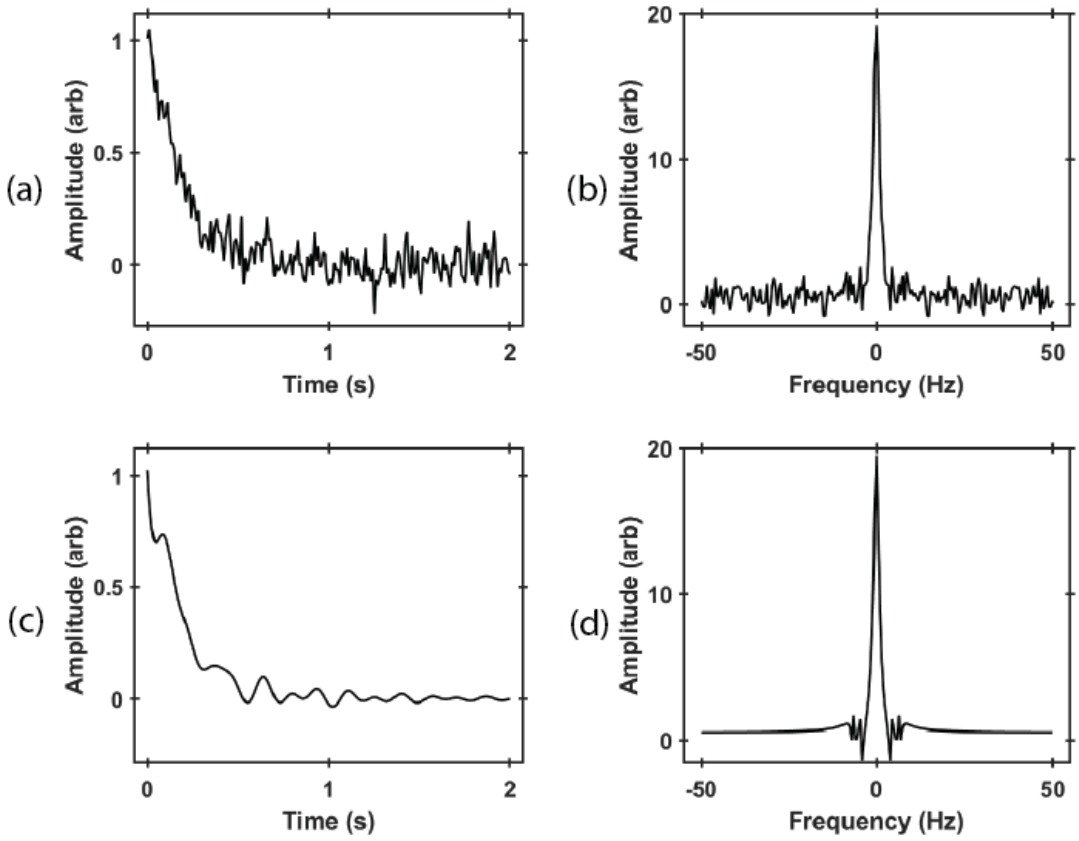

Figure 2.6. *Denoising of a noisy transient by the Matrix Pencil Filter. Plots (a) and (b) are the raw signal and respective frequency spectrum. Plots (c) and (d) are the results of the filter. Note that no major aliasing has occurred with this method.*

The matrix pencil filter (MPF) has one major advantage over apodization – a majority of the core signal contribution comes from the real components of the rates with low imaginary frequencies. In other words, eliminating the noise does not tamper with the underlying signal, and thus this filter does not tend to alias. As shown in Fig. 2.6, MPF is capable of a much higher degree of denoising over the Fourier method.

Inversely, the MPF can also be used to improve spectral features. In the frequency domain, the real component of the decay rates decide the width spectral peaks. Consider a single peak with some form of inhomogeneous broadening. The MPM deconstruction of the corresponding time domain signal yields several rates. By discarding rates in which the real frequencies are high, the components of the signal which contribute to broadening are deleted. In this context, the MPF behaves like a shimming algorithm.

References

[1] F. Bloch, Nuclear induction, Phys. Rev. **70**, 460-474 (1946)

[2] E. L. Hahn, An accurate nuclear magnetic resonance method for measuring spin-lattice relaxation times. **76**, 145-146 (1949)

[3] R. L. Kamman, C. J. G. Bakker, P. van Dijk, G. P. Stomp, A. P. Heiner, H. J. C. Berendsen, Multi-exponential relaxation analysis with MR imaging and NMR spectroscopy using fat-water systems. Magn. Reson. Imaging. **5**, 381-392 (1987)

[4] C. L. Lawson, R. J. Hanson, *Solving Least Squares Problems* (Society for Industrial and Applied Mathematics, New Jersey, USA, 1995)

[5] Å. Björck, *Numerical Methods for Solving Least Squares Problems* (Society for Industrial and Applied Mathematics, Pennsylvania, USA, 1996)

[6] K. Levenberg, A method for the solution of certain non-linear problems in least squares. Q. Appl. Math. **2**, 164-168 (1944)

[7] D. Marquardt, An algorithm for least squares estimation of nonlinear parameters. SIAM J. Appl. Math. **11**, 431-441 (1963)

[8] C. R. Gauss, *Theoria Motus Corporum Coelestium in Sectionibus Conicis Solem Ambientum* (1809) https://archive.org/details/bub_gb_ORUOAAAAQAAJ/page/n3/mode/2up

[9] H. B. Curry, The method of steepest descent for non-linear minimization problems. Q. Appl. Math. **2**, 258-261 (1944)

[10] E. J. Fordham, A. Sezginer, L. D. Hall, Imaging multiexponential relaxation in the (y, $\log_e T_1$) plane with application to clay filtration in rock cores. J. Magn. Reson., Ser. A **113**, 139–150 (1995)

[11] M. H. Levitt, *Spin Dynamics: Basics of Nuclear Magnetic Resonance* (John Wiley and Sons, West Sussex, UK, 2008)

[12] P. M. Morse, H. Feshbach, *Methods of Theoretical Physics, Part I* (McGraw-Hill, New York, USA, 1953)

[13] R. Bro, S. de Jong, A fast non-negativity-constrained least squares algorithm. J. Chemom. **11**, 393-401 (1997)

[14] P. Barone, A. Ramponi, G. Sebastiani, On the numerical inversion of the Laplace transform for nuclear magnetic resonance relaxometry. Inv. Probl. **17**, 77-94 (2001)

[15] A. T. Watson, C. T. P. Chang, Characterizing porous media with NMR methods. Prog. Nucl. Magn. Reson. Spectrosc. **31**, 343-386 (1997)

[16] M. L. Johns, K. G. Hollingsworth, Characterisation of emulsion systems using NMR and MRI. Prog. Nucl. Magn. Reson. Spectrosc. **50**, 51-70 (2007)

[17] S. I. Kabanikhin, Definitions and examples of inverse and ill-posed problems. J. Inv. Ill-Posed Probl. **16**, 317-357 (2009)

[18] L. Reichel, Q. Ye, Simple square smoothing regularization operators. Electron. Trans. Numer. Anal. **33**, 63-83 (2009)

[19] A. Buccini, M. Donatelli, L. Reichel, Iterated Tikhonov regularization with a general penalty term. Numer. Linear Algebra Appl. **24**, 1-19 (2017)

[20] M. Hanke, K. Hansen, P. C. Hensen, Regularization methods for large-scale problems. Surv. Math. Ind. **3**, 253-315 (1993)

[21] G. Huang, L. Reichel, F. Yin, Projected nonstationary iterate Tikhonov regularization. BIT Numer. Math. **56**, 467-487 (2016)

[22] S. Gazzola, P. Novati, M. R. Russo, On Krylov projection methods and Tikhonov regularization. Electron. Trans. Numer. Anal. **44**, 83-123 (2015)

[23] R. Tibshirani, Regression shrinkage and selection via the lasso. J. R. Statist. Soc. B. **58**, 267-288 (1996)

[24] H. Zou, T. Hastie, Regularization and variable selection via the elastic net. J. R. Statist. Soc. B. **67**, 301-320 (2005)

[25] S. N. Fricke, J. D. Seymour, M. D. Battistel, D. I. Freedberg, C. D. Eads, M. P. Augustine, Data processing in NMR relaxometry using the matrix pencil. J. Magn. Reson. **313**, 106704 (2020)

[26] Y. Y. Lin, P. Hodgkinson, M. Ernst, A. Pines, A novel detection-estimation scheme for noisy NMR signals: Applications to delayed acquisition data. J. Magn. Reson. **128**, 30-41 (1997)

[27] Y. Hua, T. K. Sarkar, Matrix pencil method for estimating parameters of exponentially damped/undamped sinusoids in noise. IEEE Trans. on Acoust., Speech, and Signal Process. **38**, 814-824 (1990)

[28] K. D. Ikramov, Matrix pencils: Theory, applications, and numerical methods. J. Sov. Math. **64**, 783-853 (1993)

[29] B. P. Epps, E. M. Krivitzky, Singular value decomposition of noisy data, noise filtering. Exp. Fluids. **60**, 126 (2019)

[30] G. W. Stewart, On the early history of the singular value decomposition. SIAM Rev. **35**, 551-566 (1993)

[31] E. Fukushima, S. B. W. Roeder, *Experimental Pulse NMR: A Nuts and Bolts Approach* (Addison-Wesley, Massachusetts, USA, 1981)

[32] S. N. Fricke, Portable, *Low Field Nuclear Magnetic Resonance: Theoretical Foundations and Field Applications* (UC Davis, 2021) (Dissertation)

Chapter 3: Quantitative Stray-Field T_1 Relaxometry with the Matrix Pencil Method

Abstract

The matrix pencil method (MPM) is tested as an approach to quantitatively process multiexponential low-field nuclear magnetic resonance T_1 relaxometry data. The data is obtained by measuring T_1 saturation recovery curves in the highly inhomogeneous magnetic field of a stray-field sensor. 0.9% brine solutions, doped with different concentrations of a Gd^{3+} containing contrast agent, serve as test liquids. Relaxation-times as a function of contrast-agent concentration along with the T_1 relaxation curves for combinations of multiple different test liquids are measured, and the results from processing using MPM as well as inverse Laplace transformation as a benchmark are compared. The relaxation-time resolution limits of both procedures are probed by gradually reducing the difference between the relaxation-times of two liquids measured simultaneously. The sensitivity to quantify the relative contribution of each component to the magnetization build-up curve is explored by changing their volume ratio. Furthermore, the potential to resolve systems with more than two components is tested. For the systems under test, MPM shows superior performance in separating two or three relaxation components, respectively and effectively quantifying the time constants.

3.1 Introduction

Stray-field nuclear magnetic resonance (NMR) relaxometry has evolved into a widely used tool in various industrial applications, such as well-logging and non-destructive materials testing to quantify liquid distributions in porous media and complex system characterization [1–6]. In contrast to conventional NMR systems, where the sample is placed inside the bore of a magnet, single sided or stray-field NMR instruments like the NMR-MOUSE and NMR well-logging tools are constructed from permanent magnets

and surface coils in such a way that the NMR signal is measured from a thin volume outside of the magnet [1]. These systems usually have a field strength below 1 T and a sizeable magnetic field gradient. Due to the gradient, spins at different distances from the magnet surface experience different Larmor frequencies. Hence, an applied radio frequency (RF) pulse will match only the Larmor frequency of spins in a thin sensitive volume at a certain distance away from the magnet surface. The combination of the low magnetic field strength together with the limited size of the sensitive volume results in a low signal to noise ratio (SNR). For the NMR-MOUSE this field of view can be shifted inside the object under study by repositioning the sensor with a step motor, which makes it possible to excite spins at different depths of the object and measure local changes in transverse magnetization decays [1,7].

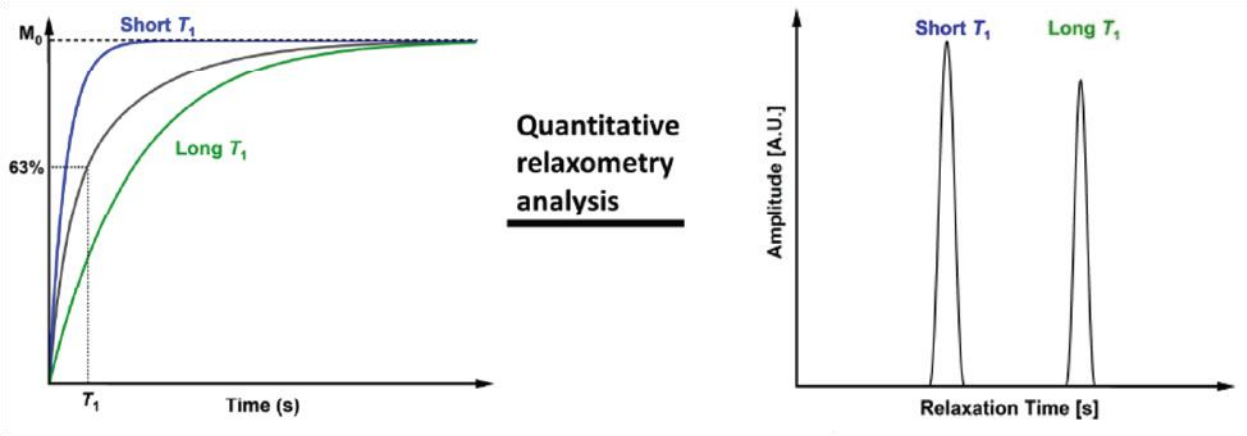

Figure 3.1. *Principle of transforming relaxometry data of a two-component system (left) into a quantitative relaxometry graph (right).*

In this study, the indirectly detected longitudinal magnetization T_1 is quantitatively analyzed in terms of distributions, assuming they are best described by sums of exponential functions. However, the same principles also apply to decays impacted by transverse relaxation T_2 and translational diffusion D [7]. The T_1 relaxation build-up curves on the left-hand side of Fig. 3.1 represent the data of a T_1 relaxation experiment with a long T_1 time (green) and a short T_1 time (blue). The measured signal is a weighted sum of both (black). To obtain a graph that reveals distributions of relaxation-times which resembles a spectrum (Fig. 3.1, right) which reveals the number and relative weight of relaxation components, the measured signal

(black) needs to be adequately decomposed. In the example case of Fig. 3.1, two peaks are obtained in the relaxation-time graph, one with a long and one with a short T_1. The positions of the peak maxima on the x axis gives the relaxation-time and the difference of the peak areas A% reports the nuclear spin ratio of the components.

Various signal processing methods have been applied to relaxation and diffusion signals. One option is to use a multi-exponential fit, but usually prior knowledge about the number and the relaxation-time constants of the relaxation species is needed for this to be successful. Currently, one of the most widely used approaches to quantitatively fit relaxometry/diffusometry data is solving a Fredholm integral of the first kind, often also referred to as an inverse Laplace transformation (ILT) [8–14]. However, the mathematically ill-posed nature of this approach leads to high noise sensitivity and low resolution, disabling the separation of components in close vicinity. These difficulties arise also when fitting model functions to the experimental data to extract the time constants.

In 2020 Fricke et al. [7] applied an approach known as the matrix pencil method (MPM) to the analysis of relaxometry/diffusometry transient signals. This approach is an established analysis tool in various fields such as electromagnetic transient simulations, radar signal processing and vibroacoustic analysis [15–19]. MPM uses a set of matrices to solve generalized eigenvalue problems which yield high resolution, discrete results for the relaxation/diffusion rates and low sensitivity to noise [7]. This approach is similar to covariance NMR, where the data is viewed in a matrix format to allow the application of matrix algebra operations to obtain discrete results for NMR spectra [20–22].

For stray-field NMR to be applicable to an even wider range of industrial and academic questions, such as the depth resolved relaxation analysis of multi-component systems, the ability of fit algorithms to quantitatively resolve close relaxation-time components is crucial. Therefore, the goal of the present work is to test, resolve and quantify the T_1 relaxation-time resolution of MPM in the highly inhomogeneous magnetic field of a stray-field NMR system and compare its performance to ILT and multi exponential fits.

3.2 Theory

3.2.1 Inverse Laplace Transformation

In the one-dimensional case, the NMR signal *s*(t) measured as a function of time *t* is reported in terms of the Laplace transform of a distribution *P(R)* of relaxation rates *R*, where *R* is the relaxation rate or the inverse of the relaxation-time,

$$s(t) = \int_0^\infty P(R)e^{-Rt}dR \tag{3.1}$$

The inverse transformation of Eq. (3.1) provides the distribution of relaxation rates,

$$P(R) = \int_0^\infty s(t)e^{Rt}\mathrm{d}t \tag{3.2}$$

Equation (3.2) is solved numerically with a finite sum of exponential functions. However, since these exponentials do not form an orthogonal set, the solution is not unique, and several different distributions will satisfy this equation. This means that the inversion prescribed by Eq. (3.1) is mathematically ill posed. With an increasing number of relaxation components, the distribution gets broader, resulting in high sensitivity to noise and low resolution. To reduce the number of possible solutions, regularization constraints are imposed. However, these constraints are without physical or statistical meaning and can introduce ambiguities to the interpretation of the relaxation-time distribution graphs. For example, broad peaks can be observed as well as artifacts at the edges of a graph. Detailed discussions of ILT theory and regularization methods are available elsewhere [8–10]. It should be noted that the ILT algorithm in this work employs L2 regularization. Further, the regularization parameter α was determined for each data set individually using a loop to optimize χ^2 [23]. A value of $\alpha = 10^9$ was found to be suitable for all data sets.

3.2.2 Matrix Pencil Method

The MPM introduced by Fricke *et al.* [7] employs an alternative, algebraic approach where the multicomponent relaxation signal is defined as

$$s(t) = \sum_{m=1}^{M} A_m \, e^{-R_m t} \tag{3.3}$$

where R_m are the decay rates of the relaxation components m = 1, 2, ..., M and A_m are corresponding signal amplitudes.

The MPM approach takes advantage of a characteristic exponential function identity. This identity realizes that the scalar

$$z = e^{-R\Delta t} \tag{3.4}$$

written in terms of a single decay rate R and uniform sampling time Δt, is the solution to the vector equation $\boldsymbol{s_1} = z\boldsymbol{s_2}$ when the elements of $\boldsymbol{s_2}$ and $\boldsymbol{s_1}$ are related to the elements of the measured signal array s(n-1) = exp(-(n-1)RΔt) as s_2(n-1) = s(n) and s_1(n-1) = s(n-1) respectively, where n = 1, 2, ..., N indicates the number measured signal array elements. In real, experimentally relevant cases more than just one exponential function contributes to the measured transient signal decay. Here one first separates the measured signal array elements at the time (n-1)Δt, s(n-1), into two matrices $\boldsymbol{Y_1}$ and $\boldsymbol{Y_2}$ as

$$\boldsymbol{Y_1} = \begin{bmatrix} s(1) & s(2) & \cdots & s\left(\frac{N}{2}\right) \\ s(2) & s(3) & & \vdots \\ \vdots & & \ddots & s(N-2) \\ s\left(\frac{N}{2}\right) & \cdots & s(N-2) & s(N-1) \end{bmatrix} \tag{3.5a}$$

and

$$\boldsymbol{Y_2} = \begin{bmatrix} s(2) & s(3) & \cdots & s\left(\frac{N}{2}+1\right) \\ s(3) & s(4) & & \vdots \\ \vdots & & \ddots & s(N-1) \\ s\left(\frac{N}{2}+1\right) & \cdots & s(N-1) & s(N) \end{bmatrix} \tag{3.5b}$$

where N is the total number of measured signal points. These two matrices are used to create the equation for a matrix pencil $\boldsymbol{Y_2} \cdot \boldsymbol{p_m} = z_m \boldsymbol{Y_1} \cdot \vec{p}_m$ that when reorganized reveals the generalized eigenvalue problem

$$\left(\boldsymbol{Y_1}^{-1} \cdot \boldsymbol{Y_2} - z_m \boldsymbol{E}\right) \cdot \vec{p}_m = 0 \tag{3.6}$$

written in terms of the (N – 1)x(N – 1) unit matrix $\boldsymbol{E}$, eigenvector $\vec{p}_m$ and eigenvalue z_m. According to Eq. (3.3), the eigenvalue solutions to this problem z_m directly report on the respective decay rates R_m and thus the associated relaxation time constants T_m since $T_m = 1/R_m$. As shown in detail in Fricke et al. [7], the z_m eigenvalues are used to define left and right Vandermonde matrices $\mathbf{Z_L}$ and $\mathbf{Z_R}$ that, along with the signal matrix $\boldsymbol{Y_2}$, form the matrix triple product $\boldsymbol{A = Z_L \cdot Y_2 \cdot Z_R}$whose diagonal elements A(m,m) are used to identify the relative contributions of each z_m eigenvalue to the total signal. In the case of the purely dissipative, non – oscillatory, exponentially damped transient signals encountered in NMR relaxometry, the z_m eigenvalues with the largest **A**(m,m) amplitude are real. The remainder of the eigenvalues are complex and are neglected as being non-physical and, when noise is present, capture primarily noise. In comparison to relaxometry transient treatment with ILT, the advantages of the MPM approach are higher resolution relaxation time constant estimates with lower computational cost and better stability against noise[7]. The increased resolution of MPM in comparison to ILT is due to the discrete nature of the algebraic approach, which, when signal noise is present produces time constants that are box car distributed [7]. Further details regarding the theory and implementation of the MPM to all classes of one and multidimensional NMR problems can be found in the literature [7,24–27].

3.3 Method

In this work, experiments are conducted with an NMR-MOUSE PM25 stray-field sensor connected to a Kea2 spectrometer manufactured by Magritek (Aachen, Germany). The stray-field is highly inhomogeneous and exhibits a strong constant field gradient of 300 kHz/mm in direction perpendicular to the flat sensitive slice. The lateral extension of the sensitive slice is 40 mm x 40 mm, and the ^{1}H Larmor frequency at that position is 13.8 MHz. For the measurements, the thickness of the sensitive slice is set to 0.4 mm, which corresponds to an acquisition time of 8 µs at the center of each echo. The pulse length was set to 5.75 µs.

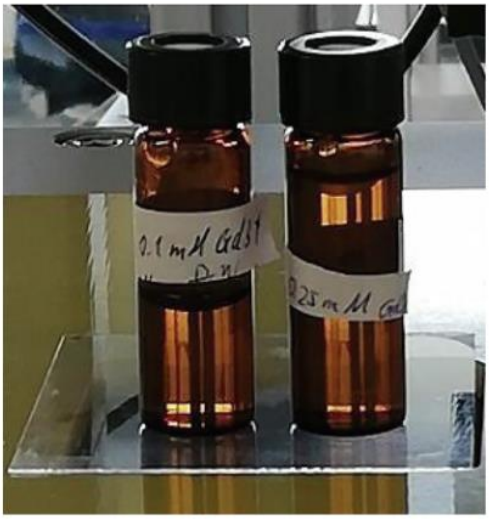

Figure 3.2. *Experimental setup with two different test liquids placed together on the detector.*

The model systems to test the resolution of the MPM are 0.9 weight-percent sodium chloride solutions doped with different amounts of diethylenetriaminepentaacetic acid gadolinium(III) dihydrogen salt hydrate (Gd-DTPA) (381667 Sigma-Aldrich) as a contrast agent. Sodium chloride solution was chosen as this is a standard test fluid used in several important industrial applications, e.g. hygiene product testing [4]. To prepare the test liquids, first a stock solution of 0.9% brine with a 2 mM concentration of the contrast agent was made. Afterwards, the stock solution was diluted to the desired concentrations to achieve a variety of relaxation-times. The samples at different dilutions were stored in separate identical glass vials (Fig. 3.2) with an outer diameter of 14.9 mm and an inner diameter of 12.3 mm. As the cross section of the vials is small compared to the detection area of the PM25 relaxometer, up to four of these tubes can be placed on the detector simultaneously. With this setup, measurements of various combinations of multiple relaxation species were possible. Measurements of the different solutions were conducted individually as well as in different combinations of two or three components. The T_1 relaxation data for comparing MPM and ILT were generated with a saturation recovery sequence as shown in Fig. 3.3.

The expression for this sequence takes the form of Eq. 3.7

$$s(t) = s_\infty(1 - e^{-R_m t}) \tag{3.7}$$

The approach outlined in the theory section for the MPM can be applied directly to data of this form without the need for an inversion. However, in this case the "1" in Eq. (3.7) will lead to an additional, real, and positive eigenvalue. This eigenvalue corresponds to a very long relaxation time which functions similar to a DC offset. The amplitude of this offset has the opposite sign of the physical eigenvalues which makes it easily recognizable. This offset is then discarded with no negative effects to the physical results.

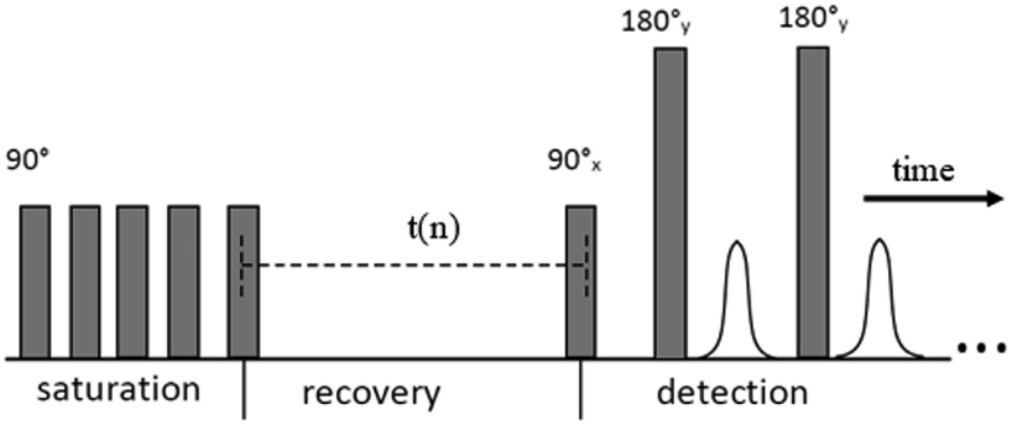

Figure 3.3. *Saturation recovery sequence.*

The recovery period t(n) for the magnetization build-up was linearly divided into N = 500 steps, which is directly used as input parameter to create the (N-1)x(N-1) $\boldsymbol{Y_1}$ and $\boldsymbol{Y_2}$ matrices shown in equation 3.5. 16 scans were averaged at each step as the SNR is proportional to the square root of the number of averaged scans [28]. The signal was detected by averaging the first 8 echoes of a CPMG sequence at an echo time of 100 μs. With this the proton density can be probed without the impacts of diffusion or relaxation on the signal [1]. These parameters were chosen to have a reasonable SNR while not overextending the measurement time. To access background noise, a measurement without sample was recorded. Based on this, the core noise level was determined to be one standard deviation on either side of the noise trace, as the majority of the noise is inside of these boundaries.

The SNR was calculated by dividing the signal at thermodynamic equilibrium by the noise level. A linear correlation with the number of vials on top of the detector was found. Ratios of around 48, 72, and 96 were determined for two, three, and four vials, respectively.

To evaluate the relaxation-time resolution limit of ILT and MPM, the relative difference $\Delta T_{\%}$ between two relaxation constants T_i is defined,

$$\Delta T_{\%} = (T_{\mathrm{A}} - T_{\mathrm{B}}) * 100\%/T_{\mathrm{A}} \tag{3.8}$$

where T_{A} is the relaxation-time of the long component and T_{B} the relaxation-time of the short component.

3.4 Results and Discussion

To determine the "true value" as reference for the computational accuracy, the T_1 relaxation-time of each relaxation species was measured as reported in Table 3.1. The reported error values correspond to 90% confidence intervals obtained by measurements of five different samples with the same concentration. With the chosen contrast-agent concentrations the T_1 values covered one order of magnitude, from about 90 ms to 1100 ms. In addition, a 0.9% brine solution without contrast-agent was tested. The solutions show the expected linear increase in relaxation rates $R_1 = 1/T_1$, with increasing contrast agent concentration [29]. Table 3.1 also reports the relative difference $\Delta T_{\%} = \Delta T_n/T_{1,\mathrm{stock}}$ of the relaxation-times with respect to the stock solution.

Next, the saturation-recovery curves for two equal proton concentration containers simultaneously placed on the detector, were obtained. Three indicators are used to evaluate the relaxation-time resolution limit:

1. The potential to resolve both relaxation components.
2. The agreement of the T_1 relaxation-time constants determined via the single component measurements with those determined from the distribution of the peaks.
3. The magnitude of the quantification error of the relative contribution of the two components. The expected ratio is one as the spin density in all samples is the same within ± 1.1%.

Table 3.1: *T_1 relaxation-time constants and rates for the different contrast-agent concentrations.*

Solution	Gd-DTPA concentration [mM]	T_1 (true value) [ms]	R_1 [1/s]	$\Delta T_{\%}$ [%]
A	2	89 ± 15	11.2 ± 1.90	n/a
B	1.5	133 ± 21	7.5 ± 1.28	33.1
C	1	179 ± 30	5.59 ± 0.95	50.3
D	0.5	338 ± 58	2.96 ± 0.52	73.7
E	0.25	595 ± 95	1.68 ± 0.27	85.0
F	0.1	1099 ± 197	0.91 ± 0.16	91.9
G	0	2240 ± 370	0.45 ± 0.08	96.0

3.4.1 Relaxation Time Resolution Limit

To determine the relaxation-time resolution limit, measurements were performed where solution A is placed on the detector together with a second tube having a different contrast agent concentration and thus different T_1 value. Figure 3.4 summarizes the resulting graphs for the different relaxation species combinations, calculated with ILT (dashed) and MPM (solid). Black brackets at the top of the graphs are used to indicate the true value range of relaxation-time values based on the average relaxation-times and 90% confidence intervals of the individual components outlined in Table 3.1.

It should be noted that the $A_{\%}$ values shown for the ILT peaks report the relative area under the apparent peaks on the logarithmic scale. The areas of artifacts were excluded from the analysis. The bins on the *x* axis are equidistant on a logarithmic scale, therefore, to get the area under the peak the left sided Riemann sum of the incremental areas is taken. Furthermore, the reported T_1 time constants for ILT

correspond to the positions of the peak maxima. The reported $A_{\%}$ values for MPM correspond to the intensities of the peaks and not the areas under the curve, as explained in the theory section.

For the first combination, solutions A and G were measured together. Figure 3.a shows that at a high $\Delta T_{\%}$ of 96.4%, both algorithms are able to resolve the components. The $A_{\%}$ values rounded to full percentages are 50:50 for MPM, and the computed T_1 relaxation-times are within the range of one standard deviation below and above the average values measured for these relaxation components individually (see Table 3.1). With ILT the longer component is in the expected range, while the shorter component is overestimated by 39% and even the distribution is outside the true T_1 time-constant range. The quantification leads to an inaccurate ratio of 38:62. In addition, at the left edge of the ILT graph a third peak emerges which is one of the artifacts mentioned in the theory section. This can be verified by extending the limits of the x axis, when performing the calculation. Instead of resulting in a larger fraction of the entire area, the signal is still present at the edge of the graph (data not shown). The false prediction of the short component, even though the relative difference between the relaxation time is high, is possibly related to the occurrence of the artifact.

In the case that the 0.9% brine solution is substituted with solution F (Figure 3.4b), $\Delta T_{\%} = 91\%$. For this combination no artifact appears in the ILT graph, and the results are in agreement with the expected longitudinal relaxation-time values for both peaks and the ratio of 49:51 indicates close to equal contributions to the overall signal. MPM produces similar results.

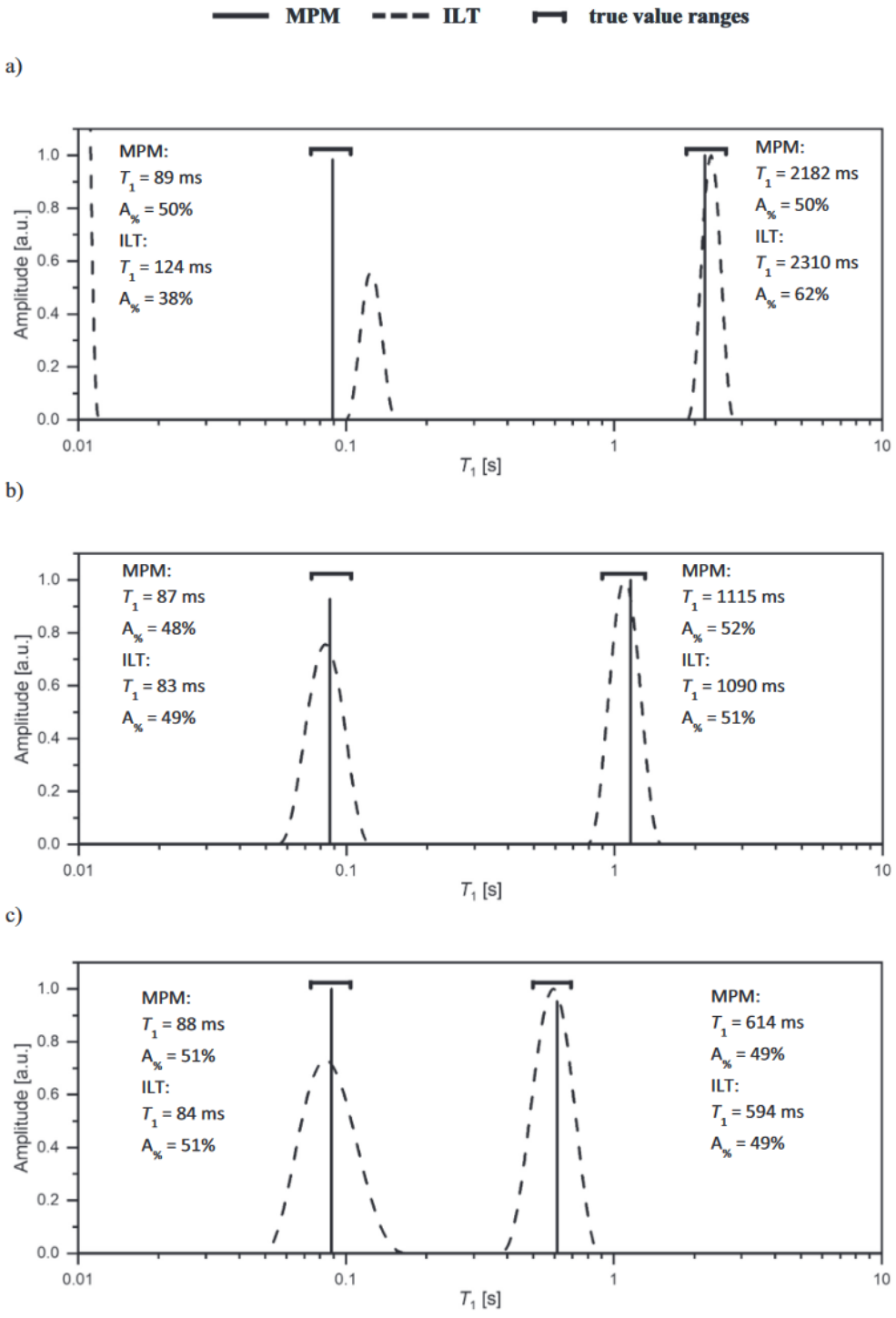

Figure 3.4. *Comparison of quantitative relaxometry results obtained using ILT (dashed line) and MPM (solid line) for different combinations of relaxation-time components. In graphs a-f) results are shown for the combination of solution A with G, F, E, D, C and B. The range of the true T_1 values determined for each component individually are given as black brackets at top of the graphs.*

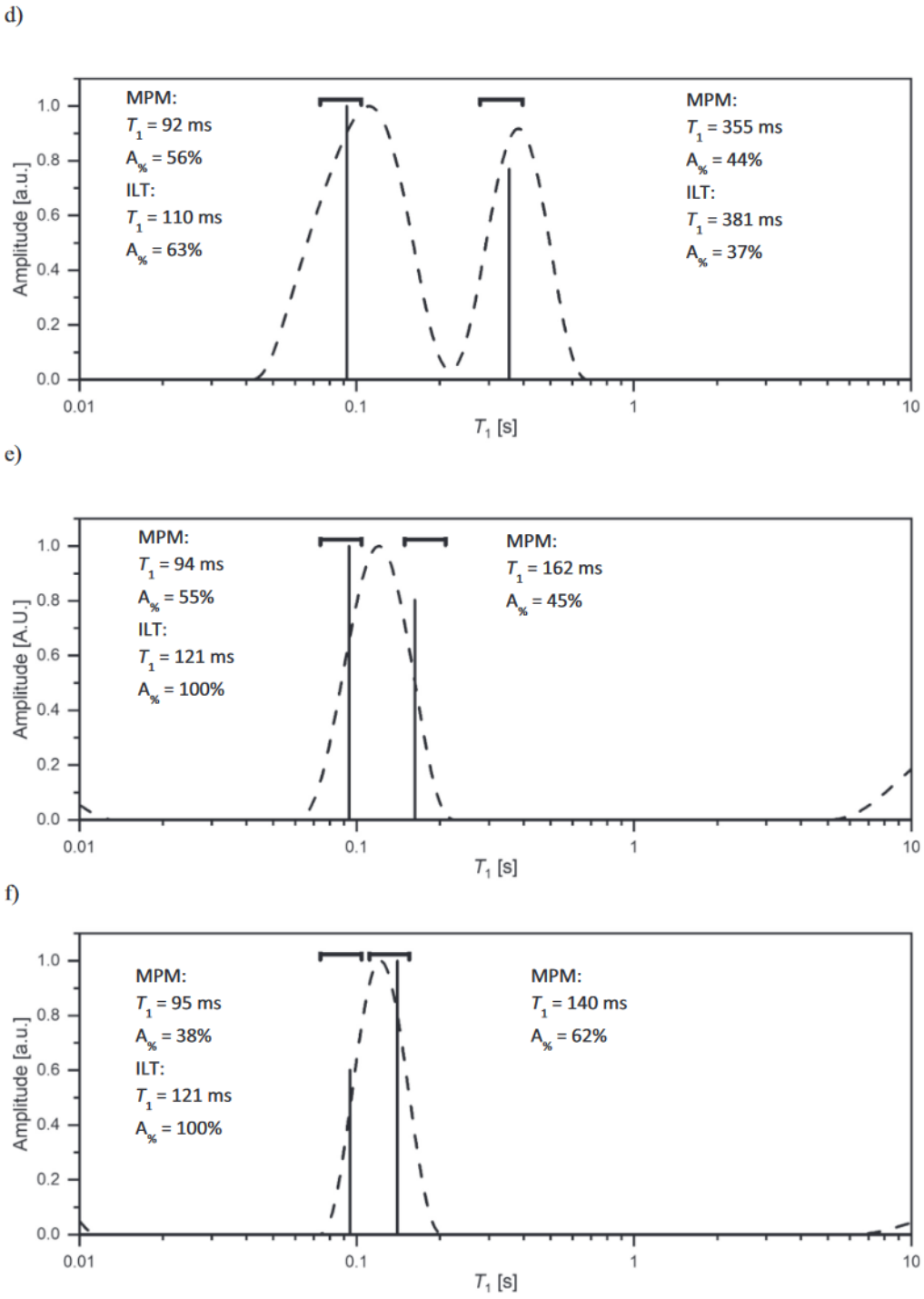

Figure 3.4 (cont.). *Comparison of quantitative relaxometry results obtained using ILT (dashed line) and MPM (solid line) for different combinations of relaxation-time components. In graphs a-f) results are shown for the combination of solution A with G, F, E, D, C and B. The range of the true T_1 values determined for each component individually are given as black brackets at top of the graphs.*

When using solution E as the second component (Figure 3.4c), $\Delta T_{\%}$ is reduced to 85%. The two T_1 relaxation components can still be resolved with both algorithms and the quantification results in $A_{\%}$ values of 51% for the short component and 49% for the long component. The T_1 time constants are in the measured ranges for the single components. The peak of the short component shows a broad distribution in the ILT graph.

For solutions A and D where $\Delta T_{\%}$ = 73.7%, the ILT starts to approach its resolution limit. The peaks are no longer completely separated (Figure 3.4d). The true T_1 value ranges are within the distributions of the two peaks. The maximum of the peak is shifted towards higher relaxation-times for the short component. The quantification leads to $A_{\%}$ values of 63% and 37% which is as well outside of the range acceptable for analytical quantification. MPM, on the other hand, separates the two components effectively and also performs better at determining the contribution to the overall signal with a ratio of 56:44. The T_1 relaxation-time constants of the two peaks match the expected relaxation-time ranges.

In the case where solutions A and C are placed on the detector together, $\Delta T_{\%}$ = 50.3%. Here, the ILT is no longer able to resolve the two components and the graph in Figure 3.4e shows only one peak with a T_1 relaxation-time that is about the average of the constants of the two components. This indicates that for the ILT algorithm used here, two relaxation-times need to have a relative difference of about 74% to be resolved and accurately quantified. MPM, on the other hand, is able to resolve the two relaxation species even at a relative difference of about 50%. Furthermore, the relaxation constants match the ones measured for each component individually and the $A_{\%}$ have an acceptable ratio of 55:45.

Finally, the lowest tested relative difference of 33.1% was achieved by combining solutions A and B for the T_1 saturation recovery experiment (Figure 3.4f). In this case also the MPM reaches its relaxation-time resolution limit. While the estimation of the relaxation-time constants leads to the values that are in agreement with the results of the single component measurements, the quantification fails as the amplitudes have a ratio of 38:62, which is not within an acceptable range.

Based on these observations, the T_1 relaxation-time resolution limit of the MPM is determined to be between 33.1% and 50.3% as the latter was the last combination where the two peaks are properly

resolved and the quantification as well as the estimation of the T_1 time constants are successful. With ILT a $\Delta T_{\%} \approx 74\%$ was required to resolve the two relaxation components. Due to the discrete nature of the eigenvalues calculated via MPM a higher relaxation-time resolution can be achieved compared to ILT.

3.4.2 MPM Relaxation Time Resolution Limit Verification

As the next step it was tested whether the determined relaxation-time resolution limit of MPM is impacted by the magnitude of the relaxation-time. Therefore, combinations of relaxation species with a similar relative difference, but higher absolute T_1 relaxation-time constants were tested. The different combinations have $\Delta T_{\%}$ values between 43.2 and 50.3%. Table 2 summarizes the investigated solution combinations with their respective relative differences as well as the determined T_1 values and the relative contributions of the component.

Fig. 3.5 shows the corresponding relaxation graphs. Peaks with the same colour correspond to the same solution combination. Black brackets at the top of the graphs are used to indicate the expected range of relaxation-time values based on the average relaxation-times and standard deviations of the individual components outlined in Table 3.1. For all cases it was possible to effectively resolve the two components. All estimated T_1 time constants are in agreement with the expected values obtained from measuring the relaxation-times of the components individually. From the $A_{\%}$ in Table 3.2 it can be seen that the ratio of the components is around 50:50 for all combinations.

Table 3.2. *MPM quantitative T1 relaxometry analysis results for combinations with relative differences close to the relaxation-time resolution limit.*

Solution combination	**$\Delta T_{\%}$ [%]**	**Component 1 T_1 [ms]**	**Component 2 T_1 [ms]**	**Component 1 $A_{\%}$ [%]**	**Component 2 $A_{\%}$ [%]**
2 mM and 1 mM Gd-DTPA (A and C)	50.3	94	162	55	45
1 mM and 0.5 mM Gd-DTPA (C and D)	47.0	184	309	55	45
0.5 mM and 0.25 mM Gd-DTPA (D and E)	43.2	326	601	53	47
0.25 mM and 0.1 mM Gd-DTPA (E and F)	45.9	579	1089	48	52

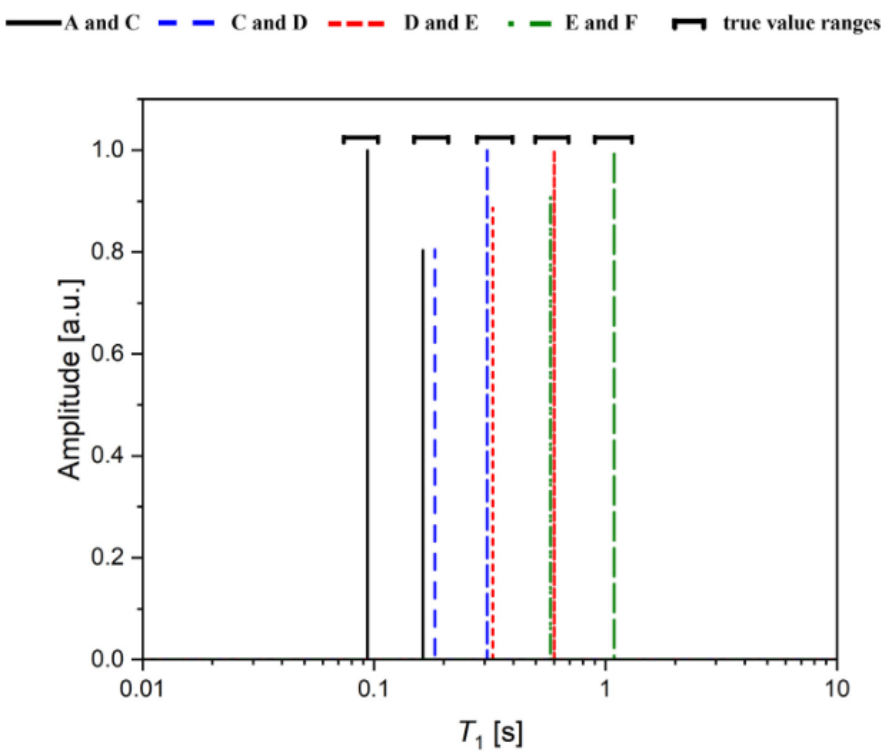

Figure 3.5. *MPM T_1 relaxometry results for combination with relative differences close to the relaxation-time resolution limit. The range of the true T_1 values determine for each component individually are given as black brackets at top of the graphs.*

3.4.3 Quantification Sensitivity

Next to determining the relaxation-time resolution limit, the sensitivity of MPM to quantify components in a mixture was tested and compared to the ILT method. For this, in addition to the 50:50 combination already used in section 3.4.1 solutions A and D were placed on the detector together with ratios of 66:33 and 75:25. Fig 3.6A shows the resulting graphs for the different ratios obtained using ILT, while Fig. 3.6B shows the results determined using MPM. Black brackets at the top of the graphs are used to indicate the range of the true T_1 time values for the two components.

When processing the data using ILT the position of the peak maxima of the 50:50 combination of solutions A and D are slightly overestimated for the shorter component, but the distributions still overlap with the expected range. The maxima of both components are inside the expected range for the 66:33 and

75:25 ratios. The differences in the contribution could lead to narrower peaks and might improve the potential to resolve the two components.

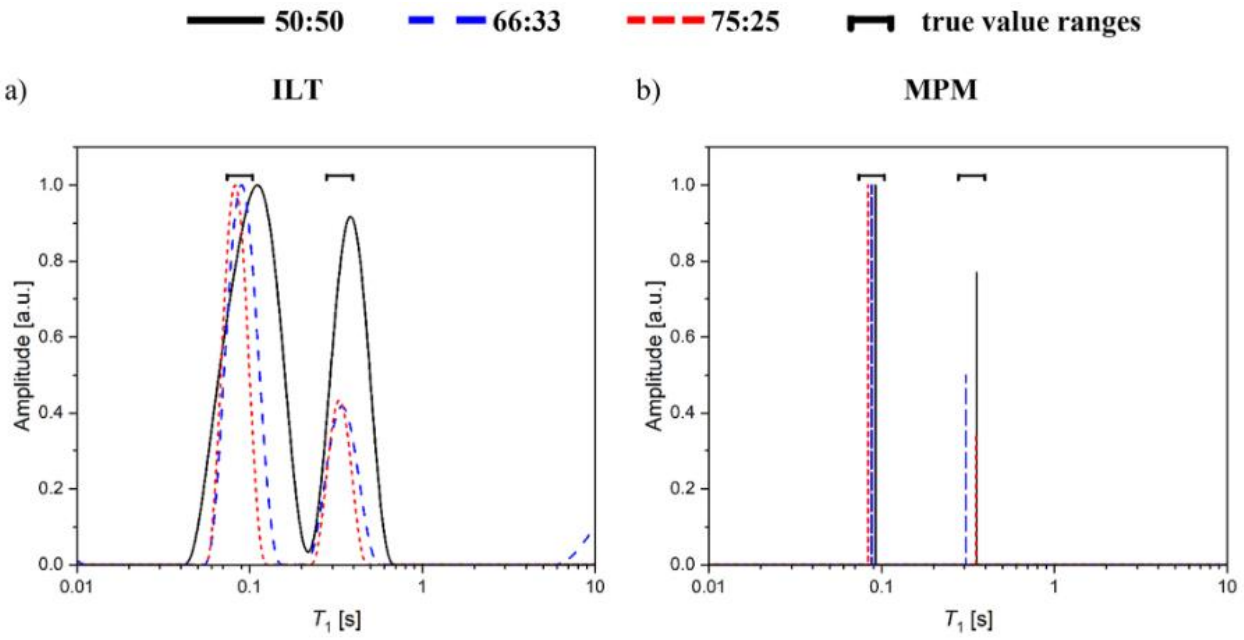

Figure 3.6. *T_1 relaxation graphs of two component systems with ratios of 50:50 (black straight line), 66:33 (blue dashed line) and 75:25 (red short-dashed line). The range of the true T_1 values determined for each component individually are given as black brackets at the top of the graphs. The results were computed with a) ILT, using $\alpha = 10^9$ and b) MPM.*

On the other hand, the T_1 relaxation-time constant calculated via MPM are determined, well within the error range for all ratios. To quantify the contribution of the individual components using ILT the areas under the peaks of the resulting graphs are integrated, while for MPM the peak intensities are compared. Table 3.3 summarizes the quantification results based on the two different approaches. With ILT the analysis of the magnetization build-up curve data for the 50:50 ratio leads to an erroneous quantification, as the relative difference of the two components is too low. For the other two data sets, the integrations yield ratios of 71:29, which is in both cases close to the expected contribution to the original magnetization build-up signal. However, it is not possible to differentiate the two combinations.

Table 3.3. *Quantification results of a two-component system obtained by ILT and MPM for different component ratios.*

Expected ratio	ILT	MPM
50:50	63:37	56:44
67:33	71:29	67:33
75:25	71:29	74:26

The T_1 relaxation-times calculated via MPM all match the expected ranges of solutions A and D. Further, the peak intensities are in good agreement with the expected ratios for all tested ratios. These results imply that MPM is more reliable at quantifying components with varying contributions to the overall signal than ILT.

3.4.4 Multicomponent Measurements

In the final experiment, the complexity of the system under test was extended to a three-component system to test whether MPM is also capable of resolving and quantifying systems with more than two components. For this study solutions A, F and G were placed on the detector together in equal quantities, leading to an expected relative contribution of 33% for each component.

Figure 3.7 shows the resulting NMR relaxometry graphs obtained using MPM (solid) and ILT (dashed). Black brackets at the top of the graphs are used to indicate the expected relaxation-time ranges for the three components. Both algorithms were able to estimate the correct number of relaxation components. However, the positions of the peaks calculated via ILT do not match the expected values. The T_1 relaxation-time of solution A, the shortest component, is overestimated by a factor of about 2.5, the maximum of the relaxation-time distribution of the medium component (solution F) is a factor of 2 lower than the expected values. Only the peak of the 0.9% brine solution without contrast agent is partly

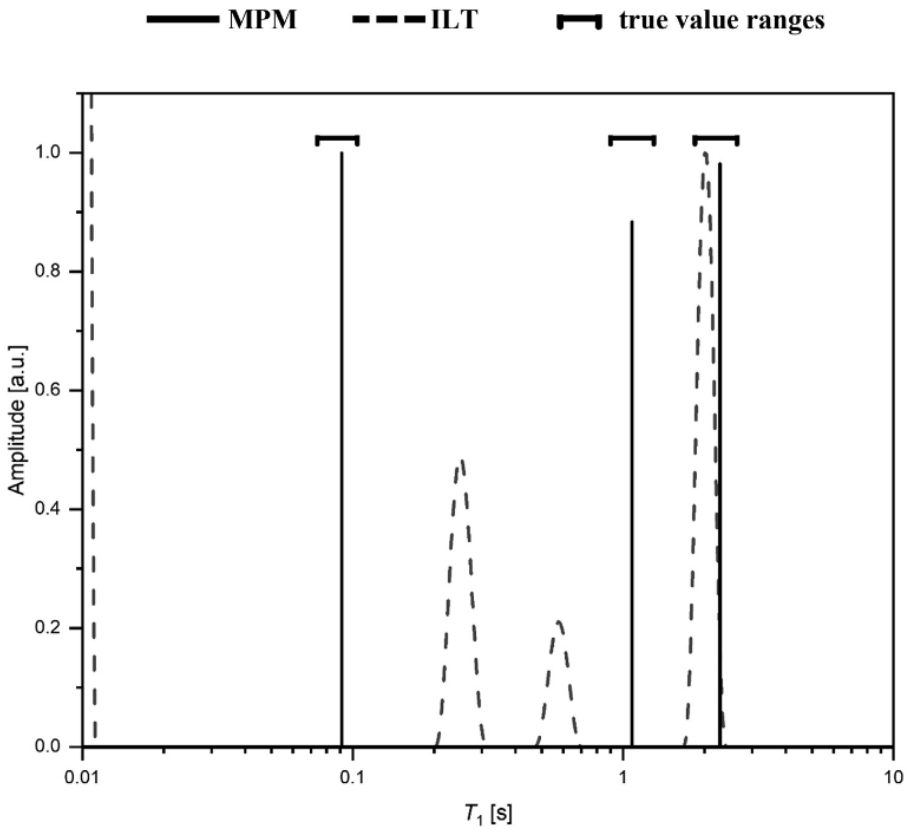

Figure 3.7. *T_1 NMR relaxometry graph of a combination of three components. MPM results are shown as solid, ILT results as dashed lines. The range of the true T_1 values determined for each component individually are given as black brackets at top of the graphs.*

in the expected range. Further, integrating the area under the peaks leads to a ratio of 33:13:54, for solutions A, F and G, respectively.

On the other hand, all relaxation-times were estimated correctly using MPM. The quantification results were accurate with calculated relative contributions of 35% (solution A), 31% (solution F) and 34% (solution G). This shows MPM is more accurate to determine and quantify relaxation-times for multicomponent systems.

3.5 Conclusion

The performance of the MPM algorithm for quantitative relaxometry analyses is tested in this experimental study. The MPM results are compared with the widely applied L2 regularized, ILT method on T_1 data obtained in the highly inhomogeneous magnetic field of a stray-field relaxometer. Using MPM it is possible to effectively resolve two relaxation species that have a relative difference $\Delta T_{\%} \approx 43\%$, while for the same data the tested ILT algorithm is limited to resolve two components with $\Delta T_{\%} > 73\%$. With MPM it was even possible to separate a pair of relaxation species with a relative difference of 33.1%.

The resolution limit for MPM is verified by combining samples with overall higher relaxation-times, but similar relative difference in the range of 40 – 50%. This shows that the relaxation-time resolution limit is not negatively impacted by the magnitude of the relaxation-time.

The two-component quantification sensitivity of both MPM and the ILT was also tested. It is possible to reliably quantify ratios of 50:50, 67:33 and 75:25 using MPM with $A_{\%}$ close to the expected relations. The sensitivity of the applied ILT algorithm is too low to differentiate between a 67:33 and 75:25 ratio.

For the system under test, both algorithms could successfully reduce the measured magnetization build-up curve to three different relaxation components. However, the ILT algorithm failed to determine the correct relaxation-times for all solutions and only the quantification of the short component matched the expected 33% contribution. It should be noted that there is a variety of ways to impose constraints and regularizations on ILT that will impact the resulting distributions and could lead to improved resolution as well as sensitivity.

This experimental study shows, that MPM is a robust approach to reveal and quantify components in mixtures of relaxation species with discrete T_1 relaxation-time constants. This holds true even for data with SNR lower than 100 measured in the highly inhomogeneous magnetic field of a stray-field NMR sensor.

Future work will be dedicated to advancing the MPM algorithm to reveal distributions of relaxation times and diffusion coefficients as well as to process 2-dimensional, data. In addition, further investigations will be performed on fluids interacting with porous media and the acquisition of depth resolved relaxation/diffusion profiles. It will also be determined if the high resolution offered by MPM permits the tracking of small, long term T_1, T_2 and D changes during aging. This will allow the stability of complex formulations to be reliably monitored in real time. It is clear that MPM could allow the analysis of currently inaccessible systems in several industrial sectors via low-field NMR sensors.

References

[1] J. Perlo, F. Casanova, B. Blümich, Profiles with microscopic resolution by single-sided NMR, J. Magn. Reson. 176 (2005) 64–70. https://doi.org/10.1016/j.jmr.2005.05.017.

[2] B. Blümich, J. Perlo, F. Casanova, Mobile single sided NMR, Progess Nucl. Magn. Reson. Spectrosc. 52 (2008) 197–269. https://doi.org/10.1016/j.pnmrs.2007.10.002.

[3] V. Anand, Novel methodology for accurate resolution of fluid signatures from multi-dimensional NMR well-logging measurements, J. Magn. Reson. 276 (2017) 60–68. https://doi.org/10.1016/j.jmr.2017.01.007.

[4] B. Mohebbi, J. Claussen, B. Blümich, Fast and robust quantification of liquid inside thin fibrous porous materials with single-sided NMR, Magn. Reson. Imaging. 56 (2019) 131–137. https://doi.org/10.1016/j.mri.2018.09.022.

[5] R. de Oliveira-Silva, É. Lucas-Oliveira, A.G. de Araújo-Ferreira, W.A. Trevizan, E.L.G. Vidoto, D. Sakellariou, T.J. Bonagamba, A benchtop single-sided magnet with NMR well-logging tool specifications – Examples of application, J. Magn. Reson. 322 (2021) 106871. https://doi.org/10.1016/j.jmr.2020.106871.

[6] A.H. Tavangarrad, Continuum-scale modeling of water infiltration into a stack of two thin fibrous layers and their inter-layer space, Chem. Eng. Sci. 207 (2019) 769–779. https://doi.org/10.1016/j.ces.2019.07.001.

[7] S.N. Fricke, J.D. Seymour, M.D. Battistle, I.D. Freedberg, C.D. Eads, M.P. Augustine, Data processing in NMR relaxometry using the matrix pencil, J. Magn. Reson. 313 (2020) 106704. https://doi.org/10.1016/j.jmr.2020.106704.

[8] L. Venkataramanan, Y.-Q. Song, M.D. Hurlimann, Solving Fredholm integrals of the first kind with tensor product structure in 2 and 2.5 dimensions, IEEE Trans. SIGNAL Process. 50 (2002) 1017–1026. https://doi.org/10.1109/78.995059.

[9] E.J. Fordham, L. Venkataramanan, J. Mitchell, A. Valori, What are, and what are not, Inverse Laplace Transforms, Diffus. Fundam. 29 (2017) 1–8. https://nbn-resolving.org/urn:nbn:de:bsz:15-qucosa2-315904.

[10] Y.-Q. Song, Resolution and uncertainty of Laplace inversion spectrum, Magn. Reson. Imaging. 25 (2007) 445–448. https://doi.org/doi:10.1016/j.mri.2006.11.023.

[11] V.-V. Telkki, Hyperpolarized Laplace NMR, Magn Reson Chem. 56 (2018) 619–632. https://doi.org/10.1002/mrc.4722.

[12] V.-V. Telkki, M. Urbańczyk, V. Zhivonitko, Ultrafast methods for relaxation and diffusion, Prog. Nucl. Magn. Reson. Spectrosc. 126–127 (2021) 101–120. https://doi.org/10.1016/j.pnmrs.2021.07.001.

[13] R. Bai, C. Guan Koay, E. Hutchinson, P.J. Basser, A framework for accurate determination of the T2 distribution from multiple echo magnitude MRI images, J. Magn. Reson. 244 (2014) 53–63. https://doi.org/10.1016/j.jmr.2014.04.016.

[14] J. Martin, A. Reymbaut, M. Schmidt, A. Doerfler, M. Uder, F.B. Laun, D. Topgaard, Nonparametric D-R1-R2 distribution MRI of the living human brain, NeuroImage. 245 (2021) 118753. https://doi.org/10.1016/j.neuroimage.2021.118753.

[15] B. Salarieh, H.M.J. De Silva, Review and comparison of frequency-domain curve-fitting techniques: Vector fitting, frequency-partitioning fitting, matrix pencil method and loewner matrix, Electr. Power Syst. Res. 196 (2021) 107254. https://doi.org/10.1016/j.epsr.2021.107254.

[16] M. Mazzotti, I. Bartoli, G. Castellazzi, A. Marzani, Computation of leaky guided waves dispersion spectrum using vibroacoustic analyses and the Matrix Pencil Method: A validation study for immersed rectangular waveguides, Ultrasonics. 54 (2014) 1895–1898. https://doi.org/10.1016/j.ultras.2014.05.009.

[17] Y.Q. Zou, X.Z. Gao, X. Li, Y.X. Liu, A Matrix Pencil Algorithm Based Multiband Iterative Fusion Imaging Method, Sci. Rep. 6 (2016) 19440. https://doi.org/10.1038/srep19440.

[18] B. Fourestie, Z. Altman, J. Wiart, A. Azoulay, Correlate measurements at different test sites, IEEE Trans. ANTENNAS Propag. 47 (1999) 1569–1573. https://doi.org/10.1109/8.805901.

[19] S. Wang, Z.C. Wu, L. Du, G.H. Wei, Y.Z. Cui, Study on the Matrix Pencil Method with Application to Predict Time-domain Response of a Reverberation Chamber, Appl. Comput. Electromagn. Soc. J. 28 (2013) 763–771.

[20] D.A. Snyder, Covariance NMR: Theoretical concerns, practical considerations, contemporary applications and related techniques, Prog. Nucl. Magn. Reson. Spectrosc. 122 (2021) 1–10. https://doi.org/10.1016/j.pnmrs.2020.09.001.

[21] K. Takeda, Y. Kobayashi, Y. Noda, K. Takegoshi, Inner-product NMR spectroscopy: A variant of covariance NMR spectroscopy, J. Magn. Reson. 27 (2018) 146–151. https://doi.org/10.1016/j.jmr.2018.10.012.

[22] A. Fredi, P. Nolis, C. Cobas, T. Parella, Access to experimentally infeasible spectra by pure-shift NMR covariance, J. Magn. Reson. 270 (2016) 161–168. https://doi.org/10.1016/j.jmr.2016.07.010.

[23] K.P. Whittall, A.L. MacKay, Quantitative interpretation of NMR relaxation data, J. Magn. Reson. 1969. 84 (1989) 134–152. https://doi.org/10.1016/0022-2364(89)90011-5.

[24] Y. Hua, T.K. Sarkar, Matrix pencil method for estimating parameters of exponentially damped/undamped sinusoids in noise, IEEE Trans Acoust Speech Signal Process. 38 (1990) 814–824. https://doi.org/10.1109/29.56027.

[25] Y.-Y. Lin, P. Hodgkinson, M. Ernst, A. Pines, A Novel Detection-Estimation Scheme for Noisy NMR Signals: Applications to Delayed Acquisition Data, J. Magn. Reson. 128 (1997) 30–41. https://doi.org/1090-7807/97.

[26] T.K. Sarkar, O. Pereira, Using the Matrix Pencil Method to Estimate the Parameters of a Sum of Complex Exponentials, IEEE Antennas Propag. Mag. 37 (1995) 48–55. https://doi.org/10.1109/74.370583.

[27] Kh.D. Ikramov, Matrix pencils: Theory, applications, and numerical methods, J. Sov. Math. 64 (1993) 783–853. https://doi.org/10.1007/BF01098963.

[28] G. Helms, P. Dechent, Increased SNR and reduced distortions by averaging multiple gradient echo signals in 3D FLASH imaging of the human brain at 3T, J. Magentic Reson. Imaging. 29 (2009) 198–204. https://doi.org/10.1002/jmri.21629.

[29] C.E. Anderson, S.B. Donnola, Y. Jiang, J. Batesole, R. Darrah, M.L. Drumm, S.M. Brady-Kalnay, N.F. Steinmetz, X. Yu, M.A. Griswold, C.A. Flask, Dual Contrast - Magnetic Resonance Fingerprinting (DC-MRF): A Platform for Simultaneous Quantification of Multiple MRI Contrast Agents, Sci. Rep. (2017) 1–10. https://doi.org/10.1038/s41598-017-08762-9.

Chapter 4: Improving the Resolution of MPM Recovered Relaxometry Parameters with Proper Time Domain Sampling

Abstract

The matrix pencil method (MPM) is a powerful tool for processing transient nuclear magnetic resonance (NMR) relaxation signals with promising applications to increasingly complex problems. In the absence of signal noise, the eigenvalues recovered from an MPM treatment of transient relaxometry data reduce to relaxation coefficients that can be used to calculate relaxation time constants for known sampling time Δt. The MPM eigenvalue and relaxation coefficient equality as well as the resolution of similar eigenvalues and thus relaxation coefficients degrade in the presence of signal noise. The relaxation coefficient Δt dependence suggests one way to improve MPM resolution by choosing Δt values such that the differences between all the relaxation coefficient values are maximized. This work develops mathematical machinery to estimate the best Δt value for sampling damped, transient relaxation signals such that MPM data analysis recovers a maximum number of time constants and amplitudes given inherent signal noise. Analytical and numerical reduced dimension MPM is explained and used to compare computer-generated data with and without added noise as well as treat real measured signals. Finally, the understanding gleaned from this effort is used to predict the best data sampling time to use for non-discrete, distributions of relaxation variables.

4.1 Introduction

Nuclear magnetic resonance (NMR) spectroscopy has a rich history in the study of solid, liquid, and gas phase samples in chemistry, biology, physics, medicine, etc [1]. High-resolution NMR, typically performed at high magnetic field with superconducting magnets using chemical shifts, scalar J couplings [2, 3], and long-range dipolar couplings spectrally manifesting as sample-ordered line-splitting or relaxation-induced line broadening [4–6], has emerged as the premiere method to study three-dimensional

chemical structure in solid and liquid phases. Lower magnetic field bench top, permanent magnets are beginning to become more popular in these high-resolution studies [7] although they have been used for years in magnetic resonance imaging and relaxometry [8, 9]. The imaging of materials [10] and living objects [11] is an entirely separate active research area that provides critical information regarding the preparation of new devices with engineered properties and of course, in the case of humans, insight into health and illness. NMR relaxometry, often performed on protonated samples with Larmor frequencies in the 1–20 MHz range, commonly uses low-resolution permanent magnets [8, 9]. Here the spectral resolution is poor, chemical shifts and scalar J couplings are not resolved, and typically the spin–lattice, longitudinal and spin–spin, transverse relaxation times, and the macroscopic diffusion coefficient as well as their respective two-dimensional correlations are the core measured parameters. The application of these low-field relaxometry measurements to complex mixtures often reveals several relaxation times, and, therefore, a unique signal that is described by a weighted sum of exponentials [12, 13]. Provided these parameters can be measured, and more importantly extracted from the time domain, transient signals, they can be used as a fingerprint for a given substance or mixture, much like the chemical shifts and J couplings form fingerprints for complex macromolecules in high-resolution NMR work [7].

The Fourier transform (FT) used to extract frequencies and amplitudes from oscillatory high-resolution time domain NMR-free induction signals is not capable of recovering relaxation time values from exponentially damped, non-oscillatory NMR relaxometry signals. As relaxometry signals are not complex and oscillatory, the FT produces a spectrum with one broad peak at zero frequency. In these situations, the inverse Laplace transform (ILT) has emerged as the current industry standard for recovering relaxation time values from multicomponent NMR relaxometry data [13]. The ILT takes exponentially damped, real, and non-oscillatory transient signals as input and provides distributions of relaxation rates or times as output. Discretization of the ILT for application to data is accomplished by routines such as the Lawson–Hanson algorithm [14], a non-negative least squares (NNLS) method. As is common for inversion problems, ILT is an inherently ill-posed problem when unmodified. The consequences of this ill-posed nature are that several solutions may satisfy the problem, and that these solutions are easily influenced by

minute differences in the data. Using a set of pure exponential decay functions to model a data set that is a mixture of noise with pure exponential decay functions results in severe ILT instability. To restrict the number of possible solutions, L2 regularization is often applied at the expense of increased computation time and of course added artificial output distribution broadening [15].

In recent years, some alternative methods have found success in bypassing some of the stability complications of the L2 regularized NNLS algorithms. One such method is Modified Total Generalized Variation regularization which conjoins L1 and L2 regularizations allowing variability in the discernment of discrete and continuous distribution features [16]. Moving away from the NNLS problem, the q-exponential non-linear least squares method offers a statistics-driven approach to multiexponential modeling [17].

It is for these same reasons that the matrix pencil method (MPM) was developed and used to treat a wide range of relaxometry data from the study of textbook two component samples with different spin–lattice and spin–spin relaxation times to unique emerging materials with new properties and vaccine-binding biomolecules [18]. The work builds on earlier uses of the MPM in high-field solid-state NMR problems [19], speech analysis [20], and remote radar sensing [21]. The MPM is an algebraic way to treat transient, exponential signals. As it is not a mathematical transformation, the MPM sidesteps some of the complications encountered when using ILT, providing clear, discrete solutions that make it well-suited for NMR relaxometry studies.

Initial work in this area was designed to advertise the usefulness of MPM to the broader NMR community by including applications from a wide range of disciplines as well as measurements of the core relaxation parameters [18]. A more recent, purely experimental paper considered the ultimate resolving capability of the conventional MPM algorithms introduced in the initial work [22]. Here two separate sample containers housing water with different paramagnetic impurity concentrations and known spin–lattice relaxation times were simultaneously placed on top of a commercially available Magritek PM-25 single-sided NMR instrument. The analysis of the two-component saturation recovery transient signals revealed that the resolving power of MPM was roughly twice that of ILT. In some cases, operation with

MPM offered even more gain over ILT. However, in these cases, perfect amplitude fidelity or reproduction of accurate fractional relaxation coefficient contributions to the signal was sacrificed.

It was recognized in that recent experimental work that signal noise is the primary factor limiting MPM resolution. The greater the signal noise, the lower the resolution. The work reported here and described below acknowledges that the MPM reports eigenvalues that, in the absence of noise, are relaxation coefficients λ_m that depend on the inherent relaxation rate and signal sampling time Δt. Thus, the ability to resolve two relaxation times or rates reduces to resolving two relaxation coefficients that depend on the choice of Δt. This fact suggests that there should be an optimum Δt value that provides the best chance of resolving relaxation coefficients with similar relaxation time values. The next section describes how to maximize the sum of square difference of relaxation coefficients SS_λ to obtain the best data sampling time Δt_{max} and motivates a performance metric or noise tolerance N_T that can be used to verify the Δt_{max} value theoretically as well as to compare to actual experimental measurements.

4.2 Theory

The application of both one- and two-dimensional MPM to NMR relaxometry data is described in greater detail elsewhere [18]. In the one-dimensional case considered here, the measured non-oscillatory, damped, relaxometry signal $s((n-1)\Delta t)$ sampled at the time $(n-1)\Delta t$ serves as MPM algorithm input. All index counters like n, m, and q in the following equations are understood to begin at value one. Central to the MPM approach is representation of the signal in terms of a linear combination of damped exponential functions as

$$s\big((n-1)\Delta t\big) = \sum_{m=1}^{mpts} A_m \lambda_m^n + N\big((n-1)\Delta t\big) \tag{4.1}$$

where the relaxation coefficient is $\lambda_m = \exp(-R_m \Delta t)$, the relaxation rate $R_m = 1/T_m$ is inversely proportional to the time constant Tm, the amplitude of the m^{th} relaxing signal component is A_m, and the total number of relaxing components is mpts. Standard Gaussian white noise represented by the zero average and cross-

correlation, $\langle N(n\Delta t)\rangle = \langle N(n\Delta t)N(m\Delta t)\rangle = 0$, non-zero mean square, $\langle N(n\Delta t)^2\rangle = \langle N^2\rangle \neq 0$, function $N((n-1)\Delta t)$ is used as the noise source as described in more detail in the Experimental section. The two primary outputs from MPM signal analysis are an amplitude matrix $\tilde{V}$ and eigenvalues z_m. In the absence of noise where $N((n-1)\Delta t) = 0$ for all choices of n in Eq. (4.1), the MPM analysis disentangles the linear combination of exponentials to provide an estimate of the signal amplitudes rates from the diagonal elements of the amplitude matrix as $A_m = V(m,m)$, and since $\lambda_m = z_m$, as $R_m = \log(z_m)/\Delta t$.

In the presence of noise, the eigenvalues z_m deviate from their relaxation coefficient, noise-free values, λ_m. Not surprisingly, the closer the λ_m values, the larger the deviation of z_m from λ_m for fixed mean square noise amplitude $\langle N^2\rangle$. The dependence of the relaxation coefficient values λ_m on the dwell time Δt suggests that there will be a sampling time Δt_{max} that leads to the largest separation between λ_m values. This time can be determined by maximizing the sum of square differences as a function of Δt

$$SS_\lambda = \sum_{m=1}^{mpts} \left(\lambda_m - \bar{\lambda}\right)^2 \quad with \quad \bar{\lambda} = \frac{1}{mpts}\sum_{m=1}^{mpts} \lambda_m \tag{4.2}$$

an effort that will provide the least sensitivity of the z_m values to noise. A useful way to study the resolution limits of the MPM for both theoretical and real experimental data is to compare the sum of square differences obtained in the noise-free case shown in Eq. (4.2) to the sum of squares based purely on MPM eigenvalues with added noise

$$SS_z = \sum_{m=1}^{mpts} (z_m - \bar{z})^2 \quad with \quad \bar{z} = \frac{1}{mpts}\sum_{m=1}^{mpts} z_m \tag{4.3}$$

using the noise tolerance

$$N_T = \frac{SS_z - SS_\lambda}{SS_z + SS_\lambda} \times 100 \tag{4.4}$$

that describes the percent difference between SS_z and SS_λ for many values of Δt. In practice this would be accomplished by determining SS_λ and SS_z at different dwell times Δt. This is most easily done by first performing MPM on the raw transient sampled at the dwell time Δt. Subsequent MPM analyses are then performed on signals generated from the raw transient by taking every other data point at $2\Delta t$, every third

data point at $3\Delta t$ and so on as described in Fig. 1a. In the noise-free case, $SS_z = SS_\lambda$ and $N_T = 0$ for all $q\Delta t$ values. As the noise increases, SSz deviates from SS_λ, N_T becomes non-zero, and the ability of MPM eigenvalues to reproduce relaxation coefficients degrades. In the case of a purely theoretical comparison, one knows the λm values from knowledge of the R_m rates and multiples of the dwell time $q\Delta t$ enabling calculation of SS_λ. The value of SS_z is obtained from the z_m eigenvalues generated from MPM analysis of a decaying transient signal with added random noise having the same dwell time multiple $q\Delta t$. For experimental comparisons, samples with known R_m values in separate containers housed in the detection coil are used. Since the R_m values are known from separate measurements of each container alone, SS_λ can be calculated for each multiple of the dwell time $q\Delta t$. The MPM analysis of the bulk signal obtained from all the containers simultaneously placed in the magnet and detection coil provides the z_m eigenvalues at each $q\Delta t$ needed to calculate SS_z and thus a value for N_T.

To understand the meaning of and how to develop and use SS_λ, SS_z, and N_T, consider the special signal involving just two relaxing components, or equivalently a biexponential decay signal where $\lambda_1 = \exp(-R_1\Delta t)$ and $\lambda_2 = \exp(-R_2\Delta t)$ for the respective decay rates R_1 and R_2. It should be clear that there are many choices of λ_1 and λ_2 given the dwell time Δt and that the subscript numbers indicate different relaxation rates not spin–spin versus spin–lattice relaxation rates. Ignoring the shaded gray region of Fig. 4.1b that will be described below, the solid, curved line in the northwest corner of the plot shows the

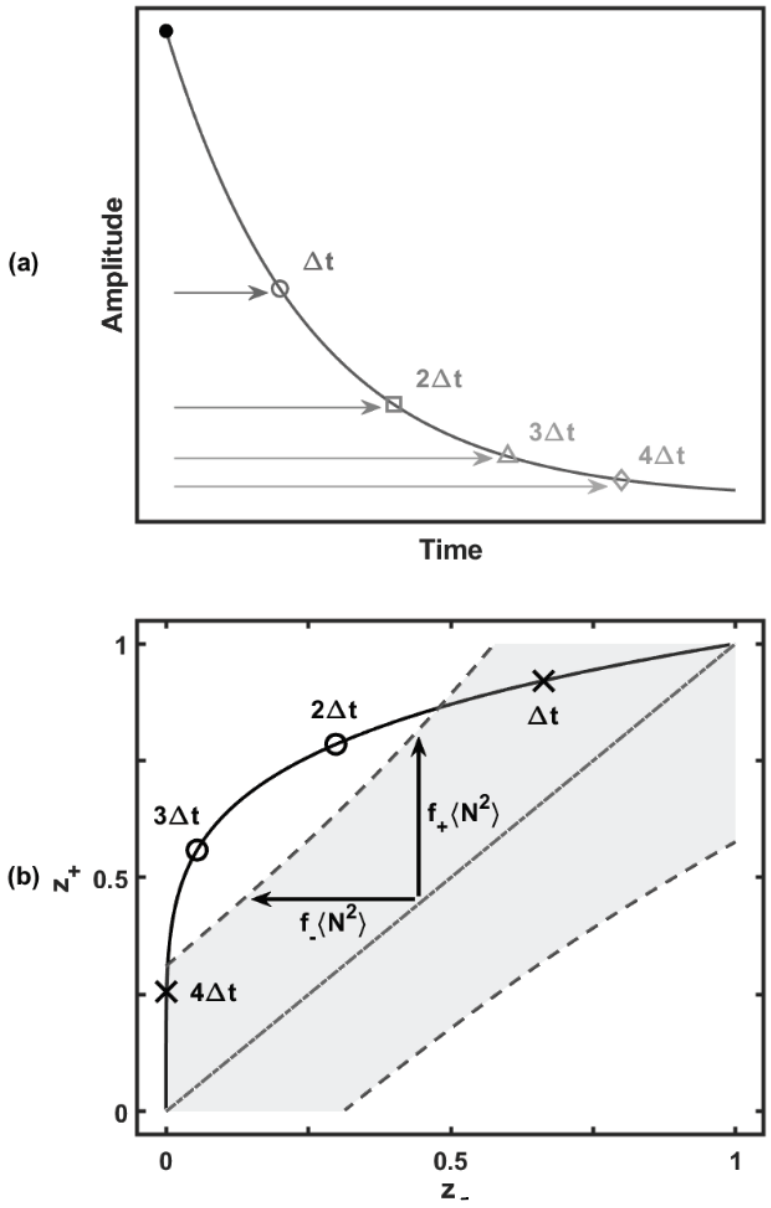

Figure 4.1. *The decay signal shown in (a) as the solid line helps graphically identify the signal points used for the MPM analysis. For example, for q = 1, the points separated by Δt and indicated with a solid circle, open circle, square, and triangle are used, while for q = 2, the points separated by 2Δt and indicated with a solid circle, open square, open diamond and the s(6Δt) point not shown are used. The plot shown in (b) for two relaxation coefficients shows how the shaded gray region representing noise suggests that the points at Δt and 4Δt shown as "x" symbols will present large N_T values while the open symbols at 2Δt and 3Δt yield smaller N_T values with the smallest being at Δt_{max}. The shaded gray region bounds are described by the $f_+\langle N^2\rangle$ and $f_-\langle N^2\rangle$ noise terms in the two relaxation coefficient eigenvalues shown in Eq. (4.12)*

behavior of λ_1 and λ_2 for fixed R_1 and R_2 values as a function of variable dwell time Δt. Recall that this line describes the eigenvalues $z_{+,-}$ in the absence of noise as $z_{+,-} = \lambda_{1,2}$ in this case. The model transient signal shown in Fig. 4.1a obtained with a fixed Δt can be used to explore the solid line curve in Fig. 4.1b created with a continuous Δt variable by taking each point at Δt, every other point at $2\Delta t$, every third point at $3\Delta t$, every fourth point at $4\Delta t$, etc. When operating in this way, the open circle, "x", and "*" symbols shown on the solid line indicate the $\lambda_{1,2}$ pairs obtained at the chosen $q\Delta t$ value. Here $q \geq 1$ is an index. The dot-dashed line along the diagonal in the plot represents the condition where $\lambda_1 = \lambda_2$. In the absence of noise, λ_1 and λ_2 are not resolved because they are the same. As all the five symbolled points on the solid curve in Fig. 4.1b for different $q\Delta t$ are displaced from the $\lambda_1 = \lambda_2$ diagonal, they are in principle able to be resolved in the absence of noise. However, the best resolution will occur for the largest difference between λ_1 and λ_2 or for the Δt value obtained from maximizing SS_λ shown in Eq. (4.2) above. For two components, SS_λ reduces to the difference $\lambda_1 - \lambda_2$ which is captured by the dotted line along the anti-diagonal in Fig. 4.1b. When maximized as a function of Δt, the difference yields the optimized time $\Delta t_{max} = \log(R_2/R_1)/(R_2 - R_1)$ and the most distinguishable relaxation coefficient $\lambda_1^{max} = (R_1/R_2)^{R1/(R2-R1)}$ and $\lambda_2^{max} = (R_1/R_2)^{R2/(R2-R1)}$. Graphically in the two-component case, the Δt_{max} value obtained from maximizing SS_λ corresponds to finding the longest vector perpendicular to the $\lambda_1 = \lambda_2$ diagonal and between the diagonal and the $\lambda_{1,2}$ curve.

In the absence of noise, any two λ_m values are always completely resolved, although the best resolution occurs at Δt_{max} with the associated λ_1 max and λ_2 max values as just described. Moreover, the parameter N_T in Eq. (4.3) is always zero in the absence of noise as $SS_z = SS_\lambda$. To determine the effect of added noise in the case of two relaxing components, MPM can be accomplished analytically, an approach that avoids the uncertainties in addition to the mysteries of the singular valued decomposition included in most MPM algorithms [15, 16]. Here one first uses the measured data array $s((n-1)\Delta t)$ sampled at the times $(n-1)\Delta t$ to construct two data matrices from just four points.

$$\boldsymbol{Y}_1 = \begin{bmatrix} s(0) & s(q\Delta t) \\ s(q\Delta t) & s(2q\Delta t) \end{bmatrix} \quad and \quad \boldsymbol{Y}_2 = \begin{bmatrix} s(q\Delta t) & s(2q\Delta t) \\ s(2q\Delta t) & s(3q\Delta t) \end{bmatrix} \tag{4.5}$$

Notice that if q = 1, the first four points in the measured data s((n-1)Δt) array are used and $\lambda_m = \exp(-R_m\Delta t)$. For q = 3, every third data point is used to select the {s(0), s(3Δt), s(6Δt), s(9Δt)} four points for analytical MPM analysis as described in Fig. 1a and $\lambda_m = \exp(-3R_m\Delta t)$. The matrix pencil equation

$$(\boldsymbol{Y}_1^{-1} \cdot \boldsymbol{Y}_2 - z_m \boldsymbol{E}) \cdot \vec{p}_m = 0 \tag{4.6}$$

in terms of the unit matrix $\boldsymbol{E}$ and the eigenvectors $\vec{p}_m$ is then solved for the eigenvalues z_m. Essentially one finds the inverse matrix

$$\boldsymbol{Y}_1^{-1} = \frac{1}{s(0)s(2q\Delta t) - s(q\Delta t)^2}\begin{bmatrix} s(2q\Delta t) & -s(q\Delta t) \\ -s(q\Delta t) & s(0) \end{bmatrix} \tag{4.7}$$

and then the eigenvalues of the matrix product

$$\boldsymbol{Y}_1^{-1} \cdot \boldsymbol{Y}_2 = \begin{vmatrix} 0 & \dfrac{s(2q\Delta t)^2 - s(q\Delta t)s(3q\Delta t)}{s(0)s(2q\Delta t) - s(q\Delta t)^2} \\ 1 & \dfrac{s(0)s(3q\Delta t) - s(q\Delta t)s(2q\Delta t)}{s(0)s(2q\Delta t) - s(q\Delta t)^2} \end{vmatrix} \tag{4.8}$$

in the usual way as

$$z_{\pm} = \frac{1}{2}\frac{s(0)s(3q\Delta t) - s(q\Delta t)s(2q\Delta t)}{s(0)s(2q\Delta t) - s(q\Delta t)^2} \pm \sqrt{\frac{1}{4}\left(\frac{s(0)s(3q\Delta t) - s(q\Delta t)s(2q\Delta t)}{s(0)s(2q\Delta t) - s(q\Delta t)^2}\right)^2 + \frac{s(2q\Delta t)^2 - s(q\Delta t)s(3q\Delta t)}{s(0)s(2q\Delta t) - s(q\Delta t)^2}} \tag{4.9}$$

These analytical expressions for MPM analysis can be used to explore the effect of signal noise on the $z_{+,-}$ eigenvalues and their deviation from λ_1 and λ_2. For two relaxing components with amplitudes A_1 and A_2, Eq. (4.1) implies that four consecutive signal points with noise beginning at t = 0 are

$$\begin{aligned} s(0) &= A_1 + A_2 + N(0) & s(2q\Delta t) &= A_1\lambda_1{}^2 + A_2\lambda_2{}^2 + N(2q\Delta t) \\ s(q\Delta t) &= A_1\lambda_1 + A_2\lambda_2 + N(q\Delta t) & s(3q\Delta t) &= A_1\lambda_1{}^3 + A_2\lambda_2{}^3 + N(3q\Delta t) \end{aligned} \tag{4.10}$$

Taylor expansion of Eq. (4.9) to second order in terms of these four independent noise variables along with knowledge that the average noise and cross-correlation are zero, $\langle N(n\Delta t)\rangle = \langle N(n\Delta t)N(m\Delta t)\rangle = 0$, and with non-zero mean square, $\langle N(n\Delta t)^2\rangle = \langle N^2\rangle \neq 0$, results in two noise factors

$$f_+ = [1 + A_1A_2(\lambda_1^4 + 4\lambda_1^2 + \lambda_2^2 + \lambda_1^4\lambda_2^2 + 4\lambda_1^3\lambda_2 + 4\lambda_1^2\lambda_2^2 + 4\lambda_1\lambda_2)]$$
$$- \frac{A_2^2[2\lambda_2^4 + 2\lambda_2^2 - \lambda_1^2 + \lambda_1\lambda_2^5 - \lambda_1^2\lambda_2^4 + 2\lambda_1\lambda_2^3 - 4\lambda_1^2\lambda_2^2 - \lambda_1\lambda_2]}{(\lambda_1 - \lambda_2)^5}$$

$$f_- = [-1 - A_1A_2(\lambda_2^4 + 4\lambda_2^2 + \lambda_1^2 + \lambda_1^2\lambda_2^4 + 4\lambda_1\lambda_2^3 + 4\lambda_1^2\lambda_2^2 + 4\lambda_1\lambda_2)]$$
$$- \frac{A_1^2[2\lambda_1^4 + 2\lambda_1^2 - \lambda_2^2 + \lambda_1^5\lambda_2 - \lambda_1^4\lambda_2^2 + 2\lambda_1^3\lambda_2 - 4\lambda_1^2\lambda_2^2 - \lambda_1\lambda_2]}{(\lambda_1 - \lambda_2)^5} \quad (4.11)$$

that can be used to approximate the two eigenvalues to first order in $\langle N^2 \rangle$ as

$$z_{+,-} \simeq \lambda_{1,2} + f_{+,-}\langle N^2 \rangle \quad (4.12)$$

These two equations are interesting because they suggest that the added signal noise does not directly yield eigenvalues that fluctuate equally about an average $z_{+,-} = \lambda_{1,2}$. Rather, the added signal noise induces a shift of the $z_{+,-}$ eigenvalues away from the noise-free $\lambda_{1,2}$ values. It is this shift that is captured by the shaded gray region in Fig. 4.1b with bounds indicated by dashed black lines that correspond to the $f_+\langle N^2 \rangle$ and $f_-\langle N^2 \rangle$ factors appended to the $\lambda_{1,2}$ relaxation coefficients in the $z_{+,-}$ eigenvalues in Eq. (4.12). A larger average signal noise $\langle N^2 \rangle$ will generate a larger shaded gray region on this plot. Consideration of the eigenvalue difference, $z_+ - z_- = \lambda_1 - \lambda_2 + (f_+ - f_-)\langle N^2 \rangle$, indicates that the λ_1–λ_2 noise-free value increases to a larger $\langle N^2 \rangle$-dependent number where the increase calculated from Eq. (4.11), $(f_+ - f_-)\langle N^2 \rangle$, can be used to determine the noise tolerance defined in Eq. (4.4) as

$$N_T = \frac{(f_+ - f_-)\langle N^2 \rangle}{2(\lambda_1 - \lambda_2) + (f_+ - f_-)\langle N^2 \rangle} \times 100 \quad (4.13)$$

It is important to remember that the N_T value directly depends on $q\Delta t$ through the definition of the $\lambda_{1,2}$ values and that the best separation of the $z_{+,-}$ eigenvalues will be when $q\Delta t = \Delta t_{max}$ and when NT is minimum. In terms of the plot in Fig. 4.1b, the N_T value for the points at Δt and $4\Delta t$ labeled with an "x" and firmly embedded in the shaded region will have large, close to 100% N_T values because the noise is so large that the relaxation components are not resolved. The open circles at $2\Delta t$ and $3\Delta t$ will have smaller N_T values. However, the point for Δt_{max} labeled with an "*" will display the minimum N_T value and thus be most easily resolved in the presence of noise. As long as the Δt_{max} point on the $\lambda_{1,2}$ curve is greater than the

system noise or equivalently lies outside of the gray shaded region in Fig. 4.1b, the N_T value will approach zero and the two components will likely be resolved. If, however, this same point falls within the shaded gray area, a case not shown here, the N_T value will become much greater and a reliable estimate of the $\lambda_{1,2}$ values is not possible given the inherent signal noise.

A similar graphical interpretation of SS_λ drives the determination of Δt_{max} for signals involving more than just two components. In the three-component case, the three $\lambda_1 = \exp(-R_1 q\Delta t)$, $\lambda_2 = \exp(-R_2 q\Delta t)$, and $\lambda_3 = \exp(-R_3 q\Delta t)$ relaxation coefficients for the three R_1, R_2, and R_3 rates label three orthogonal axes and maximization of SS_λ amounts to determining the maximum perpendicular distance from the body diagonal to the $\lambda_{1,2,3}$ curve. Noise in this case broadens the body diagonal line to the surrounding volume and only certain Δt values will provide $\lambda_{1,2,3}$ points outside of this volume. These Δt sampling rates produce small N_T values and thus faithful experimental estimates of the true relaxation properties can be recovered. The effect of the added noise can be mathematically considered in the same way it was for two relaxation coefficients above. The additional λ_3 contribution to the signal s(t) requires an additional two signal points s(4qΔt) and s(5qΔt) to accomplish reduced dimensional MPM analysis. In this case, the $\boldsymbol{Y}_1$ and $\boldsymbol{Y}_2$ matrices are constructed as

$$\boldsymbol{Y}_1 = \begin{bmatrix} s(0) & s(q\Delta t) & s(2q\Delta t) \\ s(q\Delta t) & s(2q\Delta t) & s(3q\Delta t) \\ s(2q\Delta t) & s(3q\Delta t) & s(4q\Delta t) \end{bmatrix} \qquad \boldsymbol{Y}_2 = \begin{bmatrix} s(q\Delta t) & s(2q\Delta t) & s(3q\Delta t) \\ s(2q\Delta t) & s(3q\Delta t) & s(4q\Delta t) \\ s(3q\Delta t) & s(4q\Delta t) & s(5q\Delta t) \end{bmatrix} \tag{4.5}$$

and the $\boldsymbol{Y}_1^{-1} \cdot \boldsymbol{Y}_2$ eigenvalues $z_{1,2,3}$ are calculated to find $\lambda_{1,2,3}$ and thus $R_{1,2,3}$ given qΔt. Although analytical solutions for the $z_{1,2,3}$ eigenvalues were generated akin to the two-component case shown in Eq. (4.12), the overwhelming complexity and number of terms prevent reproduction here. Instead, numerical diagonalization of $\boldsymbol{Y}_1^{-1} \cdot \boldsymbol{Y}_2$ was used to calculate N_T for MPM algorithm performance estimates on purely theoretical and experimental data.

Extension of this approach to more than three relaxing components is straightforward. The MPM analysis of signals with four relaxing components requires eight signal point and five relaxing components

requires ten signal points. A signal with *m* relaxing components will thus require 2m points for treatment with reduced MPM, and of course numerical matrix diagonalization is required.

4.3 Experimental

Gadopentetic acid (Gd-DTPA) and sodium chloride were obtained from Sigma-Aldrich and used without further purification. In-house deionized water was used to prepare a 0.9% (by mass) sodium chloride stock solution. Six samples in the 0.05 mM < [Gd-DTPA] < 2 mM concentration range were prepared from this stock solution and are listed in Table 1. All NMR measurements were accomplished using a Tecmag Apollo controlled, Aspect Instruments M100, 1.01 T, magnetic resonance imaging spectrometer operating at a 43.7 MHz ^{1}H Larmor frequency. All MPM analyses of experimental data were accomplished on transient, exponentially damped signals obtained with the standard Carr–Purcell–Meiboom–Gill (CPMG) pulse sequence [23]. The time between the 1024 consecutive collected spin echoes was 10 ms, the $\pi/2$ pulse time with 27 W of applied power was 35 μs and multiple samples easily fit within the 6 cm diameter, 10 cm long NMR detection coil. Signal averaging was used to sum eight separate signal acquisitions and this averaged signal corresponds to one experimental trial. The experimental data shown in all figures correspond to a 512-trial average. Experimental estimates of $\langle N^2 \rangle$ values were obtained by calculating the mean square of the last 200 points of the CPMG transient after scaling the raw signal so that the first point is one.

All data processing and simulations were accomplished using Matlab (Mathworks, Natick, MA). Because the measured transient CPMG signals from the six standard Gd-DTPA-doped samples were single-exponential, regression to $\exp(-(n-1)\Delta t/T_2)$ could be used to accurately determine T_2 values ($R_2 > 0.95$). The noise in numerical transient signal simulations was established by scaling random numbers $\mathcal{N}(0,1)$ extracted from a zero-centered, width of one, standard normal distribution by the root mean square signal noise as $N((n-1)\Delta t) = \mathcal{N}(0,1)\langle N^2 \rangle^{1/2}$ so that the mean square average and cross-correlation at each Δt reduce

to $\langle N((n-1)\Delta t)^2\rangle = \langle N^2\rangle$ and zero. In all calculations, 15,000 noisy CPMG decay signals are used to calculate an average transient decay response that is used to estimate SS_z.

Table 1. *Summary of water T_2 values as a function of Gd-TPA concentration*

[Gd-TPA] (mM)	T_2(ms)	R (Hz)
0.05	1,724	0.58
0.10	1,471	0.68
0.25	592	1.69
0.50	448	2.23
1.00	229	4.36
2.00	98.1	10.2

4.4 Results and Discussion

The goal of this work is to identify the data sampling time Δt_{max} that maximizes the resolution of as many relaxation components λ_m as possible in the presence of real signal noise described by $\langle N^2\rangle$. It is the maximization of SS_λ as a function of Δt in Eq. (4.2) that identifies Δt_{max} and it is the value of N_T in Eq. (4) as a function of $q\Delta t$ that reports on the resolution performance. Here N_T values of zero are considered to perform well while N_T values exceeding zero perform less well. The theoretical results in Fig. 4.2(a–d) for two and three relaxation components reflect these comments.

The open circles shown in Fig. 4.2(a, b) describe the behavior of Eq. (4.13) as a function of $q\Delta t$ and $\langle N^2\rangle$ for two relaxing components with different R_1 and R_2 values. The relevant R_m values in units of Hz are shown in the plot mounted boxes. The solid lines correspond to numerical diagonalization of Eq. (4.8) followed by averaging over the random number generated noise $N(q\Delta t)$. The similarity of the analytical behavior of Eq. (4.13) to the numerical results in the neighborhood of Δt_{max} indicated by the

vertical dashed line, especially at very low $\langle N^2 \rangle$ value, suggests that it is safe to use numerical diagonalization followed by averaging to determine N_T values. The deviation of the analytical and numerical results displayed in Fig. 4.2a at large $q\Delta t$ and $\langle N^2 \rangle$ values is not a limitation of numerical diagonalization. Rather it is due to restricting the eigenvalue expansion to the second-order term in the Taylor expansion used to develop the analytical eigenvalues in Eq. (4.12). Both the analytical and numerical approaches shown in Fig. 4.2b demonstrate that as the added noise $\langle N^2 \rangle$ increases the range of $q\Delta t$ times that yield low to zero N_T values decreases and becomes centered on the Δt_{max} value predicted from maximizing SS_λ. It is only when $\langle N^2 \rangle$ exceeds 10^{-4} that N_T noticeably increases from zero implying that the added noise is too great to adequately recover meaningful $\lambda_{1,2}$ values from the $z_{+,-}$ eigenvalues even though operation at Δtmax is insured. In other words, as signal noise increases, the range of $q\Delta t$ values providing $z_{+,-}$ eigenvalues that faithfully report the $\lambda_{1,2}$ relaxation coefficient values decreases. In terms of the plot shown in Fig. 4.1b, as noise increases, the overall length of the solid line outside of the shaded gray area decreases and when $\langle N^2 \rangle$ exceeds 10^{-4}, the entire $\lambda_{1,2}$ curve is within the shaded gray area. The similarity of the solid line graphs with minima centered on Δt_{max} shown in Fig. 4.2b demonstrates that relaxation coefficient amplitude has little effect on both Δt_{max} and N_T, consistent with the determination of Δtmax from SS_λ where the relative contribution of the relaxation components to the full signal is not considered.

Numerical diagonalization of the $\boldsymbol{Y}_1^{-1} \cdot \boldsymbol{Y}_2$ matrix is used in all cases where more than two components are involved. The three-component case shown in Fig. 4.2c, like Fig. 2a, considers N_T as a function of $q\Delta t$ and $\langle N^2 \rangle$ for three equal amplitude components with three different rates $R_{1,2,3}$ while Fig. 4.2d, like Fig. 4.2b, fixes $\langle N^2 \rangle$ and the $R_{1,2,3}$ values while varying the three amplitudes $A_{1,2,3}$. The three-component calculated results in Fig. 4.2(c, d) convey similar information as the two-component results in Fig. 4.2(a, b). As the noise $\langle N^2 \rangle$ increases, the range of $q\Delta t$ values where N_T equals zero decreases and centers on the Δt_{max} value predicted from maximizing SS_λ as a function of Δt. There also appears to be very little dependence on the fractional contribution of each relaxation coefficient to the signal at fixed

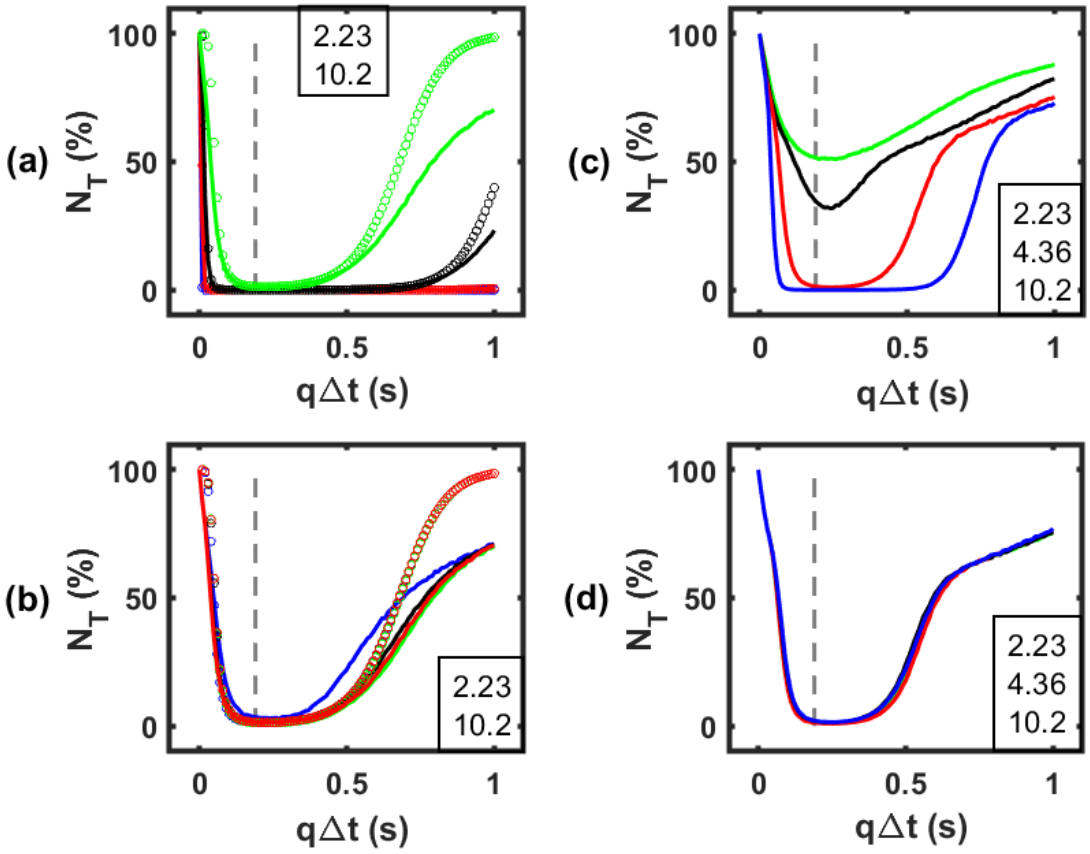

Figure 4.2. *Purely theoretical predictions of the behavior of* Δt *max and* N_T *for two (a, b) and three (c, d) relaxation coefficient cases as a function of added noise. The vertical dashed line in all the plots indicates the value of* Δt *max obtained from maximizing* SS_λ *in Eq. (4.2) as a function of* Δt*. For easy reference, the appropriate relaxation rate* R_m *values in units of Hz are shown in the small box in each plot. The solid lines shown in all plots correspond to numerically determined estimates of* N_T*. The open circles in (a) and (b) represent the two-component analytical result shown in Eq. (4.13). The two-coefficient comparison shown in (a) at the four* $\langle N^2 \rangle = 10^{-10}$ *(green),* 10^{-8} *(black),* 10^{-6} *(red), and* 10^{-4} *(blue) noise levels used transient signals s(t) with equal amplitude* $A_1 = A_2 = 0.5$ *exponential decay functions. One* $\langle N^2 \rangle = 10^{-4}$ *noise value was used to generate (b) for four different exponential decay function amplitude pairs* $\{A_1,A_2\} = \{0.5,0.5\}$ *(green),* $\{0.25,0.75\}$ *(black),* $\{0.33,0.67\}$ *(red), and* $\{0.1,0.9\}$ *(blue). The three-coefficient comparison shown in (c) at the same four* $\langle N^2 \rangle$ *noise levels used transient signals s(t) with equal amplitude* $A_1 = A_2 = 0.33$ *exponential decay functions. One* $\langle N^2 \rangle = 10^{-8}$ *noise value was used to generate (d) for four different exponential decay function amplitude triples* $\{A_1,A_2,A_3\} = \{0.33,0.33,0.33\}$ *(green),* $\{0.25,0.25,0.5\}$ *(black),* $\{0.2,0.4,0.4\}$ *(red), and* $\{0.14,0.29,0.57\}$ *(blue). Some of the colors are difficult to see in (d) as the lines overlap (color figure online).*

$\langle N^2 \rangle$ value, as judged from the similarity of the numerically generated curves in Fig. 4.2d. The important difference between the two- and three-component cases shown in Fig. 4.2 is sensitivity to noise. The three-component results always present N_T values much greater than the corresponding two-component case for the same applied $\langle N^2 \rangle$ value. For example, for $\langle N^2 \rangle = 10^{-4}$ in Fig. 4.2a, N_T is ca. 5% at most, while in Fig. 4.2c, N_T exceeds 50%. This effect can also be observed in the comparison of Fig. 4.2(b, d) where similarly shaped curves are produced from drastically different applied $\langle N^2 \rangle$ values, here 10^{-6} and 10^{-8} respectively. The reason that the three-component case appears to be more sensitive to noise is directly related to the proximity of the chosen relaxation rates. The two-component case uses $R_1 = 2.23$ Hz and $R_2 = 10.2$ Hz while the three-component case includes the additional 4.36 Hz rate. It is the smaller difference of 2.13 Hz in the three-component case in comparison to the 7.96 Hz difference in the two-component case that likely leads to this sensitivity. If the added third rate led to a similar 7.96 Hz difference, then a similar noise sensitivity would be expected.

The set of six samples with the Gd-DTPA concentration in Table 4.1 was prepared, placed in six separate 1 mL plastic containers, and separately analyzed with the CPMG pulse sequence to obtain the listed T_2 time constants. The value of R reported in Table 1 is the inverse of the T_2 value. These samples were prepared to verify the predictions described in Fig. 4.2 by obtaining transient CPMG decay signals from different pairs, triples and quadruples of these tubes simultaneously placed inside of the NMR detection coil. The relaxation rates in Hz for the samples being simultaneously studied are included in all figure legends.

The two-component predictions shown in Fig. 4.2(a, b) are reflected in the experimental measurements. Here different pairs of the samples listed in Table 4.1 were simultaneously placed inside of the NMR detection coil and explored with the CPMG pulse sequence. The left-hand column in Fig. 4.3 shows how the N_T value changes when the relaxation properties of one of the containers are changed while keeping those for the second container fixed. The relaxation rates obtained from the separate individual containers in Hz are shown in the legends. As the relaxation rates of the separate samples converge, the relaxation coefficients λ_m at all $q\Delta t$ values become more similar. Experimental results

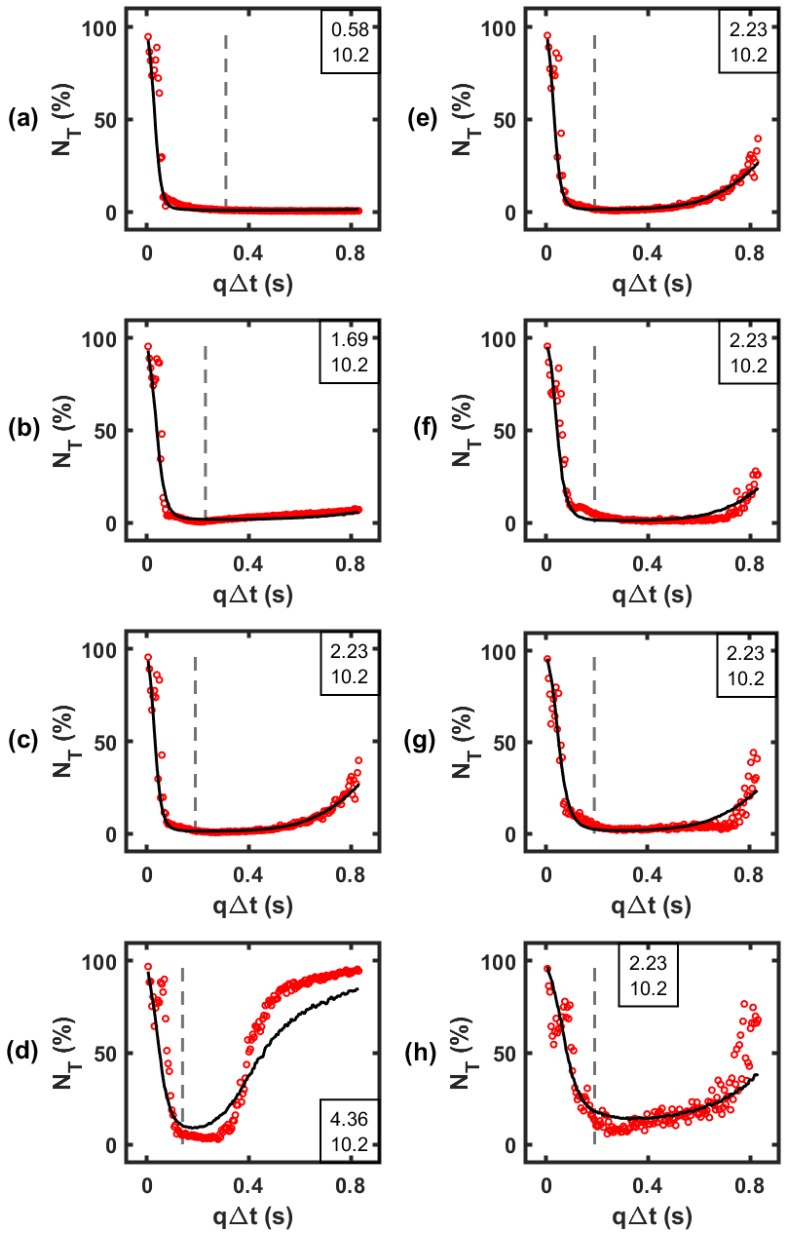

Figure 4.3. *Comparison of experimental (open red circles) to theoretical (solid black line) N_T values for two-component signals. The vertical dashed line in all the plots indicates the value of Δt_{max} obtained from maximizing SS_λ in Eq. (4.2) as a function of Δt. For easy reference, the appropriate relaxation rate R_m values in units of Hz are shown in the small box in each plot. The results shown in the left-hand column (a–d) explore the effect of different R_m values for equal amplitude components while those shown in the right-hand column (e–h) have fixed R_m values with the respective {0.50,0.50}, {0.59,0.41}, {0.71,0.29}, and {0.91,0.09} relaxation coefficient amplitudes established using variable volume samples. The $\langle N^2 \rangle$ values used in the solid black line simulated results were obtained from the measured raw transient signal (color figure online).*

shown as the open circles agree well with the solid line theoretical predictions. The theoretical result is much smoother than the experimental data because the experimental results were generated from an average of 512, 8 scan transient signal trials with noise while the theoretical prediction involved averaging over 15,000 transient signals with the same noise amplitude as the measured data. The right-hand column in Fig. 4.3 displays an expected small variation in shape as a function of relaxation coefficient amplitude confirming the theoretical predictions summarized in Fig. 2b. The graphs presented in Fig. 4.3 suggest that the best MPM performance with noise is when $q\Delta t = \Delta t_{max}$ as the N_T value is minimum. All the N_T values for equal amplitude, similar relaxation coefficients shown in Fig. 4.3d and for drastically different amplitude relaxation coefficients shown in Fig. 4.3h are greater than zero. This observation suggests that even operation at Δt_{max} will not reliably recover accurate relaxation coefficients and thus relaxation times given the experimental noise level.

A similar good agreement between experiment and theory is enjoyed in equal amplitude three and four relaxation coefficient studies as shown in the left- and righthand columns in Fig. 4.4, respectively. Here three and four separate equal-volume containers, each loaded with one of the samples listed in Table 1, were simultaneously placed in the NMR detection coil and explored with the CPMG pulse sequence. The shape of the curves shown in Fig. 4.4(b, d) is to be expected by comparison to Fig. 4.3d. The difference between these results is the addition of the R_1 = 0.58 Hz and 2.23 Hz rate samples in Fig. 4.4(b, d), respectively. In addition to being more sensitive to signal noise as judged by the larger $q\Delta t$ range of $N_T > 0$ values in Fig. 4.4(b, d), the added relaxation rate sample also shifts Δt_{max} to longer values. The N_T values much closer to zero displayed in Fig. 4.4(a, c) are also to be expected with reference to Fig. 3(b, c), respectively. Here the only difference is the addition of a third R_1 = 0.58 Hz sample container to the NMR detection coil prior to generating the results shown in Fig. 4.4(a, c). Once again, the Δt_{max} values shift to a longer time due to the addition of the third sample. Even though the N_T values for the three-component case suggest that the inherent experimental noise is too great to resolve the relaxation coefficients in Fig. 4.4d, the overall shape of the N_T curve is easily reconciled with respect to the two relaxation coefficient

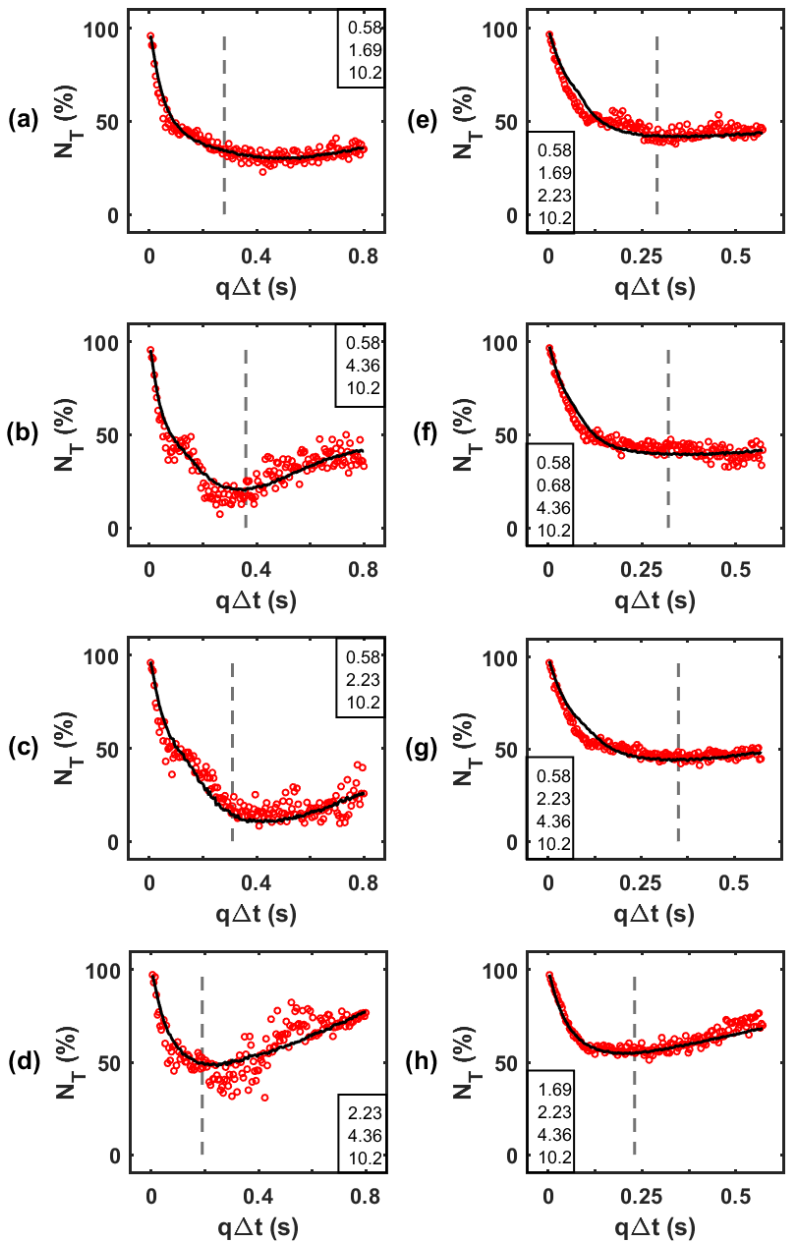

Figure 4.4. *Comparison of experimental (open red circles) to theoretical (solid black line) N_T values for equal amplitude three (a–d) and four (e–h) component signals. The vertical dashed line in all the plots indicates the value of Δt_{max} obtained from maximizing SSλ in Eq. (4.2) as a function of Δt. For easy reference, the appropriate relaxation rate R_m values in units of Hz are shown in the small box in each plot (color figure online)*

results shown in Fig. 4.3. Such a simple understanding does not seem possible when four relaxation coefficients are involved as shown in the right-hand column in Fig. 4.4. Like Fig. 4.4d, the N_T value in all

the four component cases shown in Fig. 4.4e–h exceeds zero meaning that the MPM approach does not reliably resolve these four components given the level of experimental noise. Data sampling at the Δt_{max} value still produces N_T values greater than zero although in most cases NT is minimum at $q\Delta t = \Delta t_{max}$.

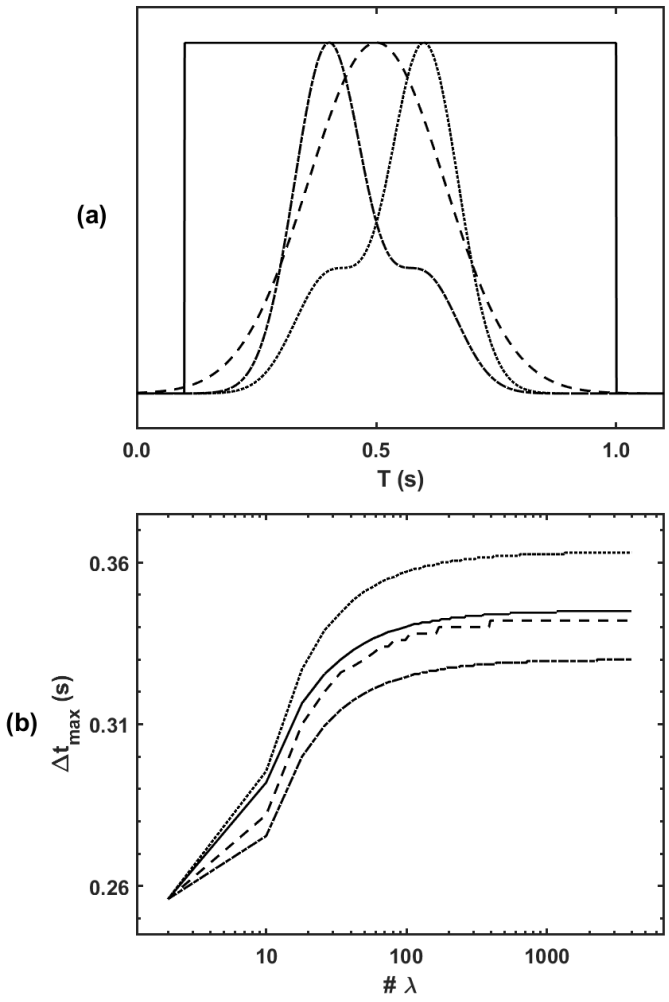

Figure 4.5. *Dependence of Δt max on the number of uniformly spaced components in the 0.1 s < T < 1 s range. The asymptotic Δtmax values shown in (b) for the uniform (solid), Gaussian (dashed), and oppositely skewed, bimodal Gaussian (dash-dotted and dotted) amplitude profiles in (a) are 0.35, 0.34, 0.32, and 0.37 respectively.*

The agreement between experiment and theory displayed in Figs. 4.3, 4.4 validates the reduced MPM approach used here to calculate N_T and its relationship to Δt_{max}. This strong agreement allows one to ask how small the experimental noise $\langle N^2 \rangle$ must be to resolve all four relaxation coefficients for the sample quadruples used to develop the results on the right-hand side of Fig. 4.4. In all cases, it was found that all

four components are resolved at Δt_{max} if the noise level is decreased by a factor of 100. Since the signal to noise ratio is known to increase with the square of the number of scans [24], increasing the number of signals averaged from 8 per trial to 100^2 × 8 = 80,000 should recover acceptable resolution.

Another useful theoretical exercise considers the dependence of Δt_{max} on the density and amplitude of the time constants within a fixed range of values as summarized in Fig. 4.5. The graph in (a) displays four separate time constant amplitude envelope functions. These functions include a box or equal amplitude distribution across the 0.1 s to 1.0 s time range, a Gaussian distribution and two oppositely skewed, bimodal Gaussian distributions. These amplitude distributions were used to generate the respective plots of Δt_{max} as function of the density of relaxation coefficients in (b), or equivalently the number of relaxation coefficients # λ within the displayed fixed 0.1 s < T < 1 s range. The Δt_{max} values were obtained by maximizing Eq. (4.2) as a function of Δt and increasing number of relaxation coefficients. The Δt_{max} value for two relaxation coefficients is identical in all cases as the two time constants T_1 = 0.1 s and T_2 = 1 s yield R_1 = 10 Hz and R_2 = 1 Hz and $\Delta t_{max} = \log(R_2/R_1)/(R_2–R_1) = \log(10\text{ Hz}/1\text{ Hz})/(10\text{ Hz}–1\text{ Hz}) = 0.26$ s. As the number of relaxation coefficients increases, the Δt_{max} value steadily increases and asymptotically approaches a constant number that reflects the relaxation time distribution mean value. The similarity of the 0.35 s and 0.34 s asymptotic Δt_{max} values shown for the solid and dashed curves in Fig. 4.5b is expected as the corresponding time constant amplitude distributions shown in Fig. 4.5a are symmetric and have the same mean time constant value. As the shape of the distribution becomes bimodal in Fig. 4.5a, the asymptotic Δt_{max} value changes. The shift of average time constant to shorter T value for the dash-dotted curve in Fig. 4.5a causes the asymptotic Δt_{max} value to shorten to 0.32 s in Fig. 4.5b. The opposite effect is observed for the dotted curve in Fig. 4.5b. Here the asymptotic Δt_{max} value lengthens to 0.37 s as the average time constant shifts to longer T value in Fig. 4.5a. It should be clear that operation at Δt_{max} does not guarantee that all the relaxation coefficients will be resolved. For example, it is not possible to resolve the ca. 1,000 relaxation coefficients used to reach the Δt_{max} asymptotic limit. Rather, the asymptotic Δt_{max} values shown in Fig. 4.5 suggest the best sampling rate needed to extract the maximum number of relaxation coefficients

from the measured data provided enough signals have been averaged to keep the experimental noise level low and thus produce near zero N_T values.

4.5 Conclusion

The MPM is an algebraic way to analyze the damped, exponential, and transient signals common to all NMR relaxometry experiments. This work builds upon earlier results [18, 22] and demonstrates that the eigenvalues provided by MPM analysis z_m most faithfully reproduce the relaxation coefficients λ_m when the data sampling time Δt_{max} is chosen such that the sum of square λ_m differences SS_λ is maximum as a function of data acquisition sampling time Δt. The validity of Δt_{max} in sample collections contrived to simultaneously produce two, three, and four relaxation coefficients is demonstrated by comparison of experiment to theory via the N_T parameter shown in Eq. (4). The analysis of two relaxation coefficient samples is attractive because a tractable analytical solution for N_T is obtained to first order in the mean square noise $\langle N^2 \rangle$. In the case of Gaussian white noise, higher nth-order analytical corrections in terms of $\langle N^2 \rangle^n$ could be developed. But judging from the agreement between the analytical and numerical results in the vicinity of Δt_{max}, numerical methods were adopted as they also easily scale to situations presenting more than just two relaxation coefficients.

The obvious way to implement this work in the laboratory begins by obtaining a high signal–to–noise, oversampled transient relaxation decay signal. Oversampling guarantees that $\Delta t < \Delta t_{max}$. The number and the values of the relaxation time constants are estimated from this oversampled signal using conventional MPM, ILT, data fitting, etc. The m estimated time constants are used to construct the λ_m relaxation coefficients and SS_λ, the function that is maximized to yield Δt_{max}. The measured transient data is then resampled at Δt_{max} and MPM is used to find the inherent relaxation times and their relative contribution to the signal. If the actual number of time constants contributing to the signal is known, then the reduced MPM introduced here can be used in place of applying the MPM to the full resampled signal.

References

[1] Encyclopedia of NMR, R. K. Harris and R. E. Wasylishen (Eds.), 2012, John Wiley and Sons, Hoboken, NJ, USA.

[2] R.R. Ernst, G.B. Bodenhausen, A. Wokaun, *Principles of Nuclear Magnetic Resonance in One and Two Dimensions* (Oxford University Press, New York, USA, 1987)

[3] K. Wuthrich, *NMR of proteins and nucleic acids* (Wiley, New York, USA, 1986)

[4] N. Tjandra, A. Bax, Direct measurement of distance and angles in biomolecules by NMR in a dilute liquid crystalline medium. Science **278**, 1111–1114 (1997)

[5] M.R. Hansen, L. Mueller, A. Pardi, Tunable alignment of macromolecules by filamentous phage yields dipolar coupling interactions. Nat. Struct. Biol. **5**, 1065–1074 (1998)

[6] C.R. Sanders, Life during wartime: a personal recollection of the circa 1990 prestegard lab and its contributions to membrane biophysics. J. Membr. Biol. **252**, 541–548 (2019)

[7] H. Yu, S. Myoung, S. Ahn, Recent applications of benchtop nuclear magnetic resonance spectroscopy. Magnetochemistry **7**, 121–147 (2021)

[8] G. Eidmann, R. Savelsberg, P. Blumler, B. Blumich, The NMR mouse, a mobile universal surface explorer. J. Magn. Reson., Ser. A **122**, 104–109 (1996)

[9] A.E. Marble, I.V. Mastikhin, B.G. Colpitts, B.J. Balcom, A Compact permanent magnet array with a remote homogeneous field. J. Magn. Reson. **186**, 100–104 (2007)

[10] B. Blumich, *NMR Imaging of Materials* (Oxford University Press, Oxford, UK, 2000)

[11] L.I.L. Things, M.R.I. Through, R.S. Chaughule, S.S. Ranade (eds.), *Prism Publications* (Mumbai, India, 2006)

[12] E.J. Fordham, A. Sezginer, L.D. Hall, Imaging multiexponential relaxation in the (y, loge T1) plane, with application to clay filtration in rock Cores. J. Magn. Reson., Ser. A **113**, 139–150 (1995)

[13] Y. Song, L. Venkataramanan, L. Burcaw, Determining the resolution of laplace inversion spectrum. J. Chem. Phys. **122**, 104104 (2005)

[14] R. Bro, S.D. Jong, A fast non-negativity-constrained least squares algorithm. J. Chemom. **11**, 393–401 (1997)

[15] A.N. Tikhonov, V.Y. Arsenin, *Solutions of Ill-Posed Problems* (Wiley, New York, USA, 1977)

[16] A. Reci, A.J. Sederman, L.F. Gladden, Retaining both discrete and smooth features in 1D and 2D NMR relaxation and diffusion experiments. J. Magn. Reson. **284**, 39–47 (2017)

[17] B. Chencarek, M.S. Nascimento, A.M. Souza, R.S. Sarthour, B.C.C. Santos, M.D. Correia, I.S. Oliveira, Multi-exponential analysis of water NMR spin-spin relaxation in porosity/permeability controlled sintered glass. J. Magn. Reson. **50**, 211–225 (2019)

[18] S.N. Fricke, J.D. Seymour, M.D. Battistel, D.I. Freedberg, C.D. Eads, M.P. Augustine, Data Processing in NMR Relaxometry Using the Matrix Pencil. J. Magn. Reson. **313**, 106704 (2020)

[19] Y.Y. Lin, P. Hodgkinson, M. Ernst, A. Pines, A Novel detection-estimation scheme for noisy NMR signals: applications to delayed acquisition data. J. Magn. Reson. **128**, 30–41 (1997)

[20] R. Kumaresan and D. W. Tufts, Estimating the Parameters of Exponentially Damped Sinusoids and Pole-Zero Modeling in Noise, IEEE Trans. on Acoust, Speech, and Signal Process. ASSP-30 (6) (1982) 833–840.

[21] S. Jang, W. Choi, T.K. Sarkar, E.L. Mokole, Quantitative comparison between matrix Pencil method and state-space-based methods for radar object Identification. URSI Radio Science Bulletin **2005**(313), 27–38 (2005)

[22] D. Wortge, M. Parziale, J. Claussen, B. Mohebbi, S. Stapf, B. Blumich, M. Augustine, Quantitative stray-field T1 relaxometry with the matrix pencil method. J. Magn. Reson. **351**, 107435 (2023)

[23] S. Meiboom, D. Gill, Modified Spin-echo method for measuring nuclear relaxation times. Rev. Sci. Instrum. **29**, 688–691 (1958)

[24] E. Fukushima, S.B.W. Roeder, *Experimental Pulse NMR: A Nuts and Bolts Approach* (Addison-Wesley Publishing Company, Massachusetts, USA, 1981), pp 12–13

Chapter 5: Diffusion and Exchange in NMR

5.1 Introduction

The motion sensing abilities of NMR spectroscopy is not limited to merely relaxation rates. Adding to the impressive resume is the capability to detect diffusive and exchange motions [1]. Much of the important molecular dynamics and spatial information about a sample can be uncovered with the proper NMR pulse sequences. The effects of these motions were previously touched on in chapter 1 with respect to relaxation [2]. Here, a slightly deeper look at the role of diffusion and exchange are provided in order to provide extra context for the final chapter of this dissertation.

5.2 Diffusion

5.2.1 Fick's Laws

When discussing diffusion from a general chemistry and biology perspective, it is described as the translation of particles from a high density region to a lower density space. This behavior is described by Fick's first law,

$$\vec{J} = -D\vec{\nabla}\varphi \tag{5.1}$$

where $\vec{J}$ is the diffusive flux along each cartesian axis, D is the diffusion constant, $\nabla\varphi$ and represents the concentration gradient of the sample [3,4]. The diffusivity is tied to key information about the conditions of the given particle, including average translational energy and the intermolecular forces of the surrounding environment [5]. For liquids, this information can be cleanly summed up by the Stokes-Einstein relation [6].

$$D = \frac{k_B T}{6\pi\eta r} \tag{5.2}$$

Here, η is the viscosity, T is the temperature, and r is the radius of the particle. Usually, the particle is approximated to be spherical for simplicity. Under anisotropic conditions, D takes on the form of a tensor, however most liquid-state NMR situations are isotropic, and the diffusion coefficient is a scalar quantity.

One can now imagine that as time evolves, the concentration gradient changes due to the flux of particles. This is described by Fick's second law, also known as the diffusion equation:

$$\dot{\varphi} = D\nabla^2\varphi \tag{5.3}$$

Consider, a typical NMR sample in which no such commanding concentration gradient exists. As is evident by relaxation, some translation must still exist in the sample to incite local field fluctuations [2]. The motion is driven by collisions with surrounding particles and is thus random in nature. This phenomenon is called Brownian motion and its corresponding *D* is known as the self-diffusion coefficient [6]. For an isotropic solution, the displacement across all dimensions on average reduces to zero as any random process would. However, similar to the squares of fluctuating fields in relaxation, the squares of the displacement are non-zero. The self-diffusion coefficient reflects the rate of this squared displacement yielding valuable dynamic via

$$d_{rms} = \sqrt{2D\tau} \tag{5.4}$$

where d_{rms} is the root mean square displacement of a given particle and τ is the length of time travelled.

5.2.2 Bloch-Torrey Equations

To observe the effects of diffusion on magnetization, the classical equations of motion are reintroduced [7]. Naturally, as spins translate through a volume, so too must the respective magnetic moment. This diffusion of magnetization can consequently be modeled by Fick's second law:

$$\frac{\partial\vec{M}}{\partial t} = D\nabla^2\vec{M}, \tag{5.5}$$

where is the vector $[M_x, M_y, M_z]$. In combination with the influence of Zeeman and relaxation interactions, the total change in magnetization can be captured by

$$\frac{\partial\vec{M}}{\partial t} = \gamma\vec{M}\times\vec{B} + \boldsymbol{R}\cdot(\vec{M}-\vec{M}_{eq}) + D\nabla^2\vec{M} \tag{5.6}$$

where $\vec{M}_{eq}$ is the equilibrium magnetization, usually $M_z = M_0$, and $\boldsymbol{R}$ is a diagonal matrix of the relaxation rates,

$$\boldsymbol{R} = \begin{pmatrix} -\frac{1}{T_2} & 0 & 0 \\ 0 & -\frac{1}{T_2} & 0 \\ 0 & 0 & -\frac{1}{T_1} \end{pmatrix}. \tag{5.7}$$

This set of differential equations makes up the Bloch-Torrey equations [8].

Recall the previous discussion on the effects of inhomogeneity on spin-spin relaxation. In the absence of any magnetic field gradient, the field experienced by a spin at any location is equivalent. This means that the magnetization is invariant under translation of these spins. In contrast, diffusion in an inhomogeneous field will induce a change in precession rate of the magnetic moment based on the current position of the spin as a function of time [1,2]. This continuous movement introduces fluctuations which drive faster relaxation, thus further attenuating signals beyond the pure dephasing. By including a linear field gradient of strength *G* in the z-direction, the effect of diffusion can be calculated independently as

$$\frac{\partial \vec{M}}{\partial t} = -i\gamma G z \vec{M} + D\nabla^2 \vec{M}. \tag{5.8}$$

Solving Eq. 5.8 yields the following attenuation function,

$$A = e^{-\frac{1}{3}D\gamma^2 G^2 t^3} \tag{5.9}$$

In conjunction with the relaxation solution, the classical solution for an FID under the effects of diffusion is given by Eq. 5.10 [9].

$$M(t) = M_0 e^{-\frac{t}{T_2}} e^{-\frac{1}{3}D\gamma^2 G^2 t^3}. \tag{5.10}$$

5.2.3 Measuring Diffusion Coefficients

Since the debut of spin echoes, multiple methods of directly measuring diffusion coefficients with NMR have been considered [10]. The original Carr-Purcell method for studying diffusion coefficients utilizes the steady application of a known gradient magnetic field during a spin echo sequence [11,12]. An ideal spin echo refocuses all spins, but if an isochromat were to change in precession frequency at any point

during the process its dephasing may become irreversible. In most commercial systems, the amount of irreversible dephasing due to the static field inhomogeneity is negligible. With a stronger applied gradient, the effects of diffusion become more pronounced. By knowing G and T_2, the self-diffusion coefficient can be calculated from a train of spin echoes using Eq. 5.10.

The Carr-Purcell method serves as an effective technique; however, it is haunted by hardware limitations [10]. Molecules with smaller coefficients require stronger gradient fields to see any appreciable effects due to diffusion. An increase in inhomogeneity results in a broader range of transition frequencies as the degree of dephasing grows. If the gradient field becomes too strong, some spins may no longer be subjected to enough RF power for sufficient excitation. To account for this effect, the amplitude of the RF must be increased while simultaneously increasing the bandwidth of the receiver, the latter introducing extra noise to the signal.

To bypass the complications that arise from the Carr-Purcell method, Stejskal and Tanner demonstrated the use of pulsed field gradients in the place of a continuous field [13]. The first pulsed gradient is applied immediately after the π/2 RF pulse over a period of δ. During this time, all spins dephase according to their location and gradient strength [14]. As with the standard spin echo, a π pulse is applied to begin the refocusing process. A second gradient pulse is then applied to reverse the effects of the initial dephasing pulse to ensure total coherence. If a spin diffuses at any time between these gradient pulses, Δ, the phase accrued due to the second pulse may not fully counter the first pulse. Only a fraction of the spins will refocus as a consequence, thus attenuating the recorded signal. The Bloch-Torrey equations can be solved for each step of the Pulsed Gradient Spin Echo (PGSE) sequence to find the following equation for the signal:

$$M(\Delta, \delta, G) = M_0 e^{-D\gamma^2 G^2 \delta^2 \left(\Delta - \frac{\delta}{3}\right)} \tag{5.11}$$

In contrast to previously discussed pulse sequences, PGSE data is not generally gathered as a function of time. Further attenuating the signal, incrementing Δ and δ subjects spins to increasing relaxation influence at each step. Instead, the strength of the gradient pulse is varied to increase the amount of

dephasing while maintaining a constant echo time. The transient is Gaussian as a function of G, so typically the transient is treated as a function of G^2 in order to apply standard relaxometry data processing methods.

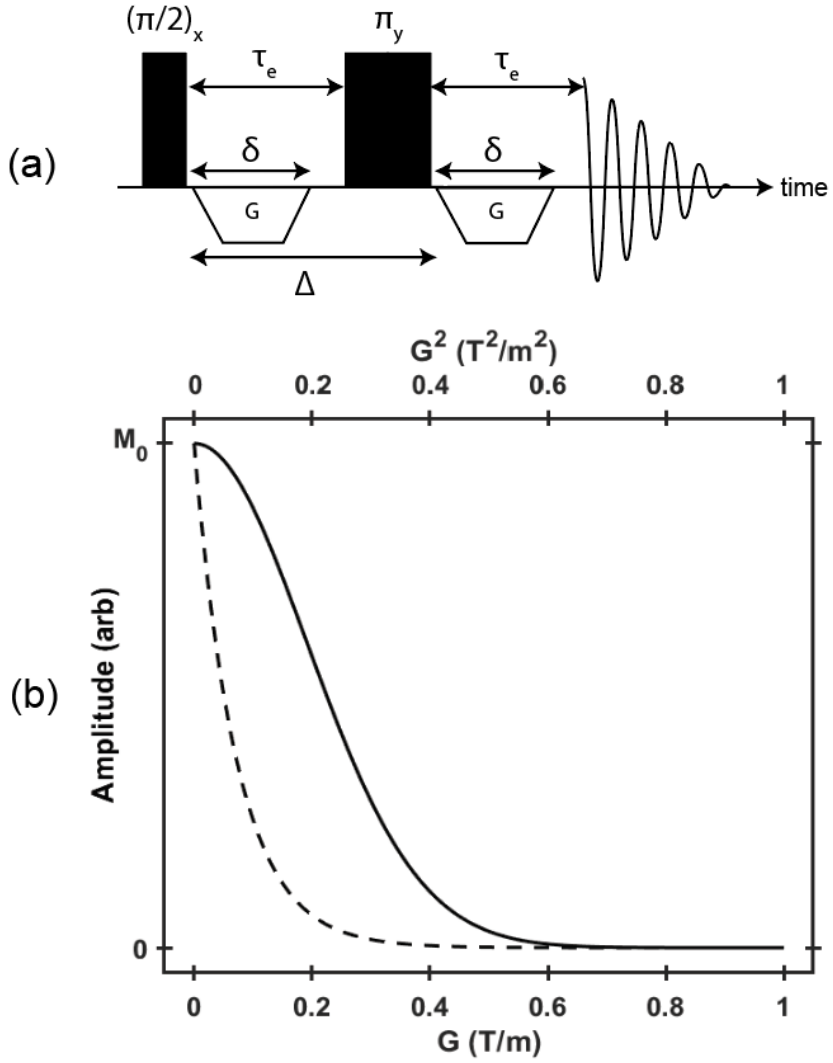

Figure 5.1. *The Pulsed Field Gradient Spin Echo sequence for measuring self-diffusion coefficients (a) and the corresponding transient (b) as a function of G (solid) and G^2 (dashed). This transient was calculated with $D = 2.3\times10^{-9} m^2/s$, $\delta = 7\times10^{-3}$ s, $\Delta = 7\times10^{-2}$ s, and $\gamma = 42.8$ MHz/T.*

5.2.4 Confinement

The path of molecules considered thus far have only been restricted by other molecules. In porous media and emulsions, often the motion of the molecules are further restricted by a barrier [15-19].

Traditionally, scattering and microscopy techniques have been used to measure the size of these pores and droplets. However, each of these methods tend to require some amount of sample interference to be sufficient. NMR diffusion experiments are being increasingly applied as noninvasive methods to measure these physical properties.

With significant restriction, the root mean square displacement of molecules is skewed as a consequence of more frequent collisions. As a result, the diffusivity measured from PGSE experiments is smaller than the true self-diffusion coefficient [17]. With knowledge of the correct D and an approximate boundary shape, one of several equations can be leveraged to determine the confinement radius. Generally, the cavities are assumed to be spherical attenuating the signal as

$$M(\Delta,\delta,G) = M_0 e^{-2\gamma^2 G^2 \sum_{m=1}^{\infty} \frac{1}{\alpha_m^2(\alpha_m^2 r^2 - 2)}\left[\frac{2\delta}{\alpha_m^2 D} - \frac{2+e^{-\alpha_m^2 D(\Delta-\delta)} - 2e^{-\alpha_m^2 D\Delta}}{(\alpha_m^2 D)^2} - \frac{2e^{-\alpha_m^2 D\delta} - e^{-\alpha_m^2 D(\Delta+\delta)}}{(\alpha_m^2 D)^2}\right]} \quad (5.12)$$

where r is the radius of the cavity and α_m corresponds to the roots of the Bessel function (J_n) relation

$$J_{3/2}(\alpha r) = \alpha r J_{5/2}(\alpha r). \quad (5.13)$$

Furthermore, often the size of these boundaries are not uniform throughout the sample, but rather a complex distribution. Currently, the primary mode of recovering these distributions of radii falls in the hands of inverse Laplace transforms.

5.3 Exchange

Another source of motion for nuclear spins comes through more reactionary means. Be it through intermolecular or intramolecular reactions, nuclei may find themselves positioned in new magnetic environments by a change in chemical bonding [20]. This process, known as chemical exchange, gives rise to both spectral and relaxation effects which promote the study of chemical kinetics in NMR. In contrast to more traditional kinetics experiments, NMR analysis of kinetics is not constrained to systems which are far from equilibrium. Due to the effects of nuclear shielding, NMR proves to be highly sensitive to any movement of spins between chemical environments. Even after dynamic equilibrium, chemical exchange can still be observed.

5.3.1 Two-Site Exchange

Consider a system with two chemical environments, A and B, in which the static field experienced by a spin occupying each site is different [1,20]. The resulting precession frequencies ω_A and ω_B serve an important role and the effects of exchange are discussed here in the form of chemical shift frequencies Ω_A and Ω_B. Two conditions exist for the following exchange between the sites:

$$A \underset{k_{BA}}{\overset{k_{AB}}{\rightleftharpoons}} B. \tag{5.14}$$

First, if the two environments possess an equal population, the forward (k_{AB}) and reverse (k_{BA}) rates of reaction are also equivalent. This situation is referred to as symmetric two site exchange.

The effects of exchange in NMR are tied to the relationship of the frequency of exchange with respect to the difference in chemical shifts $\Delta\Omega$ [20]. If exchange occurs at a rate much slower than $\Delta\Omega$, the system is in the regime of slow exchange. Hopping between sites induces a sudden change in precession frequency and thus induces dephasing amongst the spins. As the rate of exchange increases in the slow regime, the degree of dephasing increases yielding noticeable broadening of each spectral peak while retaining some features of the two peaks. This continues until the rate of exchange is in the ballpark of $\Delta\Omega$, a point at which all resolution is lost producing a significantly broad spectrum as depicted in Fig. 5.2(c). This is the intermediate exchange regime, and the maximum amount of dephasing across all spins is found when $k = \Delta\Omega/2$.

As the rate of exchange exceeds the intermediate regime, the phases begin to reconverge thus conversely narrowing the spectrum. This narrowing regime is the consequence of fast exchange [20]. With the rapid hopping, the spin response to the different environments blur thus resulting in an apparent average of precession frequencies. In the fast exchange regime, the spectrum collapses to one narrow peak as rate increases.

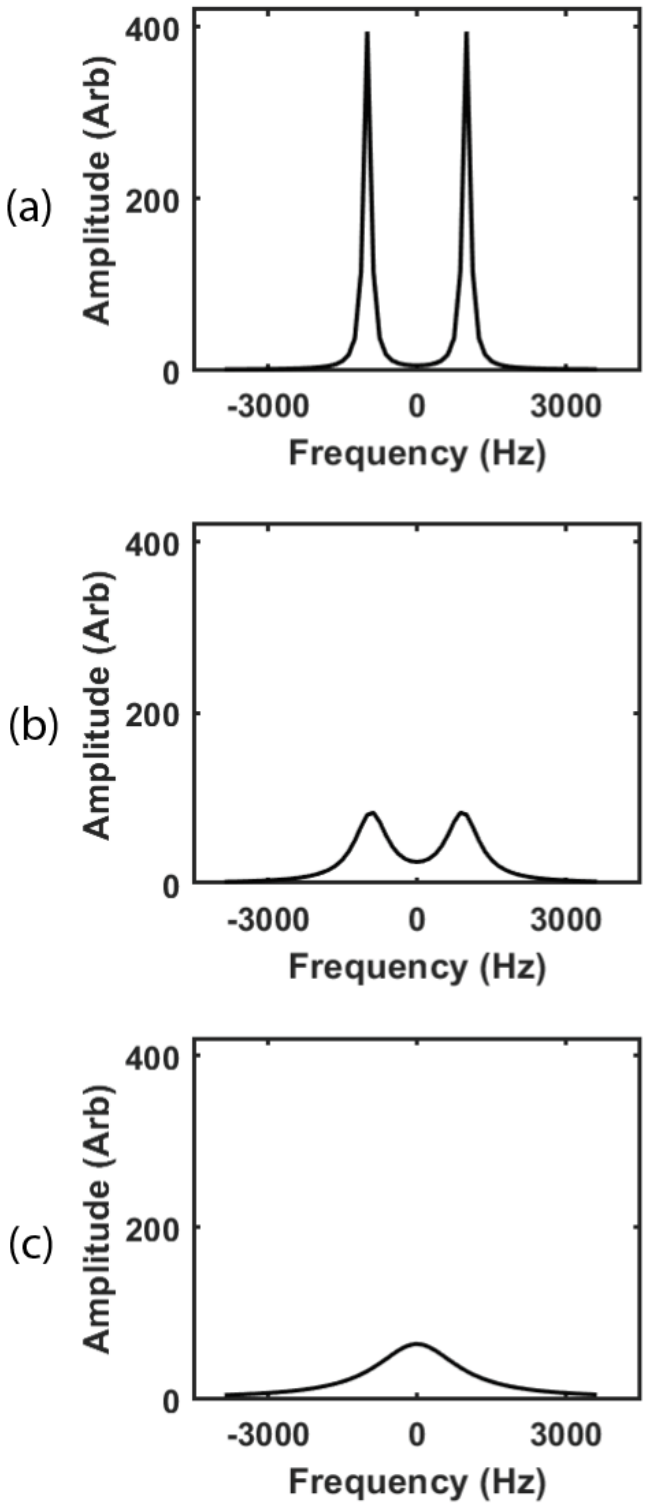

Figure 5.2. *The effects of slow exchange on NMR spectra. These spectra were simulated with $\Delta\Omega/2$ = 6300 Hz and exchange rates of k = 500 Hz (a), 2500 Hz (b), and 6300 Hz (c). As the exchange rate increases, the doublet collapses into a singlet.*

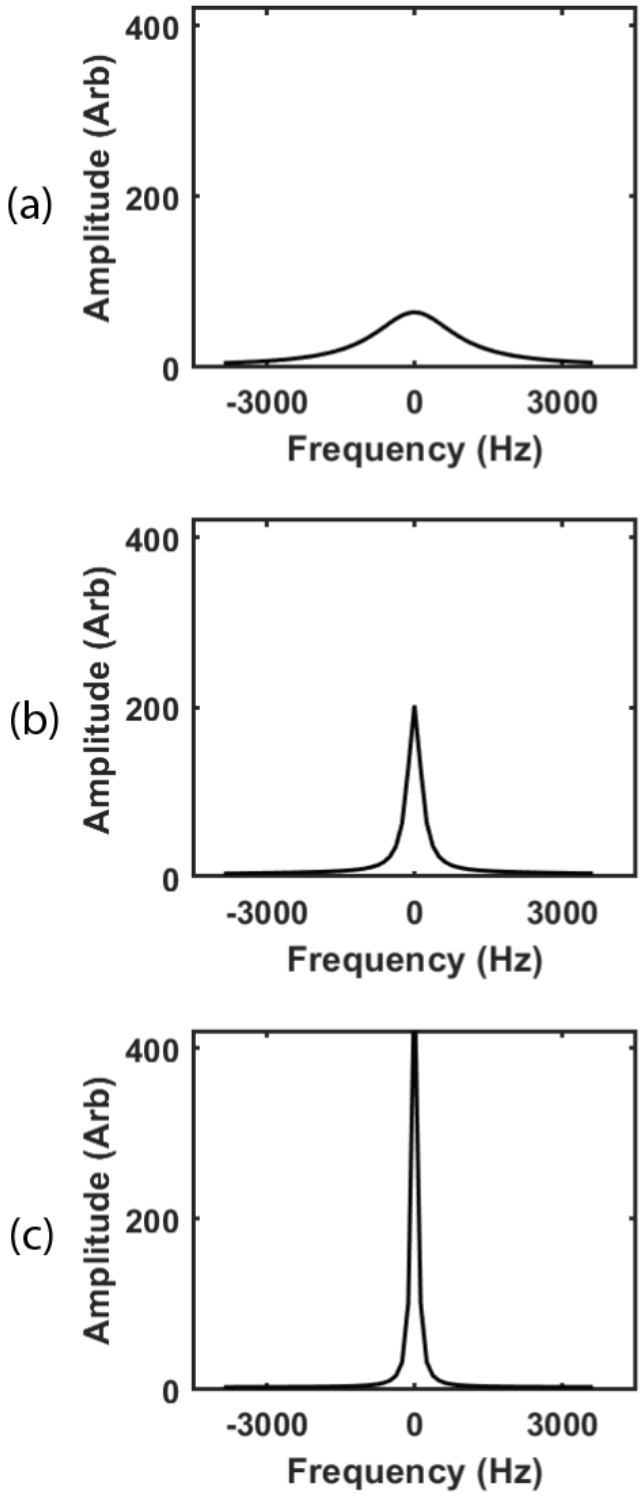

Figure 5.3. *The effects of fast exchange on NMR spectra. These spectra were simulated with $\Delta\Omega/2$ = 6300 Hz and exchange rates of k = 6300 Hz (a), 20000 Hz (b), and 50000 Hz (c). As the exchange rate increases, the singlet narrows.*

In the case where one site is heavily preferred over another, the rates of the forward and reverse reactions are governed by the equilibrium constant [20]. This is the most common condition for chemical reactions due to energetic and entropic barriers. Asymmetric two-site exchange experiences the same broadening and narrowing effects of the symmetric case. An additional distortion occurs due to the difference in populations in the form of weighted averaging of precession frequencies. Thus, in the fast exchange regime the narrowing peak shifts closer to the environmental frequency with a higher population. While the two-site exchange cases are deeply understood, systems of any higher complexity still hold some mysteries. Chapter 6 serves as an investigation of three-site relaxation in the realm of restricted diffusion.

5.3.2 Bloch-McConnell Equations

As with the other motions discussed so far, the classical equations of motion provide satisfactory models for magnetization behavior due to exchange. McConnell introduced a modified set of equations for the purpose of understanding two-site chemical exchange [21,22]. For the purpose of calculating the spectral effects, only the transverse magnetization will be considered, as denoted by $M^+ = M_x + iM_y$.

With two sites, two precession frequencies contribute to the overall signal based on their relative populations, P_A and P_B. In a matrix form, this will be represented as

$$\boldsymbol{L} = \begin{pmatrix} P_A\omega_A & 0 \\ 0 & P_B\omega_B \end{pmatrix}. \tag{5.15}$$

Considering only the effects of relaxation in the transverse plane, a matrix of the corresponding spin-spin relaxation rates is required,

$$\boldsymbol{R} = \begin{pmatrix} -\frac{1}{T_{2A}} & 0 \\ 0 & -\frac{1}{T_{2B}} \end{pmatrix}. \tag{5.16}$$

Barring exchange momentarily, the Bloch equations which describe the transverse magnetization for two sites is

$$\frac{d\vec{M}^+}{dt} = (i\boldsymbol{L} + \boldsymbol{R})\vec{M}^+ \tag{5.17}$$

where $\vec{M}^+$ is the vector $[M_A^+, M_B^+]$. To account for exchange processes, a matrix of kinetic rates is employed known as the exchange matrix $\boldsymbol{K}$.

$$\boldsymbol{K} = \begin{pmatrix} -k_{AB} & k_{BA} \\ k_{AB} & -k_{BA} \end{pmatrix} \tag{5.18}$$

Inserting $\boldsymbol{K}$ into the Bloch formalism yields the Bloch-McConnell equations:

$$\frac{d\vec{M}^+}{dt} = (i\boldsymbol{L} + \boldsymbol{R} + \boldsymbol{K})\vec{M}^+ \tag{5.19}$$

In contrast to the previous classical models, the exchange matrix introduces off-diagonal elements. The Bloch-McConnell equations require diagonalization of $i\boldsymbol{L} + \boldsymbol{R} + \boldsymbol{K}$ in order to solve for the magnetization at each site. The total signal for two magnetic sites undergoing exchange is given by

$$\vec{M}^+ = e^{\Lambda_A t} + e^{\Lambda_B t} \tag{5.20}$$

where Λ_A and Λ_B denote the eigenvalues for sites A and B respectively.

5.3.3 Measuring Exchange

As previously discussed, the narrowing and broadening of spectral lines is reflected in relaxometry measurements by changes in relaxation rates. These changes can be utilized for the experimental investigation of kinetic processes such as the folding of proteins. One of the simplest methods for exchange studies is the relaxation dispersion experiment [23]. Considering the standard CPMG pulse sequence, complete refocusing of spins following a π pulse requires that all spins maintain their precession frequency during evolution times τ_e. Any exchange that occurs between refocusing pulses ($2\tau_e$) will accrue additional dephasing that is not reversible thus decreasing the recorded signal. As a consequence, the CPMG signal damps faster.

If the rate of refocusing pulses $1/2\tau_e$, known as repetition rate ν, outpaces the exchange rate, the attenuation effect becomes minimized as spins refocus before noticeable amounts exchange is able to occur. Accordingly, if the repetition rate is too slow, spins are given ample time to exchange thus decreasing echo

amplitudes. The relaxation dispersion experiment explores this phenomenon by determining the apparent relaxation rate of several CPMG transient signals as a function of repetition rate. The exchange rates may then be recovered by fitting to the solutions outlined by Carver and Richards [25].

Another common experiment for looking at exchange in NMR is T_2-T_2 exchange which yields a map of the exchange processes [26]. Depicted in Fig. 5.5, this pulse sequence consists of two CPMG trains, occurring over periods of t_1 and t_2, separated by a mixing period τ_m which allows exchange to occur. Between the CPMG sequences, an additional π /2 pulse is introduced. A process known as magnetization storage is accomplished as the first $\pi/2$ pulse rotates any remaining transverse relaxation to the longitudinal direction. While the mechanisms of T_1 now drive relaxation towards thermal equilibrium, the magnetization along the static field is encoded with the original precession frequencies and populations of the spins. During this relaxation period, spins are allowed to exchange before being subjected to another CPMG pulse sequence which is detected.

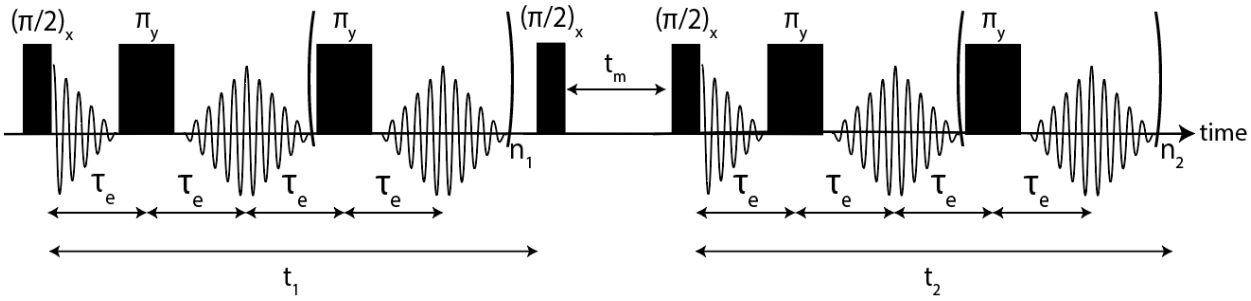

Figure 5.4. *The T_2-T_2 exchange pulse sequence for studying exchange. A CPMG with one repetition rate and overall experimental time, defined by $2n_1\tau_e$, is followed by a storage pulse, then another CPMG with different parameters.*

The T_2-T_2 exchange sequence is repeated for several values of t_1 while recording only the second CPMG as a function of t_2 yielding a two-dimensional data matrix which when inverted provides the exchange map. Note that is beneficial to increment t_1 in equally spaced intervals. If the exchange map displays off-diagonal peaks, exchange has occurred [26,27]. In conjunction with the solutions of the Bloch-

McConnell equations, the integrals of the exchange peaks can provide useful kinetic information. This experimental technique is the basis for the experimental discussions in Chapter 6.

References

[1] P. T. Callaghan, *Translational Dynamics and Magnetic Resonance: Principles of Pulsed Gradient Spin Echo NMR* (Oxford University Press, Oxford, UK, 2011)

[2] M. H. Levitt, *Spin Dynamics: Basics of Nuclear Magnetic Resonance* (John Wiley and Sons, West Sussex, UK, 2008)

[3] L. Zhou, K. Nyberg, A. C. Rowat, Understanding diffusion theory and Fick's law through food and cooking. Adv. Physiol. Educ. **94**, 192-197 (2015)

[4] A. Fick, Ueber Diffusion. Ann. Phys. **170**, 59-86 (1855)

[5] T. D. W. Claridge, *High Resolution NMR Techniques in Organic Chemistry, 2nd Ed.* (Elsevier, Oxford, UK, 2009)

[6] A. Einstein, Über die von der moleukularkinetischen Theorie der Wärme geforderte Bewegung von in ruhenden Flüssigkeiten suspendierten Teilchen. Ann. Phys. **322**, 549-560 (1905)

[7] F. Bloch, Nuclear induction, Phys. Rev. **70**, 460-474 (1946)

[8] H. C. Torrey, Bloch equations with diffusion terms. Phys. Rev. **104**, 563-565 (1956)

[9] V. M. Kenkre, E. Fukushima, D. Sheltraw, Simple solutions of the Torrey-Bloch equations in the NMR study of molecular diffusion. J. Magn. Reson. **128**, 62-69 (1997)

[10] E. Fukushima, S. B. W. Roeder, *Experimental Pulse NMR: A Nuts and Bolts Approach* (Addison-Wesley, Massachusetts, USA, 1981)

[11] E. L. Hahn, Spin echoes. Phys. Rev. **80**, 580-594 (1950)

[12] H. Y. Carr, E. M. Purcell, Effects of diffusion on free precession in nuclear magnetic resonance experiments. Phys. Rev. **94**, 630-638 (1954)

[13] E. O. Stejskal, J. E. Tanner, Spin diffusion measurements: Spin echoes in the presence of a time-dependent field gradient. J. Chem. Phys. **42**, 288-292 (1965)

[14] A. G. Anderson, R. L. Garwin, E. L. Hahn, J. W. Horton, G. L. Tucker, R. M. Walker, Spin echo serial storage memory. J. Appl. Phys. **26**, 1324-1338 (1955)

[15] A. T. Watson, C. T. P. Chang, Characterizing porous media with NMR methods. Prog. Nucl. Magn. Reson. Spectrosc. **31**, 343-386 (1997)

[16] M. L. Johns, K. G. Hollingsworth, Characterisation of emulsion systems using NMR and MRI. Prog. Nucl. Magn. Reson. Spectrosc. **50**, 51-70 (2007)

[17] K. J. Packer, C. Rees, Pulsed NMR studies of restricted diffusion: I. Droplet size distributions in emulsions. J. Colloid Interface Sci. **40**, 206-218 (1971)

[18] K. G. Hollingsworth, M. L. Johns, Measurement of emulsion droplet sizes using PFG NMR and regularization methods. J. Colloid Interface Sci. **258**, 383-389 (2003)

[19] J. S. Murday, R. M. Cotts, Self-diffusion coefficient of liquid lithium. J. Chem. Phys. **48**, 4938-4945 (1968)

[20] A. D. Bain, Chemical exchange in NMR. Prog. Nucl. Magn. Reson. Spectrosc. **43**, 61-103 (2003)

[21] H. M. McConnell, Reaction rates by nuclear magnetic resonance. J. Chem. Phys. **28**, 430-431 (1957)

[22] L. W. Reeves, K. N. Shaw, Nuclear magnetic resonance studies of multi-site chemical exchange. I. Matric formulation of the Bloch equations. Can. J. Chem. **48**, 3641-3653 (1970)

[23] P. Neudecker, P. Lundström, L. E. Kay, Relaxation dispersion NMR spectroscopy as a tool for detailed studies of protein folding. Biophys. J. **96**, 2045-2054 (2009)

[24] E. Walinda, D. Morimoto, K. Sugase, Overview of relaxation dispersion NMR spectroscopy to study protein dynamic and protein-ligand interactions. Curr. Protoc. Protein Sci. **92**, e57 (2018)

[25] J. P. Carver, R. E. Richards, A general two-site solution for the chemical exchange produced dependence of T_2 upon the Carr-Purcell pulse separation. J. Magn. Reson. **6**, 89-105 (1972)

[26] J. Jeener, B. H. Meier, P. Bachmann, R. R. Ernst, Investigation of exchange processes by two-dimensional NMR spectroscopy. J. Chem. Phys. **71**, 4546-4553 (1979)

[27] Y. Gao, B. Blümich, Analysis of three-site *T2-T2* exchange NMR. J. Magn. Reson. **315**, 106740 (2020)

Chapter 6: Asymmetry in Three-Site Relaxation Exchange NMR

Abstract

The asymmetry of peak integrals in 2D relaxation maps of exchange between three sites indicates circular flow between the relaxation sites. This disagrees with the detailed balance according to which the exchange between any pair of sites must be balanced in terms of thermodynamic equilibrium. Confined diffusion of particles jumping randomly on a 2D checkerboard grid to any of their eight neighbor positions and confined gas diffusion were modeled in Monte Carlo simulations to explore the impact of topological constraints on particle exchange between three pools. Both models produce density variations across the pore and reveal that up to 1% of the molecules move in circular paths between the relaxation pools. This motion is driven by different features of algorithm. It is silent in terms of thermodynamic equilibrium, confirming that multi-site exchange maps are symmetric in this case. The coherent flux is argued to result from stochastic pore resonance related to diffusion eigenmodes. If it can be driven experimentally by external time-varying electric, magnetic, or ultrasonic fields, this may be a way to enhance heterogeneous catalysis.

6.1 Introduction

Exchange is an essential ingredient of diffusion and spreading phenomena, which are abundant in nature and govern the evolution of tangible and intangible objects and goods [1], as well as the physics of living systems [2,3]. Nuclear magnetic resonance (NMR) provides particularly powerful methodologies to investigate molecular exchange processes [4,5]. Slow molecular exchange on the timescale of milliseconds is studied by e.g., two-dimensional exchange NMR, i.e., by chemical exchange spectroscopy for rotational motion [6] and by exchange relaxometry for translational motion [7]. In equilibrium, the nature of the exchange processes is commonly understood to be random Brownian motion, and the associated 2D NMR exchange maps are expected to be symmetric with respect to their diagonal. On the other hand, exchange

in non-equilibrium leads to asymmetry. This has been observed in NMR, for example, in 2D chemical exchange spectra for chemical reactions involving different sites [8], for the spread of hyperpolarization by spin diffusion [9], for slow flow across porous media in relaxation exchange maps [10], and in position and velocity exchange NMR [11].

The kinetics of transitions or exchange between discrete states driven by random processes are described by van Kampen [12] as follows:

$$\frac{dM_i(t)}{dt} = \sum_j \{k_{ij}M_j(t) - k_{ji}M_i(t)\}, \tag{6.1}$$

where M_i refers to populations represented in NMR by magnetization components collected in the vector $\vec{M}$, and k_{ij} refers to the exchange rates equivalent to the transition probabilities from state j to state i, which are collected in the kinetic exchange matrix $\boldsymbol{k}$. In equilibrium,

$$\frac{dM_i(t)}{dt} = 0, \tag{5.2}$$

and the number of all particles arriving at site i from sites j is equal to the number of all particles leaving from site i to sites j so that the total mass is conserved.

As a result of mass balance, two-site exchange between states or sites A and B always leads to symmetric 2D NMR exchange maps in thermodynamic equilibrium as the number $k_{BA}M_A$ of particles populating site B by leaving site A per unit of time is equal to the number of particles $k_{AB}M_B$ leaving site B and populating site A per unit of time. This number is the product of the rate k_{BA} for transitions from site A to site B times the population M_A of site A. The relationship $k_{BA}M_A = k_{AB}M_B$ is known as the principle of detailed balance. In thermal equilibrium, it is understood to also apply to rate processes involving more than two sites [2,13].

As an example of mass-balanced equilibrium diffusion between three sites [13,14], Eq. (6.2) becomes

$$\begin{aligned} k_{21}M_1 + k_{31}M_1 &= k_{12}M_2 + k_{13}M_3 \\ k_{12}M_2 + k_{32}M_2 &= k_{21}M_1 + k_{23}M_3 \\ k_{13}M_3 + k_{23}M_3 &= k_{31}M_1 + k_{32}M_2, \end{aligned} \tag{6.3}$$

or equivalently, mass balance requires

$$k_{31}M_1 - k_{13}M_3 = k_{12}M_2 - k_{21}M_1 = k_{23}M_3 - k_{32}M_2. \quad (6.4)$$

Normalization of this expression to the total number of exchanges per unit of time defines the asymmetry parameter a_{sy} used below:

$$(k_{23}M_3 - k_{32}M_2)/\left[(1,1,1)\boldsymbol{k}\vec{M}\right]$$

Here, $k_{ij}M_j$ is the number of transitions from pool j to pool i, corresponding to the peak integral in an exchange map after correction for relaxation effects so that the denominator corresponds to the integral over all peaks. The asymmetry parameter thus quantifies the imbalance of exchange between two sites in terms of the number of unbalanced exchanges normalized to the total number of exchanges. Therefore, it specifies the relative flux in the circular exchange process. While mass balance (Eq. 6.4) is a necessary condition for dynamic equilibrium, detailed balance, on the other hand, is a stronger condition applicable to thermodynamic equilibrium. It requires the following:

$$a_{sy} = 0. \quad (6.6)$$

Detailed balance was introduced by Maxwell in 1867 based on sufficient reason in his derivation of the speed distribution of gas atoms considering the speed exchange between colliding gas atoms in thermodynamic equilibrium [15]. An intriguing consequence of the exchange being balanced in detail between particles A and B amounts to the impossibility of assigning positive time to either velocity exchange from A to B or from B to A on the particle scale of the exchange process, thus admitting negative time or time reversal. In 1872, Boltzmann showed, in an elaborate treatment, that Maxwell's speed distribution also applies to polyatomic gas molecules [16]. Furthermore, in 1917, Einstein derived Planck's law of blackbody radiation as a balanced energy exchange between quantized radiation and matter, underlining the striking similarity to Maxwell's speed distribution of gas atoms [17]. He concludes "Indem Energie und Impuls aufs engste miteinander verknüpft sind, kann deshalb eine Theorie erst dann als berechtigt angesehen werden, wenn gezeigt ist, daß die nach ihr von der Strahlung auf die Materie übertragenen Impulse zu solchen Bewegungen führen, wie sie die Wärmetheorie verlangt" [Since energy

and momentum are intimately connected, a theory can only then be considered justified when it has been shown that according to it the momenta of the radiation transferred to the matter lead to such motions as demanded by the theory of heat].

In his work extending Maxwell's speed distribution to polyatomic gas molecules, Boltzmann considered molecules in a container whereby the walls reflected the molecules like elastic balls: "Bezüglich der Gefäßwände, welche das Gas umschließen, will ich jedoch voraussetzen, dass die Moleküle an denselben wie elastische Kugeln reflektiert werden. . . . Die Wände stören nicht, da an ihnen die Moleküle wie elastische Kugeln reflektiert werden; also geradeso von ihnen zurücktreten, als ob der Raum jenseits der Wände von gleich beschaffenem Gase erfüllt wäre" [Concerning the container walls which enclose the gas, I want to presume that the molecules are reflected from them like elastic balls. . . . The walls do not interfere because the molecules are reflected from them like elastic balls; that is, they recede from them just like that, as if the space beyond the walls would be filled with similarly conditioned gas]. Moreover, the interaction between gas molecules can be of any type. While Boltzmann states that any other interaction between walls and molecules leads to the same result, albeit at the loss of simplicity, the perfectly elastic reflections of the gas molecules at the walls eliminate the topological constraints of the box on their motion. For confined particles, this means that the pressure across the pore volume is constant; i.e., the time average of the particle density does not vary with the location inside the pore. Boltzmann obtained the same speed distribution for polyatomic molecules with internal degrees of freedom as Maxwell did for atoms based on a detailed balance of speed exchange. In the simulations reported below, the motion of molecules is considered whereby the interactions with the walls are the same as those among the molecules. Understanding confined diffusion [18] is important from a general point of view because the motion of molecules without topological constraints is an ideal limit which cannot be perfectly realized in practice, although it may be realized within experimental uncertainty.

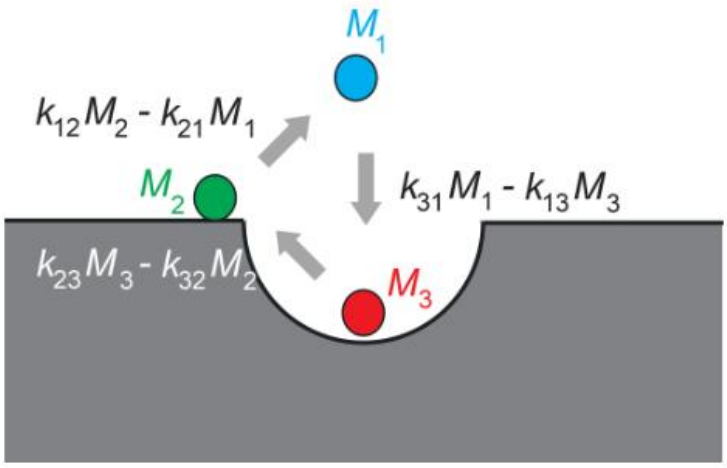

Figure 6.1. *Asymmetry in three-site diffusion-mediated exchange indicates coherent circular motion in a model example of water molecules in contact with a porous surface. Three water populations M_j are identified by different NMR relaxation times and colors They are molecules in the bulk (1), molecules on the surface (2), and molecules in the pores (3). The exchange rate constants are k_{ji} . The net particle flux $k_{ij}Mj - k_{ji}M_i$ between two sites differs from zero. The net mass of all molecules participating in the exchange is conserved. The figure illustrates positive a_{sy}.*

Two-site exchange processes will always be symmetric in equilibrium. This situation has been evaluated analytically for NMR relaxation exchange of fluids in porous media [19]. Yet, multi-site relaxation exchange NMR maps [20] can formally be asymmetric in equilibrium. For example, the transverse magnetization $s(t_1,t_2)$ from a three-site $T_2 - T_2$ relaxation exchange NMR experiment [21],

$$s(t_1, t_2) = (1,1,1)e^{-(\boldsymbol{R}_2+\boldsymbol{k})t_2}e^{-(\boldsymbol{R}_2+\boldsymbol{k})t_m}e^{-(\boldsymbol{R}_2+\boldsymbol{k})t_1}\vec{M}(t_0), \tag{6.7}$$

has been simulated to model an experimentally observed asymmetric three-site $T_2 - T_2$ NMR exchange map of water molecules saturating Al_2O_3 powder, with the three relaxation sites corresponding to bulk water, water molecules on the surface of the powder particles, and water molecules inside the surface pores (Fig. 6.1). Here, $\vec{M}(t_0)$ is the initial vector of transverse-magnetization components from relaxation sites 1, 2, and 3 generated from longitudinal thermodynamic equilibrium magnetization with a 90° pulse at the beginning of the experiment at time t_0, and t_1, t_m, and t_2 are the evolution, mixing, and detection time

intervals of the 2D NMR experiment, respectively [5,7]. Apart from the relaxation rate matrices $\boldsymbol{R}_1$ and $\boldsymbol{R}_2$ and the kinetic matrix $\boldsymbol{k}$, the best match obtained by forward simulation returned the peak integrals, revealing an asymmetry parameter of $a_{sy} = -1.2\%$. This asymmetry of the forward and backward particle jumps between two sites specifies the relative circular flux between the three sites (Fig. 6.1).

The asymmetry observed in the experiment can be argued to result from the uncertainty of the measurement and the data processing by 2D inverse Laplace transformation [22]. Also, asymmetric three-site exchange disagrees with the detailed balance of the exchange between any pair of sites in thermodynamic equilibrium because it needs to be explained by circular diffusion on the pore scale, and such motion resembles that of a rachet, which Feynman has argued disagrees with the second law of thermodynamics [23]. Nevertheless, Monte Carlo simulations were executed and are discussed below to investigate asymmetry in three-site exchange.

6.2 Modeling Confined Diffusion

6.2.1 Vacancy Diffusion: Random Particle Jumps on a 2D Checkerboard

Random jumps of particles from occupied sites to vacant sites were simulated with a Monte Carlo algorithm [24-27] in a confined space on a checkerboard. The algorithm models vacancy diffusion [28] encountered in metals and alloys, but the particles perform the jumps rather than the vacancies. To keep the simulation simple, it is limited to jumps on a 2D 3×3 Moore lattice of range 1 [29] following the rules of the game of life [29,30]. Here, the center particle can jump to any of its eight neighbors (Fig. 6.2). Different neighborhoods of range 1 were tested (Fig. S1 in the Supplement) [30], but only the Moore neighborhood, having the highest symmetry of all neighborhoods, produced data consistent with Eq. (6.4). Topological constraints were introduced, setting boundaries for the jump space. Initially, the available cells inside the jump space on the grid were populated randomly with particles up to a specified particle density. Particles in the bulk are indexed as 1, and two distinct boundary sections are indexed as 2 and 3, giving three environments for the particles to be exposed to and between which randomly selected particles can move.

A particle jumping from environment *j* to *i* is counted by incrementing the element *ij* of a 3×3 jump matrix with elements $k_{ij}M_j$ by 1. If the particle environment does not change with the jump, the respective diagonal element $k_{jj}M_j$ is incremented. The NMR relaxation environments are indexed according to increasing relaxation rate. If a particle is in contact with two different relaxation environments, it is assigned to the relaxation environment with the higher index according to the higher relaxation rate.

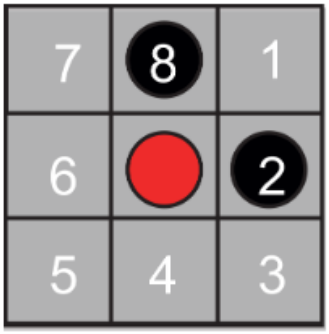

Figure 6.2. *Jumps on a checkerboard grid modeling vacancy diffusion. The center particle can jump to any of its eight nearest neighbor cells, which are numbered clockwise from 1 to 8. Jump probabilities were introduced to account for particle interaction between the center particle (red) and neighboring particles (black).*

Different rules governing jumps to a neighbor cell were explored. (1) In the simplest case, one of the eight destination cells was chosen at random without assigning a jump probability. When the destination cell was free, the jump was executed, and the initial and final environments were compared to increment the corresponding entry in the jump matrix accordingly. When the destination cell was occupied, the particle remained at its source cell, and the respective diagonal element of the jump matrix was incremented. In all other cases, jump probabilities were assigned. (2) As a subtle variant of the random jumps to any of the eight neighbor cells, jumps to any of the free neighbor cells were randomly selected by assigning zero jump probability to occupied neighbor cells and equal probability for jumps to the empty cells. This algorithm is known to violate detailed balance [24,31]. (3)With reference to the Helmholtz free energy $A = U - TS$, where U is internal energy, T is temperature, and S is entropy, a jump probability $p = \exp\left\{-\frac{\Delta A}{k_B T}\right\}$ was

introduced, where $\Delta A = U - T\Delta S$, T is the temperature, and k_B is the Boltzmann constant. $\Delta U = -\vec{F}\Delta\vec{R}$ and ΔS were estimated from the sum of distances to free or occupied neighbor cells by crude empirical models, as detailed in the supporting information. Here, $\vec{F}$ is the force, and $\Delta\vec{R}$ is the distance vector between two particles. This allowed us to probe attractive and repulsive interactions by changing the sign of ΔU in simulation runs and by varying the temperature in addition to varying population density equivalent to pressure. It is noted here that the force field on a randomly populated lattice is not conservative [31]. In other words, the energy balance of a particle moving in a circle is different from zero, and Monte Carlo simulations under these constraints probe a driven equilibrium and not the thermodynamic equilibrium [32].

The vacancy diffusion simulations were carried out with a program written in MATLAB R2020a by MathWorks on an Apple MacBook Pro 2.4 GHz with an Intel Quad-Core i5 processor. Unless indicated otherwise, 10^7 jumps were simulated in one run as taking 75 s.

6.2.2 Gas Diffusion

The gas diffusion calculations explore similar pore sizes and occupancy. Here, the motion of circular particles with diameters equal to the cell size was accomplished by propagating an initial distribution of particle speeds for random initial positions and directions in a Monte Carlo fashion based on instantaneous collisional forces. This distribution rapidly equilibrated to a Maxwell–Boltzmann distribution. Whereas in vacancy diffusion simulations the distribution of particles in the pore is recorded after each jump, it is recorded in the gas-phase simulations at constant time intervals. If the center of each particle was within one diameter of another, the particles are considered to have collided. Immediately after a collision, the projection of the velocity vector along the collision axis is reversed prior to propagating to the next step. In this approach, the observation time interval must be sufficiently small so that the new velocities are calculated with a small position uncertainty for the colliding particles [30,31].

The collisions change both the direction and velocity of the particles at each of the 10^9 constant time increments used here. Following conservation of momentum and kinetic energy,

$$\vec{v}_{1,new} = \vec{v}_{1,old} - \frac{2m_2}{(m_1+m_2)} \frac{\langle \vec{v}_{1,old} - \vec{v}_{2,old}, \vec{x}_1 - \vec{x}_2 \rangle}{\|\vec{x}_2 - \vec{x}_1\|^2} (\vec{x}_1 - \vec{x}_2), \tag{6.8}$$

$$\vec{v}_{2,new} = \vec{v}_{2,old} - \frac{2m_1}{(m_1+m_2)} \frac{\langle \vec{v}_{2,old} - \vec{v}_{1,old}, \vec{x}_2 - \vec{x}_1 \rangle}{\|\vec{x}_2 - \vec{x}_1\|^2} (\vec{x}_2 - \vec{x}_1). \tag{6.9}$$

These collisions with other particles and the wall are mediated by the particle size, which is set to be a fraction of the pore-side length of one. This means that a square pore with a five-particle diameter side length is populated with particles that have a diameter of one-fifth. To compare the continuous positional output of this model to vacancy diffusion, a two dimensional square grid with cell size set by the particle diameter is imposed on the entire pore. The quasi-continuous positional output is then binned into these cells and compared to the binned positions from the previous observation to determine if particles translated between the main pore volume, the pore wall, and the active site. The translational information is used to assign estimates of the jump matrix elements and thus the asymmetry parameter asy.

The gas diffusion simulations were carried out with a program written in MATLAB R2020a by MathWorks Inc. on a home-built desktop computer possessing an AMD (Advanced Micro Devices) Ryzen 7 2700 processor. In most cases, 10^9 jumps were simulated in one run, taking roughly 45 h to complete.

6.3 Results

Two different pore geometries were analyzed. Initially, the simulation was executed for a pore geometry (Fig. 6.3a) which approximated the surface structure of Fig. 6.1 and which is hypothesized to explain the observed asymmetry of water diffusing in a porous Al_2O_3 grain pack [21]. The dented surface was mirrored horizontally to double the probability of particles entering the dent (relaxation site 3) in the otherwise straight surface (relaxation site 2). The bulk of the particles defines relaxation site 1. Periodic boundary conditions were employed to the right and left. A pore boundary was treated just like an occupied cell, with the same rules applying to the jump probability. The simulations of particle motion confined to this complex pore structure and constrained by jump probabilities revealed the existence of asymmetric exchange. To understand the essence of the asymmetry, the pore geometry was simplified to a square with

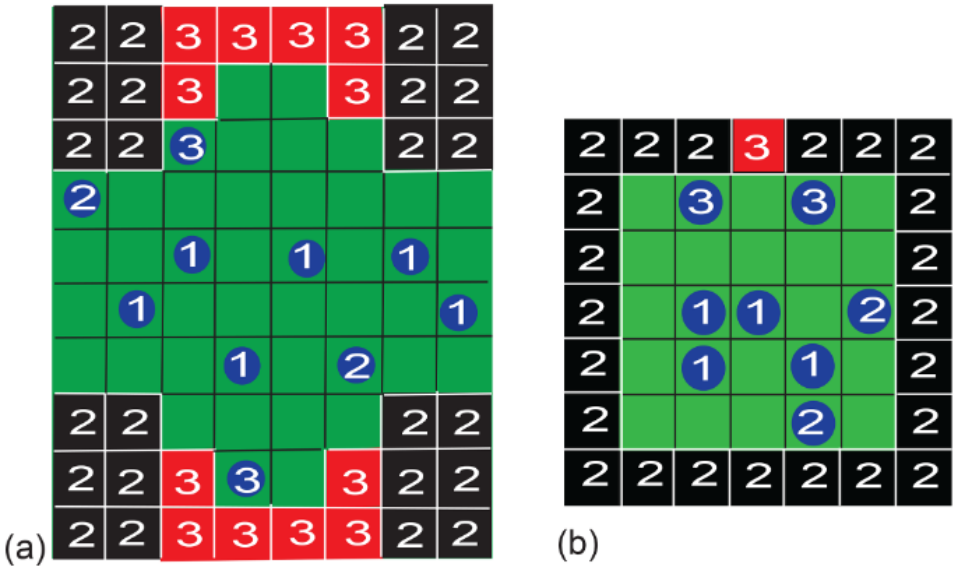

Figure 6.3. *Examples of pore models for two-dimensional three-site exchange based on a checkerboard grid. Particles can occupy one cell and jump to a neighboring one following different realizations of the jump probability. (a) Porous solid. The boundaries to the right and left are periodic. The boundaries at the top and bottom are rigid. Depending on their next neighbors in the first coordination shell, the particle relaxation environments are identified as bulk (1), surface (2), and pore (3), with increasing relaxation rates. (b) Small square pore with an active site. The bulk (1), the walls (2), and the active site (3) have different relaxation properties. If a particle is in contact with two different relaxation sites, it is counted as belonging to the particle pool with the larger relaxation rate, i.e., the pool with the higher number.*

an active site in the wall to study particle motion in detail. Particles in the bulk, in contact with the walls, and in contact with the active site are identified by different NMR relaxation properties (Fig. 6.3b). Enabled by the interaction model, which, depending on the particle environment assigns different jump probabilities as a function of temperature, the asymmetry parameter asy was evaluated for both pores with the vacancy diffusion algorithm as a function of temperature T and pressure P. Pressure was varied in terms of the population density, measured as the fraction of cells occupied in the pore. The results for the complex pore are reported in the Supplement (Fig. S3), whereas those for the simple square pore are reported here in the main text (Fig. 6.4). At certain temperatures and pressures, the autocorrelation function of the

occupation-time track of a particular cell and its Fourier transform were also determined. Striking features observed in vacancy diffusion were subsequently modeled with the gas diffusion algorithm in the square pore.

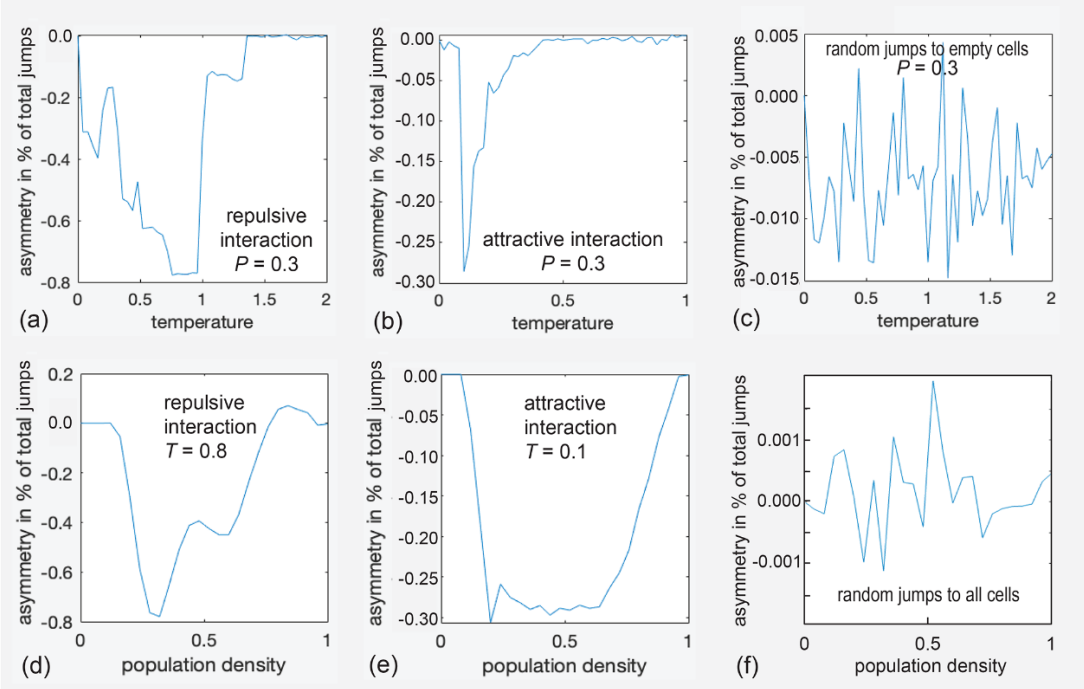

Figure 6.4. *Asymmetry parameters a_{sy} for diffusion inside the small rectangular pore depicted in Fig. 6.3b as a function of temperature T (a–c) and pressure P (d–f). (a) a_{sy}(T) for repulsive interaction at P = 0.3. (b) a_{sy} (T) for attractive interaction at P = 0.3. (c) a_{sy} (T) for jumps to randomly selected empty cells. (d) a_{sy} (P) for attractive interaction at T = 0.8. (e) a_{sy} (P) for attractive interaction at T = 0.1. (f) a_{sy} (P) for jumps to cells randomly selected from all eight neighbor cells.*

Relevant results for the square pore (Fig. 6.3b) are summarized in six graphs in Fig. 6.4. The asymmetry parameter varies strongly with temperature *T* (Fig. 6.4a, b) and pressure corresponding to population density *P* (Fig. 6.4d, e). All parameters are relative quantities without units. The top three graphs, namely (a), (b), and (c), show the variation of a_{sy} with temperature for a population fraction of 0.3, corresponding to that of a gas. The asymmetry parameter assumes only negative values in an abrupt but

reproducible manner in the range of $-0.8\% < a_{sy} < 0.0\%$ for repulsive interaction (Fig. 6.4a), i.e., for the definition of the force between particles as illustrated in Fig. S2a. With reference to Fig. 6.1, negative asy reports that the straight exit route from the active site towards the center of the pore is preferred over the detour via the pore wall. When the interaction is changed from repulsive to attractive by inverting the sign of ΔU in the expression for the free energy, the asymmetry parameter varies as well, though only between $-0.3\% < a_{sy} < 0.0\%$ (Fig. 6.4b). In either case, the asymmetry parameter varies with temperature and pressure. It is concluded that, for this small pore, up to about 1% of all jumps on the checkerboard can proceed in an ordered circular fashion between the three sites. Similar behavior is observed for the complex pore of Fig. 6.3a, as illustrated in Fig. S3 in the Supplement.

At the extrema of the $a_{sy}(T)$ curves in Fig. 4a and b, the dependence of the asymmetry parameters on population density was investigated (Fig. 6.4d, e). The variations with population density are smoother than those with temperature. Significant negative asymmetry results at intermediate pressures, while at low and high pressures, the asymmetry is small (Fig. 6.4d, e). At higher temperatures and high pressures, small positive asy is observed (Fig. 6.4d, T = 0:8, P = 0:8). If the destination cell for a jump is chosen at random without considering a hypothetical free-jump energy A, then essentially, noise more than 2 orders of magnitude smaller is observed for the exchange asymmetry determined from 10^7 jumps when varying T and P (Fig. 6.4c, f). However, a small bias towards negative asy results if the destination cell is chosen at random from all free neighbor cells (Fig. 6.4c), whereas no bias is detected if the destination cell is chosen at random from all neighbor cells, whether free or occupied (Fig. 6.4f). This difference becomes more pronounced at a higher number of jumps (see below).

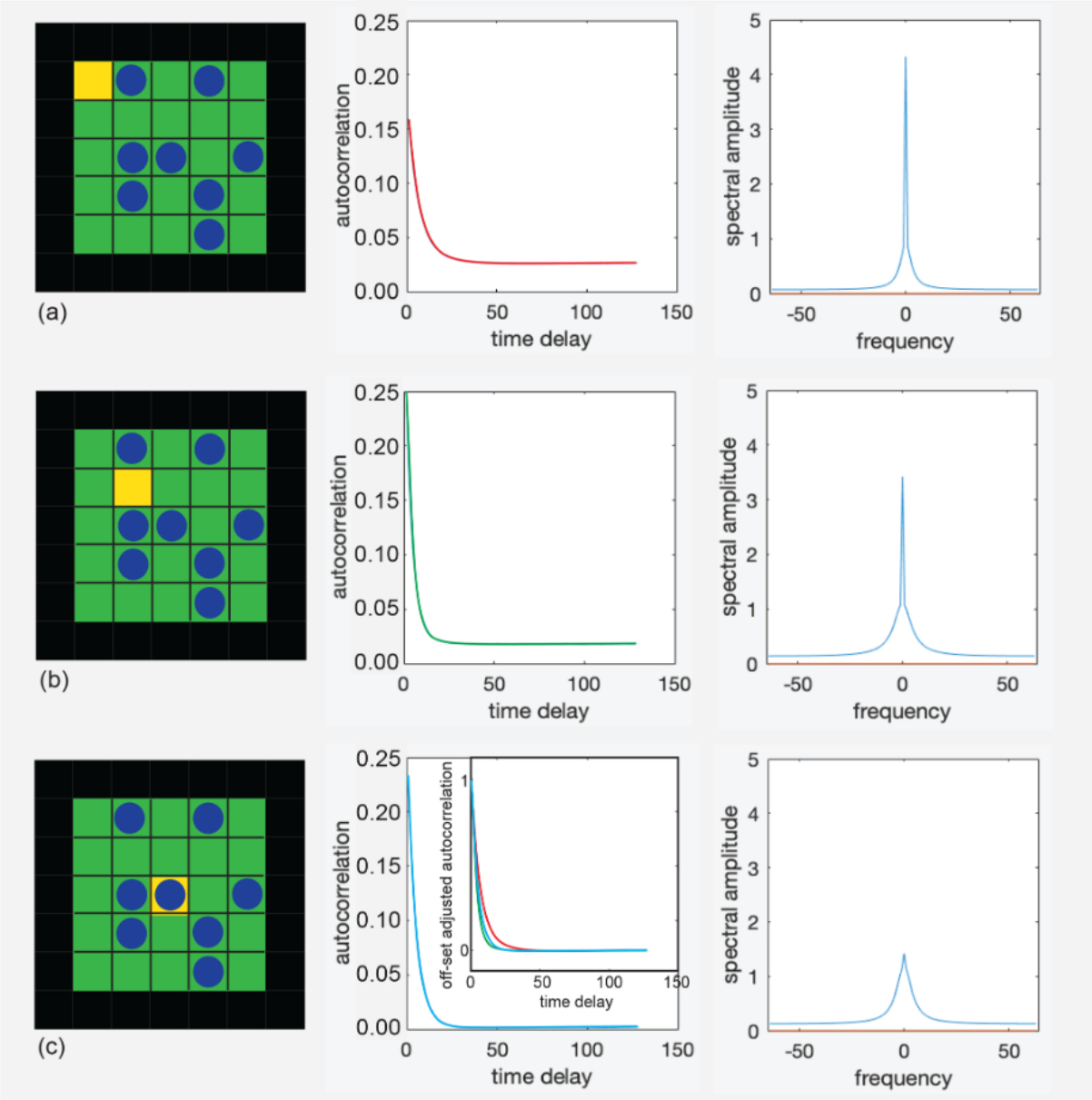

Figure 6.5. *Autocorrelation functions (center) of the occupancy of the yellow cells (left) and the real parts of their Fourier transforms (right) for repulsive interaction at T = 0.1 and P = 0.3. (a) Corner cell. (b) Off-center cell. (c) Center cell. The inset in the middle compares the decays of all three autocorrelation functions after subtraction of the offsets.*

To shed further light on the origin of the asymmetry, autocorrelation functions of the occupation-time tracks of selected cells in the pore were computed and Fourier transformed (Fig. 6.5). The occupation-time track was calibrated to zero mean for purely random occupation; i.e., it contained the negative

population density when it was empty and the complement of the population density to 1 when the cell was occupied. The faster the autocorrelation function decayed, the less coherently the cell population fluctuated and the broader its Fourier transform was, i.e., the transfer function (Fig. 6.5b, c). A constant offset of the autocorrelation function shows that the time-average population in the cell differs from the mean population of the pore (Fig. 6.5a, b). This offset produces a spike at zero frequency in the transfer functions. Subtracting the offsets from the autocorrelation functions and scaling the resulting functions to the same amplitude reveals different decays in different cells and thus variations in particle dynamics across the pore (inset in Fig. 6.5c, middle). These dynamics cannot readily be measured for a single cell in the pore, although an average over all cells and pores in the measurement volume would be amenable to experimentation by probing the particle dynamics with CPMG (Carr, Purcell, Meiboom, and Gill) measurements in magnetic gradient fields at variable echo times. Such measurements provide the frequency-dependent diffusion coefficient in terms of the Fourier transform of the velocity autocorrelation function [33-35].

While the autocorrelation function is difficult to probe experimentally, the asymmetry parameter asy, on the other hand, probes the particle dynamics and could be investigated experimentally directly by relaxation exchange NMR experiments provided the signal-to-noise ratio is good enough. The parameter depends on the location of the relaxation center in the pore wall (Fig. 6.6). This dependence has been verified to be identical for all walls of the square pore. Moreover, it exhibits mirror symmetry about the center position (Fig. 6.6g), ensuring that the simulation noise is negligible. For vacancy diffusion in a 5×5 square pore with walls that are seven cells wide (Fig. 6.6a, b), asy varies consistently with position when the jumps are selected following a priori defined probabilities, irrespective of the particle interaction being positive or negative or of the destination cell having been chosen randomly from all free neighbor cells. However, the magnitude of a_{sy} depends strongly on the selection rule defined by the jump probability, as indicated in Fig. 6.6g by the scaling factors. It is highest at the corner positions and lowest at the center position. For random jumps to empty cells, a_{sy} was more than 1 order of magnitude smaller than for repulsive interaction so that the number of particle jumps had to be increased to 10^9, resulting in 3 h computation time for each data point in the corresponding trace (Fig. 6.6e, black).

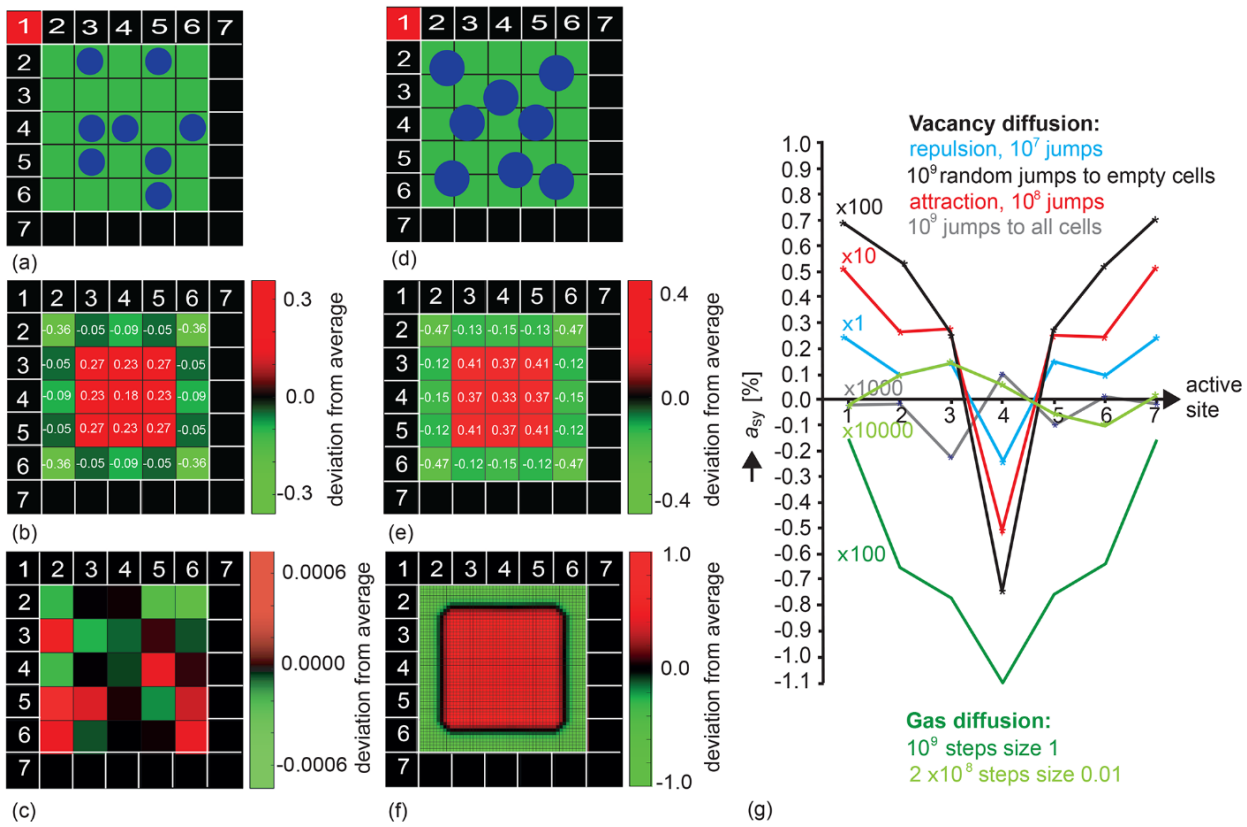

Figure 6.6. *Population density distributions and dependencies of the asymmetry parameter asy on the position of the active relaxation site in the wall of a pore with 5 × 5 cells. (a) Vacancy diffusion. Particles can jump one step on the grid in eight directions. (b) Deviations from average relative density 1 for 10^9 jumps chosen at random to any of the free neighbor cells. (c) Deviations from average relative density 1 for 10^9 jumps chosen at random to any of the eight neighbor cells. (d) Gas diffusion. The particle motion is computed on a fine grid. (e) Deviations from average relative density 1 for 10^9 observations of particle positions at observation intervals of duration 1. The particle position at the time of observation is binned to the coarse vacancy diffusion grid. (f) Deviations from average relative density 1 on a fine 50 × 50 grid of 0.1 particle diameters for 10^9 observations of particle positions at observation intervals of duration 0.01. (g) Variations of the asymmetry parameter with the position of the active site in the cell wall for differently interacting particles for vacancy diffusion at T = 0.2, P = 0.3, and different jump probabilities, as well as for gas diffusion at long and short observation intervals of 1 vs. 0.01. The mirror symmetry of each trace about the center position reports high precision of the simulation.*

Interestingly, for gas diffusion (Fig. 6d), a_{sy} varies at long observation intervals (Fig. 6.6g, green) in a fashion similar to that for vacancy diffusion and is of a magnitude comparable to that of vacancy diffusion (Fig. 6.6g, black) but does not change sign with the position of the active site in the pore wall. In all these cases, the precision of the asymmetry parameter a_{sy} obtained in the simulations exceeds the second relevant digit. If the jumps in the vacancy diffusion simulations are chosen without bias from a jump probability, then no exchange asymmetry is detected; only noise nearly more than 1 order of magnitude lower than for jumps selected at random to one of the free neighbor positions is detected (Fig. 6.6g, gray). Similarly, the asymmetry parameter decreases with the observation time, becoming shorter by more than 2 orders of magnitude, as illustrated in Fig. 6.6g, for a long time step of 1 (dark green) versus a short time step of 0.01 (light green) in simulation units of $(\mathrm{m\ s^2} / k_\mathrm{B}T)^{1/2}$.

The particle dynamics manifested in a_{sy} are accompanied by variations of the average population density across the pore, which is depleted in the contact layer of the particle with the pore wall, enhanced in the next layer, and tapers off towards the pore center in both cases (Figs. 6.6b, e, S4). The densities vary in a similar fashion across the pore for both types of diffusion, albeit having somewhat different values, as can be verified by close inspection of the numbers in each cell in Fig. 6.6b and e. These density variations disagree with Boltzmann's argument that elastic collisions with the walls effectively remove the impact of the walls to the effect that the walls can be neglected. Agreement, however, is reached if the destination cells for particle jumps in vacancy diffusion are chosen at random from all and not just the free neighbor cells (Fig. 6.6c) [24]. Shortening the observation interval in the gas diffusion simulations, however, maintains the unphysical density distribution across the pore and has no effect due to binning of the particle positions to the vacancy diffusion grid at the time of observation as the exact moment of a particle collision cannot be determined on a discrete time axis. On a finer grid, however, the population density is homogeneous, except in the regions close to the walls, which the centers of the circular particles cannot approach (Fig. 6.6f). If, however, projected onto the coarse vacancy diffusion grid, the population density modulations (Fig. 6.6e) reappear because the exact locations of collisions cannot be determined in a simple way at finite observation time intervals. Nevertheless, for both algorithms, the asymmetry parameter

approaches zero for all positions along the wall of the square pore (Fig. 6.6g, light green), confirming that detailed balance is observed.

The maps in Fig. 6.6b, c, e, and f, which reveal the deviation of local population density from average population density, were calculated by summing the 2D maps of particle locations after each jump or at each observation time, normalizing the resultant maps to the number of jumps and the particle density and subtracting the average mean expected for a constant particle density across all cells in the pore. Further maps of population density variations for the two different pores of Fig. 6.3 with other sizes and interaction parameters are summarized in Fig. S4 of the Supplement. While the particle density varies less with temperature for vacancy diffusion, different density patterns are found at different pressures. The strongest density variations are near the pore wall regardless of whether the interaction is repulsive, attractive, or based on prior knowledge that a neighbor cell is occupied. This becomes particularly evident for larger pores (Fig. S4b, d, e). Coincidentally, at low density, the main features of the density maps are strikingly similar for vacancy diffusion with destination cells chosen randomly from among the free neighbor cells (Fig. S4b) and for gas diffusion (Fig. S4d). The particle density is strongly depleted at the pore corners and near the wall and is significantly increased in the next particle layer (Fig. S4e, f). For interacting particles, this concentration variation is carried forwards in vacancy diffusion with increasing distance from the wall, leading to concentration waves which taper off towards the center of the pore and interfere with each other coming from different directions. For small pores, interference patterns dominate the density distribution across the pore (Figs. 6.6b, e and S4a, c). For particles jumping randomly to empty neighbor cells, the decay of the concentration wave towards the pore center is fast, with few to no oscillations towards the pore center, while the oscillations are enhanced by conditioning the jump probability with a hypothetical free-jump energy (Fig. S4d, $P = 0.2$). In particular, the population density at the active site in the dent of the complex pore of Fig. 6.3a depends on the parameters P and T (Fig. S4a, b).

6.4 Discussion

Confined two-dimensional diffusion has been modeled by two different algorithms to investigate to what extent the cross-peaks in 2D $T_2 - T_2$ exchange maps can be asymmetric. The asymmetry is quantified by an asymmetry parameter a_{sy}, which indicates the relative flux between two sites corresponding to the difference in the number of forward and backward exchanges normalized to the total number of exchanges. The vacancy diffusion algorithm models particle jumps on a checkerboard grid to the nearest neighbor cells under the constraint of different jump probabilities and samples the population map after each jump. The jump probability was determined from a Boltzmann distribution with a heuristic free energy which depends on the populations of the surrounding cells. The asymmetry parameters turned out to be equal to zero in the case of equal jump probability to all neighbor cells [24], whether occupied or not, confirming the validity of detailed balance (Fig. 6.6g). They were found to be different from zero when different jump probabilities were assigned to different neighbor cells, i.e., when the jump energy depended on the population pattern of the neighbor cells. However, with the statistical arrangement of the particles on a checkerboard and the confinement of the interaction force to the next-nearest neighbors, energy was not conserved with a particle move so that each particle move either injected or extracted energy from the system. Nevertheless, the equilibrium condition (Eqs. 6.2 and 6.3) was fulfilled so that the system was not in thermodynamical equilibrium but rather in an equilibrium that was driven by the algorithm. The observed asymmetry parameter was, therefore, assigned to a driven and not thermodynamic equilibrium.

The gas diffusion algorithm models particles colliding with initial velocity vectors and calculates new velocity vectors after a collision from conservation of energy and momentum, whereby the instant of a collision is interrogated on a discrete time grid. The smaller the observation time, the more precisely the instant of a collision is determined. Any deviation from the exact collision time leads to errors in the position coordinates of the colliding particles and thus their velocities (Eqs. 6.7, 6.8) [32]. While for large observation times a significant asymmetry parameter is observed (Fig. 6.6g, dark green), its value shrinks drastically when the observation time is reduced by a factor of 100 (Fig. 6.6g, light green). It is concluded

that, with the limit of infinitely short observation time, the gas diffusion algorithm can also produce a vanishing asymmetry parameter in a three-site exchange in agreement with the principle of detailed balance and with symmetry in the cross-peak intensities of exchange maps in thermodynamic equilibrium. If, on the other hand, the velocities are calculated with a systematic error in the gas diffusion model due to a finite observation interval, the resultant velocities disagree with the energy and momenta of elastic collisions so that, here, energy is also injected or extracted from the system, and the observed asymmetry parameter can be attributed to a driven and not a thermodynamic equilibrium.

The asymmetry parameters observed for either of the two pore shapes (Fig. 6.3) investigated with the vacancy diffusion model vary in a range on the order of $-1\% < a_{sy} < 1\%$; i.e., up to 1% of all particles in the pore do not follow the detailed balance between all pairs of sites but move coherently in circles between the three sites. It is emphasized that this circular exchange is between the pools of particles representing the three sites, and it is not a motion followed by individual particles completing circular jumps. Given repulsive or attractive interaction in the vacancy diffusion model with heuristic temperature- and pressure-dependent jump probabilities, the variations of asy with temperature *T* appear to be rapid, reminiscent of phase transitions (Figs. 6.4a, b, S3a). The variations of asy with pressure corresponding to population density *P* are smooth (Figs. 6.4d, e, S3b). Either positive or negative values of asy are observed as *T* or *P* change. A sign change of asy indicates a change in the sense of the circular exchange (see Fig. 6.1).

For a simple square pore, the asymmetry parameter varies with the position of the active site in the cell wall, exhibiting mirror symmetry with respect to the wall center (Fig. 6.6g). The variation is the same for the different jump probabilities, referred to as repulsive and attractive interaction or random jumps to empty cells; albeit it differs significantly in magnitude. A similar dependence is observed in the gas-phase diffusion simulations at long observation times. Moreover, the autocorrelation functions and their Fourier transforms have been determined for the occupancy time tracks of selected cells at specific positions inside a small square pore for 10^7 jumps of all particles in the pore (Fig. 6.5). The time track function was devised to have zero mean for the average cell population. Depending on the position of the cell inside the pore, the

autocorrelation functions and their Fourier transforms vary. Specifically, the autocorrelation function can exhibit a significant constant offset. At these positions inside the pore, the particle densities are different from the pore average, and the cell is, on average, emptier or more occupied than would be expected if the exchange between all cells were the same. This conclusion is supported by the observed deviations of the cell occupancies from the pore average (Figs. 6.6b, e, S4). Near the pore wall, the average population density is depleted and varies in an oscillatory manner along the pore wall. Further towards the center of the pore, the average population density increases sharply and then tapers off towards the pore center to a value slightly above the average density.

These observations for driven vacancy diffusion in a square pore with 5×5 cells are compared to independent simulations of driven gas diffusion (long observation time – step size 1) of non-interacting particles in a square pore with an edge length of five particle diameters and that also allows for seven relaxation centers along the pore wall (Fig. 6.6a, d). A similar variation of the asymmetry parameter is found for vacancy diffusion, but the asymmetry parameter is negative for all positions of the active site (Fig. 6.6g, dark green). Moreover, the depletion of the average particle density at the pore wall and its subsequent variation towards the center are similar, with the exception that oscillations of the average particle density along the pore wall are weaker for gas diffusion (Fig. 6.6b, e). These oscillations persist even at short observation times due to the uncertainty of localizing the particle positions at the exact time of their collision on a discrete time grid. The lack of a sign change in the asymmetry parameter with changing position of the active site may be explained by the destructive interference of particle collisions from multiple sites with the wall within one discrete particle diameter and the fact that the free path length between collisions in gas diffusion is not limited to the next cell as in vacancy diffusion but can range up to the pore diameter. Taken together, the observed asymmetry in the three-site exchange in driven equilibrium and the variation of the jump statistics with position inside the pore point to diffusive resonance phenomena like standing waves of air in pipes, as reported by Kundt [36], or vibrating plates, as reported by Chladni [37].

Three-site exchange can be viewed as a finite-difference approximation to the Laplace operator [12,36] governing Fick's second law [39]. Considering some local site N with neighbor sites N – 1 and N + 1 to the right and left, the mass flow to and from site N given by Eq. (6.1) is

$$\frac{dm_N(t)}{dt} = k_{N,N-1}m_{N-1} - k_{N-1,N}m_N + k_{N,N+1}m_{N+1} - k_{N+1,N}m_N \tag{6.10}$$

Taking the limit to the infinitesimally small distance $\Delta r \to dr$ between the neighboring sites leads to $k_{j,i} = k$, revealing that Eq. (6.10) is a finite-difference approximation of a second spatial derivative balanced by the temporal variations of *m* during infinitesimal time d*t*:

$$(k\, m_{N-1} - 2\, k\, m_N + k\, m_{N+1})/\Delta r^2 \approx k\, \frac{d^2m}{dr^2} = \frac{dm}{dt}/\Delta r^2\,. \tag{6.11}$$

In this limit, Eq. (6.11) becomes Fick's second law, with the diffusion coefficient $D = k\Delta r^2$. This back-of-the-envelope argument suggests that the observed asymmetry of the three-site exchange is a property of Fick's second law and relates to eigenmodes of the Laplace operator [40,41].

The diffusion equation applicable to longitudinal magnetization in NMR instead of particle masses m is the Bloch–Torrey equation [42]:

$$\frac{\partial}{\partial t}m(r,t) = D\nabla^2 m(r,t) - \mu\, m(r,t), \tag{6.12}$$

where *m* now is the magnetization deviation from thermal equilibrium, and μ is the bulk relaxation rate. $m(r,t)$ solves this equation in terms of an expansion into normalized eigenfunctions $\phi_n(r)$ with amplitudes A_n and eigenvalues τ_n [43,44]:

$$m(r,t) = e^{-\mu t}\sum_{n=0}^{\infty} A_n\, \phi_n(r) e^{-\frac{t}{\tau_n}}. \tag{6.13}$$

The eigenvalues are determined by the boundary condition

$$D\, \vec{n}\, \Delta\phi_n(r) = \rho\, \phi_n(r) \tag{6.14}$$

where ρ is the surface relaxivity, and $\vec{n}$ is the unit vector normal to the surface. They depend on the diffusion coefficient and determine the NMR relaxation time in different ways according to the pore geometry. The population ϕ_0 of the lowest normal mode has no nodes. The higher normal modes ϕ_n

possess nodal surfaces. The higher diffusion eigenmodes have been detected by NMR with selective excitation of partial pore volumes making use of field gradients internal to the pore [44]. These experimental results reported by Song agree with the Monte Carlo simulations of driven diffusive translational motion in pores reported here in that the population density varies across the pore, and the offset of the autocorrelation function of the local pore occupancy depends on the position of the cell in the pore. It needs to be investigated further how much the NMR relaxation times and the associated particle dynamics vary with the position from the pore wall to the center in the driven concentration wave [45]. On the other hand, stochastic resonance in thermodynamic equilibrium was observed with NMR first by Sleator et al. [46] and subsequently studied in detail in different scenarios by Müller and Jerschow [47] and Schlagnitweit and Müller [48]. There, the magnetization fluctuating with the thermal motion of the nuclear spins assumes the role of the particles, and the resonance circuit assumes the role of the pore. Diffusion eigenmodes are expected to be unobservable with this method unless a subset of modes is driven by an external stimulus because they may be silent in thermodynamic equilibrium.

From the exchange asymmetry of the particles in the square pore investigated in Fig. 6.6, a suggestive picture emerges for driven confined vacancy diffusion (Fig. 6.7), where the diffusion lengths are confined to the distances from the particle to the direct neighbor cells. Depending on the sign of the asymmetry parameter (Fig. 6.7a), a small fraction of the particles (blue circles) prefer the direct path towards or away from the active site (red square) at the pore boundary over the path along the boundary to or from the active site. In the center of the wall, the direct path away from the active site to the bulk is preferred over the path along the pore wall when leaving the region in contact with the active site (Fig. 6.7b). But because jumps are allowed only to neighboring cells in vacancy diffusion, the cells belonging to relaxation pool 2 at the wall to the right and left of the active site 3 must be populated from the bulk 1 by direct jumps from the bulk to the wall. For these jumps, the asymmetry parameter is indeed positive, as

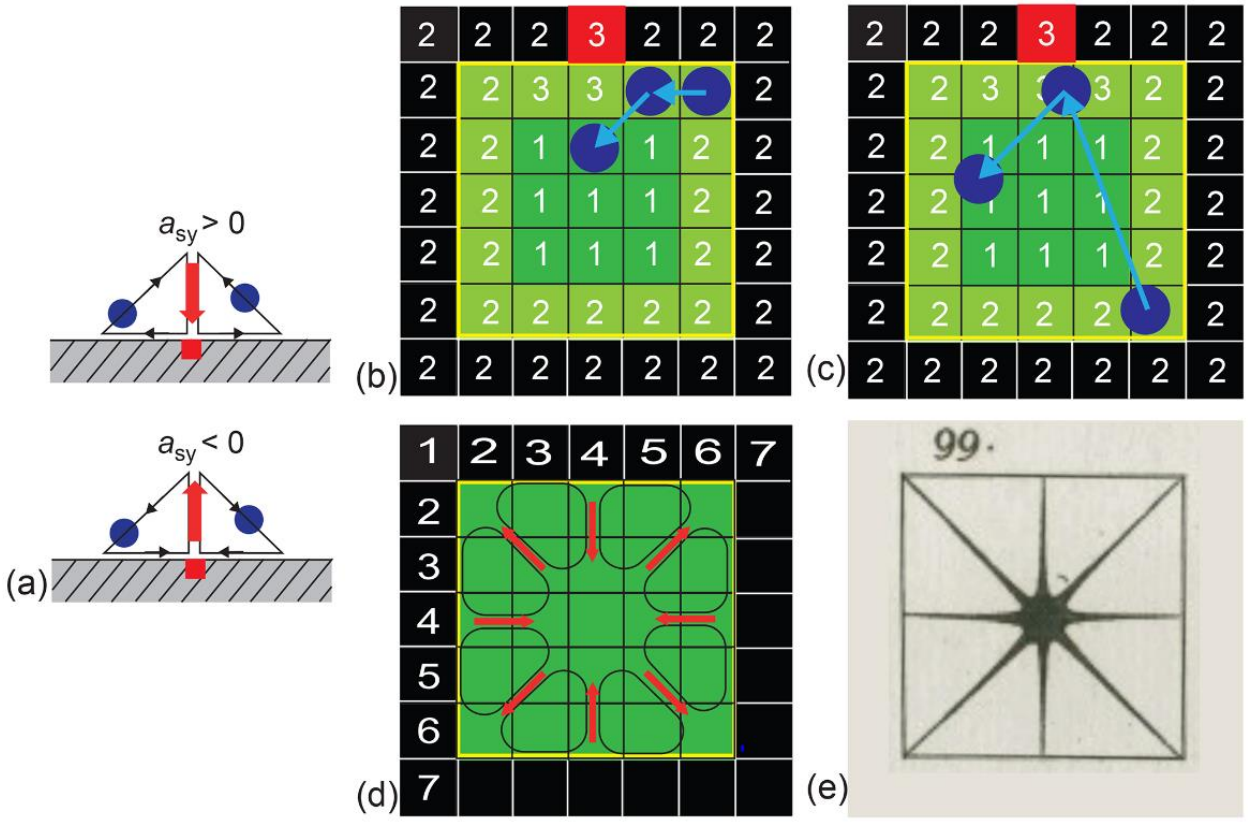

Figure 6.7. *Illustration of the exchange asymmetry in driven equilibrium for the square pore of Fig. 6a. (a) Depending on the sign of the asymmetry parameter, a small fraction of diffusing particles (blue circles) prefer the direct path towards or away from the active site (red square) at the pore boundary over the path along the boundary from the active site. (b) Vacancy diffusion for negative asymmetry parameter and the active site 3 in the center of the pore wall. Jumps are limited to the next-nearest cells. The direct path away from the active site to the bulk 1 in the center is preferred over the path along the pore wall 2 when leaving the region in contact with the active site. (c) Gas diffusion for negative asymmetry parameter and the active site 3 in the center of the pore wall. The free paths between collisions can span the entire cell. (d) In-plane translational vacancy diffusion paths resulting from the variation of the asymmetry parameters with the position of the active site on the pore wall depicted in Fig. 6.6g. (e) Out-of-plane vibrational mode of a square plate observed by Chladni [37].*

observed for the off-center positions of the active site (Fig. 6.6g). Given the symmetry of the square pore, the in-plane translational diffusion paths resulting from the variation of the asymmetry parameters with the position of the active site on the pore wall demand the existence of eight diffusion vortices inside the planar pore (Fig. 6.7d). The symmetry of this in-plane translational diffusion pattern matches the symmetry of one of the node patterns of the out-of-plane vibrational modes of a square plate observed by Chladni (Fig. 6.7e) about a quarter of a millennium earlier [37]. This also suggests that the dynamic of driven vacancy diffusion observed in the computer model reported here is a resonance feature of the pore and thus relates to diffusion eigenmodes. The resonance effect is less pronounced for gas diffusion (Fig. 6.7c) where the free paths between collisions can span the entire cell. Because the mass flow from relaxation site 2 to the active site 3 can be sustained from any position at the pore wall, the asymmetry parameter does not need to change sign when the active site moves along the pore wall (Fig. 6.7e), and the circular paths can have various shapes and can extend across the entire pore so that the vortex pattern is largely washed out.

Given the technological importance of fluid motion in small pores in heterogeneous catalysis [49], it will be interesting to explore whether such a correlated motion resulting from standing longitudinal particle concentration wave patterns near pore walls can be driven by external stimuli like ultrasound, electric, or magnetic fields. The standing waves could be enhanced by tuning the driver frequency to the pore resonance like a musician enforces resonance modes on a flute when playing. To enhance the resonance modes, low-power, broadband, forced oscillations can also be considered, such as in Fourier transform infrared spectroscopy [50] and stochastic NMR spectroscopy [51], while triggering free oscillations by means of high-power impulses may destroy the porous medium under study.

6.5 Summary

The evidence provided by Monte Carlo simulations of random particle jumps on a 2D checkerboard and by simulations of 2D gas diffusion with topological confinements supports the notion that asymmetry in three-site exchange maps is an indication of the non-Brownian diffusion dynamics of confined particles

in driven equilibrium. Depending on the sign of the asymmetry parameter, a small fraction of all particles prefers the direct path towards or away from the active site at the pore boundary over the path along the boundary to or from the active site, resulting in a circular flux (Fig. 6.7). Both driven vacancy diffusion and driven gas diffusion produce congruent results. These are as follows: (1) circular exchange is a manifestation of driven equilibrium and leads to asymmetry of exchange peaks, while thermodynamic equilibrium manifests itself in the detailed balance and symmetry of exchange peaks. (2) The circular exchange in driven equilibrium appears to be a resonance phenomenon which can potentially be driven by external stimuli. Yet, the reported simulations are limited to two dimensions, and it may be argued that the asymmetry of exchange vanishes in the more common pores with three spatial dimensions. However, two-dimensional diffusion is not an abstract model and arises for gas atoms adsorbed to metal surfaces [52] so that the driven coherent particle diffusion indicated by the non-zero asymmetry parameter may be observed there. Given the congruent simulation evidence for driven vacancy diffusion and gas diffusion in two-dimensional confinements, it is hypothesized that confined diffusion can be partially converted to coherent motion by external excitation so that the detailed balance will be violated as observed in nonequilibrium phenomena [2,3].

References

[1] Bunde, A., Caro, J., Kärger, J., and Vogel, G. (Eds.): Diffusive Spreading in Nature and Technology, Springer Nature, Cham, ISBN: 978-3-319-88489-9, 2018.

[2] Gnesotto, F. S., Mura, F., Gladrow, J., and Broedersz, C. P., Broken detailed balance and non-equilibrium dynamics in living systems: a review, Rep. Prog. Phys., **81**, 066601 (2018) https://doi.org/10.1088/1361-6633/aab3ed

[3] Lynn, C. W., Cornblath, W. J., Papadopoulos, L., Bertolerod, M. A., and Bassett, D. S.: Broken detailed balance and entropy production in the human brain, P. Natl. Acad. Sci. USA, 118, e2109889118, https://doi.org/10.1073/pnas.2109889118, 2021.

[4] Ernst, R. R., Bodenhausen, G., and Wokaun, A.: Principles of Nuclear Magnetic Resonance in One and Two Dimensions, Clarendon Press, Oxford, ISBN: 13 978-0198556299, 1987.

[5] Callaghan, P. T.: Translational Dynamics and Magnetic Resonance: Principles of Pulsed Gradient Spin Echo NMR, Oxford University Press, Oxford, ISBN: 9780199556984, 2011.

[6] Jeener, J., Meier, B. H., Bachmann, P., and Ernst, R. R.: Investigation of exchange processes by two dimensional NMR spectroscopy, J. Chem. Phys., 71, 4546–4553, 1979.

[7] Lee, J.-H., Labadie, C., Springer Jr., C. S., and Harbison G. S.: Two-Dimensional Inverse Laplace Transform NMR: Altered Relaxation Times Allow Detection of Exchange Correlation, J. Am. Chem. Soc., 115, 7761–7764, 1993

[8] Lacabanne, D., Wiegand, T., Di Cesare, M., Orelle, C., Ernst, M., Jault, J.-M., Meier, B. H., and Böckmann, A.: Solid-State NMR Reveals Asymmetric ATP Hydrolysis in the Multidrug ABC Transporter BmrA, J. Am. Chem. Soc., 144, 12431–12442, 2022.

[9] Björgvinsdóttir, S., Moutzouri, P., Walder, B. J., Matthey, N., and Emsley, L.: Hyperpolarization transfer pathways in inorganic materials, J. Magn. Reson., 323, 106888, https://doi.org/10.1016/j.jmr.2020.106888, 2021.

[10] Olaru, A. M., Kowalski, J., Sethi, V., and Blümich, B.: Exchange relaxometry of flow at small Péclet numbers in a glass bead pack, J. Magn. Reson., 220, 32–44, 2012.

[11] Han, S.-I. and Blümich, B.: Two-dimensional representation of position, velocity, and acceleration by PFG-NMR, Appl. Magn. Res., 18, 101–114, 2000.

[12] van Kampen, N. G.: Stochastic Processes in Physics and Chemistry, Elsevier, Amsterdam, ISBN: 9780444529657, 1992.

[13] Onsager, L.: Reciprocal Relations in Irreversible Processes, Phys. Rev., 37, 405–426, 1931.

[14] Sandstrom, J.: Dynamic NMR Spectroscopy, Academic Press, Cambridge, MA, ISBN: 13 978-0126186208, 1983

[15] Maxwell, J. C.: On the dynamical theory of gases, Philos. T. R. Soc. Lond., 157, 49–88, 1867.

[16] Boltzmann, L.: Weitere Studien über das Wärmegleichgewicht unter Gasmolekülen, Sitzungsber. Kais. Akad. Wiss., Wien, Math, Natruwiss. Classe, 66, 275–370, 1872.

[17] Einstein, A.: Zur Quantentheorie der Strahlung, Phys. Z., 18, 121–128, 1917.

[18] Valiullin, R. (Ed.): Diffusion NMR of Confined Systems, R. Soc. Chem., Cambridge, ISBN: 978-1 78262-190-4, 2017.

[19] McDonald, P. J., Korb, J.-P., Mitchell, J., and Monteilhet, L.: Surface relaxation and chemical exchange in hydrating cement pastes: A two-dimensional NMR relaxation study, Phys. Rev. E, 72, 011409, https://doi.org/10.1103/PhysRevE.72.011409, 2005.

[20] Van Landeghem, M., Haber, A., d'Espinose de Lacaillerie J.-B., and Blümich, B.: Analysis of Multisite 2D Relaxation Exchange NMR, Concepts Magn. Reson. A, 36, 153–169, 2010.

[21] Gao, Y. and Blümich, B.: Analysis of three-site T2-T2 exchange NMR, J. Magn. Reson., 315, 106740, https://doi.org/10.1016/j.jmr.2020.106740, 2020.

[22] Song, Y.-Q., Venkataraman, L., Hürlimann, M. D., Flaum, M., Frulla, P., and Straley, C.: T1-T2 Correlation Spectra Obtained by Using a Fast Two-Dimensional Laplace Inversion, J. Magn. Reson., 154, 261–268, 2002.

[23] Feynman, R., Leighton, R. B., and Sands, M.: The Feynman Lectures on Physics, Vol. 1, Chap. 46, Addison-Wesley, Reading, Fourth Printing, ISBN: 0-201-02116-1, 1966

[24] Metropolis, N., Rosenbluth, A.W., Rosenbluth, M. N., Teller, A. H., and Teller, E.: Equation of State Calculations by Fast Computing Machines, J. Chem. Phys., 21, 1087–1092, 1953.

[25] Grebenkov, D. S.: A fast random walk algorithm for computing the pulsed-gradient spin-echo signal in multiscale porous media, J. Magn. Reson., 208, 243–255, 2011.

[26] Hughes, B. D.: Random Walks and Random Environments, Clarendon Press, Oxford, https://doi.org/10.1016/j.jmr.2010.11.009, 1995.

[27] Sabelfeld, K. K.: Monte Carlo Methods in Boundary Value Problems, Springer-Verlag, Berlin, ISBN: 13 978-0387530017, 1991.

[28] Seitz, F.: On the Theory of Vacancy Diffusion in Alloys, Phys. Rev., 74, 1513–1523, 1948.

[29] Wolf-Gladrow, D. A.: Lattice-Gas Cellular Automata and Lattice Boltzmann Models, Springer, Berlin, ISBN: 3-540-66973-6, 2000.

[30] Bialynicki-Birula, I. and Bailynicky-Birula, I.: Modeling Reality, Oxford University Press, Oxford, ISBN: 9780198531005, 2004.

[31] Blümich, B., Parziale, M., and Augustine, M.: Monte-Carlo Analysis of Asymmetry in Three-Site Relaxation Exchange: Probing Detailed Balance, Magn. Reson. Discuss. [preprint], https://doi.org/10.5194/mr-2023-8, in review, 2023.

[32] Michel, M., Kapfer S. C., and Krauth, W.: Generalized event-chain Monte-Carlo: Constructing rejection-free global-balance algorithms from infinitesimal steps, J. Chem. Phys., 140, 054116, https://doi.org/10.1063/1.4863991, 2014.

[33] Stepišnik, J., Mohoric, A., Lahajnar, G., Mattea, C., Stapf, S., and Sersa, I.: Velocity autocorrelation spectra in molten polymers measured by NMR modulated gradient spin-echo, Europhys. Lett., 106, 27007, https://doi.org/10.1209/0295-5075/106/27007, 2014.

[34] Callaghan, P. T. and Stepišnik, J.: Modulated Gradient NMR, J. Magn. Reson., 117, 118–122, 1995.

[35] Parsons, E. C., Does, M. D., and Gore J. C.: Temporal Diffusion Spectroscopy: Theory and Implementation in Restricted Systems Using Oscillating Gradients, Magn. Reson. Med., 55, 75–84, 2006.

[36] Kundt, A.: Über eine neue Art akustischer Staubfiguren und über die Anwendung derselben zur Bestimmung der Schallgeschwindigkeit in festen Körpern und Gasen, Annal. Phys. Chem., 203, 497–523, 1866.

[37] Chladni, E. F. F.: Entdeckungen über die Theorie des Klanges, Leipzig, Weidmanns Erben und Reich, ISBN: 13 978-1278266992, 1787.

[38] Kuprov, I.: private communication with BB at the EUROMAR 2022 conference in Utrecht, July 10–14, ISBN: 978-3-527-31024-1, 2022.

[39] Fick, A.: Ueber Diffusion, Ann. Phys., 94, 59–86, 1855.

[40] de Hoop, A. T. and Prange, M. D.: Variational analysis of the natural decay rates and eigenmodes of cavity-enclosed diffusive fields, J. Phys. A, 40, 12463–12477, 2007.

[41] Grebenkov, D. S. and Nguyen, B.-T.: Geometrical Structure of Laplacian Eigenfunctions, SIAM Rev., 55, 601–667, 2013.

[42] Torrey, H. C.: Bloch Equations with Diffusion Terms, Phys. Rev., 104, 563–565, 1956.

[43] Brownstein, K. R. and Tarr, C. E.: Spin-Lattice Relaxation in a System Governed by Diffusion, J. Magn. Reson., 26, 17–24, 1977.

[44] Song, Y. Q.: Detection of the High Eigenmodes of Spin Diffusion in Porous Media, Phys. Rev. Lett., 85, 3887–3881, 2000.

[45] Bytchenkoff, D. and Rodts, S.: Structure of the two-dimensional relaxation spectra seen within the eigenmode perturbation theory and the two-site exchange model, J. Magn. Reson., 208, 4–19, 2011.

[46] Sleator, T., Hahn, E. L., Hilbert, C., and Clarke, J.: Nuclear Spin Noise, Phys. Rev. Lett., 55, 1742–1745, 1985.

[47] Müller, N. and Jerschow, A.: Nuclear Spin Noise Imaging, P. Natl. Acad. Sci. USA, 103, 6790–6792, 2005.

[48] Schlagnitweit, J. and Müller, N.: The first observation of Carbon-13 spin noise spectra, J. Magn. Reson., 224, 78–81, 2012.

[49] Kärger, J., Ruthven, D. M., and Theodorou, D. N. (Eds.): Diffusion in Nanoporous Materials, Vol. 1, Wiley-VCH, Weinheim, ISBN: 9780198537885, 2012.

[50] Michelson, A. A.: Light Waves and Their Uses, The University of Chicago Press, Chicago, 1903.

[51] Ernst, R. R.: Magnetic Resonance with Stochastic Excitation, J. Magn. Res., 3, 10–27, 1970

[52] Oura, K., Lifshits, V. G., Saranin, A. A., Zotov, A. V., and Katayama, M.: Surface Science: An Introduction, Springer, Berlin, Chap., 13, https://doi.org/10.1063/1.1825276, 2013.

Appendix

A 1D Matrix Pencil Method Script

This appendix entry contains a Matlab script for the 1D MPM algorithm. This script works for T_1 and T_2 relaxation as is. An additional line can be added to calculate diffusion coefficients from decay rates. For this algorithm to work, the x axis must be linearly spaced.

```
function [eigvals, sigrecon, rates, ampmatrix] = mpm1d(time, data, relaxcomps)

%%% Script for the calculation of relaxation rates by the Matrix Pencil Method %%%
fullrank = size(data); %Initial rank of the data matrix
timepts = max(fullrank); %Number of time steps
dt = time(2)-time(1); %Dwell time for experiment. Time axis must be linearly spaced

%%% SVD Filter %%%
sigmat = hankel(data); %Transforms 1D transient into a matrix form
[u,s,v] = svd(sigmat); %Singular Value Decomposition of data matrix
sprune(:,:) = s(1:relaxcomps,1:relaxcomps); %"Prunes" the data matrix by reducing the
uprune(:,:) = u(:,1:relaxcomps);            %rank to the number of relaxation components
vprune(:,:) = v(:,1:relaxcomps);

svdrecon = uprune*sprune*vprune'; %reconstruction of data matrix after filter

%%% Matrix Pencil Estimates of Decay Constants and Amplitudes %%%
mp1(:,:) = svdrecon(:,1:(max(fullrank) - 1)); %Generates the matrix pencils
mp2(:,:) = svdrecon(:,2:max(fullrank));
```

```
fulleigvals = eig(pinv(mp1)*mp2); %Solves the generalized eigenvalue problem
eigvals = fulleigvals(1:relaxcomps); %reduces to only physical eigenvalues
rates = -log(eigvals)./dt; %Calculating relaxation rates from eigenvalues

%%% Amplitude matrix %%%
for ii = 1:(max(fullrank)-1)
    leftamp(ii,:) = (eigvals).^(ii-1); %Building left amplitude matrix
end
rightamp = leftamp'; %Building right amplitude matrix
ampmatrix = (pinv(leftamp)*svdrecon(1:(timepts-1),1:(timepts-1))*pinv(rightamp));
%Calculation full amplitude matrix

%%% Data Modeling %%%
sigrecon = sum(diag(ampmatrix).*exp(-dt.*(0:timepts-1).*rates),1);
%Models data from the rates and amplitudes
ampmatrix = ampmatrix/sum(ampmatrix); %Normalizes the amplitude matrix

end
```

B Matrix Pencil Filter Code

This appendix entry contains a Matlab script for the 1D MPM algorithm. For this algorithm to work, the x axis must be linearly spaced.

```
function [out eigs filtrates rates ampmpm] = mpm1dfilt_complex(tax,yax,sigval,cutofffreq);

%%% Begin Code %%%

aa = size(yax);
tpts = max(aa);


dt = tax(2) - tax(1);

%%% make the input matrix and clean it up with SVD %%%

decaymat = hankel(yax);


[u,s,v] = svd(decaymat);

bb = size(s);

for ii = 1:sigval;
   sprune(ii,ii) = s(ii,ii);
   uprune(:,ii) = u(:,ii);
   vprune(:,ii) = v(:,ii);
 end

decaymatsvd = uprune*sprune*vprune';

%%% Matrix Pencil Estimates of Decay Constants and Amplitudes

for ii = 1:(max(aa) - 1);
   d1(ii,:) = decaymatsvd(ii,1:(max(aa) - 1));
   d2(ii,:) = decaymatsvd(ii,2:max(aa));
end

eigy = eig(pinv(d1)*d2);
for jj = 1:sigval;
   for ii = 1:(max(aa)-1);
   aleft1(ii,jj) = ((eigy(jj)))^(ii - 1);
   aright1(jj,ii) = ((eigy(jj)))^(ii - 1);
   end
   rates(jj) = -log((eigy(jj)))/dt;
end
```

```
ampmpm = pinv(aleft1)*decaymatsvd(1:(tpts-1),1:(tpts-1))*pinv(aright1);

xxax = imag(rates);
eigs = xxax;

% figure(1);hist(xxax,sigval)

tt = 1;
ss = 1;
for ii = 1:sigval;
   if abs(imag(rates(ii))) < cutofffreq
            filtrates(tt) = rates(ii);
      filtindex(tt) = ii;
      tt = tt + 1;
   end
end

newsigval = tt - 1;
newampmpm(newsigval,newsigval) = 0;

for ii = 1:newsigval;
   for jj = 1:newsigval;
            newampmpm(ii,jj) = ampmpm(filtindex(ii),filtindex(jj));
   end
end

out(4,tpts) = 0;

for nn = 1:tpts;

   for ii = 1:sigval;
      for jj = 1:sigval;
         %Reconstruction, 1 = complex, 3 = real
         out(1,nn) = out(1,nn) + ampmpm(ii,jj)*(exp(-dt*(nn-1)*(rates(ii))));
         out(3,nn) = out(3,nn) + ampmpm(ii,jj)*(exp(-dt*(nn-1)*real(rates(ii))));
      end
   end

   for ii = 1:newsigval;
      for jj = 1:newsigval;
         %Filtered, 2 = complex, 4 = real
         out(2,nn) = out(2,nn) + newampmpm(ii,jj)*(exp(-dt*(nn-1)*(filtrates(ii))));
         out(4,nn) = out(4,nn) + newampmpm(ii,jj)*(exp(-dt*(nn-1)*real(filtrates(ii))));
      end
   end

end

out = out;
```

C Supplement of "Asymmetry in three-site relaxation exchange NMR"

C.1 Neighborhoods explored in 2D vacancy-diffusion simulations

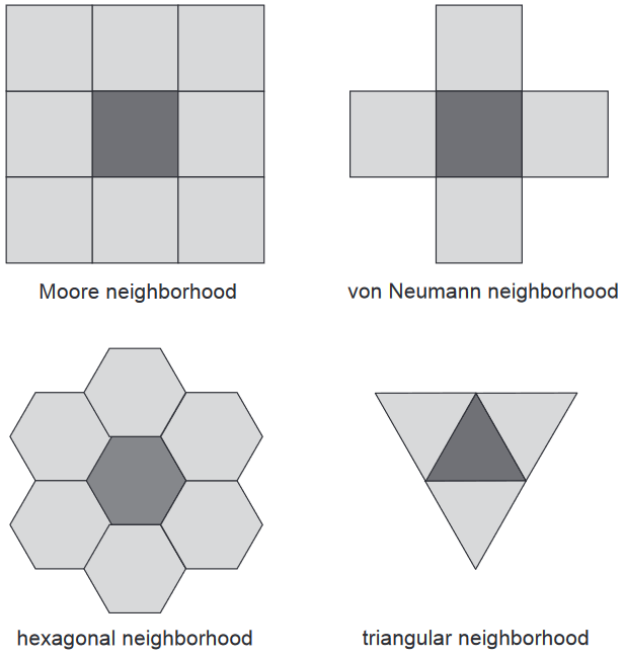

Figure S1. Simulation neighborhoods (grids) of range 1 for jumps from the center position (dark grey) to neighbor positions (light grey). All three asymmetry parameters from Eqn. (4) were calculated at each simulation run. Only the vacancy-diffusion simulations produced with the Moore neighborhood obeyed Eqn. (4), while all gas-diffusion simulations did.

C.2 Empirical Ansatz for the estimation of the transition probability from ΔU and ΔS

In an effort to introduce interactions between a particle and its surroundings, a quantity reminiscent of the free energy change $\Delta A = \Delta U - T\,\Delta S$ is determined from crude models of the internal energy change $\Delta U = -\boldsymbol{F}\,\Delta\boldsymbol{R}$ defined by the net force $\boldsymbol{F}$ exerted from all neighboring particles on the particle at stake and the length $|\Delta\boldsymbol{R}|$ of the jump to the next cell, the temperature T, and the entropy change ΔS. The force $\boldsymbol{F}$ between two particles follows Newton's inverse square distance law. It is proportional to $\frac{1}{|\Delta\boldsymbol{R}|^2}$ In the direction of $\frac{1}{|\Delta\boldsymbol{R}|^2}\Delta\boldsymbol{R}$ from an occupied cell j to the particle i under consideration. The total force the particle i experiences is estimated from the vector sum of the forces exerted from the particles j in all occupied neighbor cells (Fig. 2a),

The internal energy change $\Delta U_{f,i} = -(\boldsymbol{F}_f - \boldsymbol{F}_i)\Delta\boldsymbol{R}_{f,i} \approx \boldsymbol{F}_i\Delta\boldsymbol{R}_{f,i}$ is modeled for each potential jump from the initial, occupied cell i to the final, empty cell f by the product of the net force $\boldsymbol{F}_i$ with the vector $\Delta\boldsymbol{R}_{f,i}$ connecting the centers of the initial cell i and the final cell f.

The entropy change $\Delta S = S_f - S_i$ is the difference between the entropies of the particle with its eight nearest neighbors for the final state f and the initial state i. It is modeled by the sum of the step lengths $R_{f,i} = |\Delta\boldsymbol{R}_{f,i}|$ of the particle i to its unoccupied next nearest neighbor cells f,

$$S_i = \Sigma_f \Delta R_{f,i} \tag{2}$$

In case a neighbor cell is occupied, $\Delta\boldsymbol{R}_{f,i} = 0$. Detailed examples are worked out below.

The sum of distances has been used as a model for the configurational entropy $S = -k_B{*}\Sigma_n P_n \ln(P_n)$, because the configurations on the square grid are discrete and differ so that the standard formula $S = k_B{*}\ln(W)$ does not strictly apply. The sum of jump distances in the Moore neighborhood can be argued to approximate W (but not the logarithm) apart from some scaling factor. This crude approximation exhibits the essential features of entropy: The distance sum is zero, if there is only one possible configuration, and it grows with the number of accessible configurations. For purpose of calculating a jump probability $p = \exp\left\{-\frac{\Delta A}{k_B T}\right\}$ this suffices.

In each jump step, an initially occupied cell i is selected at random and p is evaluated for all possible jumps to neighboring empty cells as potential final cells f. If for one or more jumps $p \geq 1$ is calculated, p is set to 1 and the destination cell of the jump picked at random from this subset of all potential jumps. If all neighbor cells are occupied, $p = 0$, and no jump is counted. If $0 < p < 1$ the destination cell is chosen at random from all those with the same largest jump probability $p < 1$. In the reported simulations, the Boltzmann constant k^* has been set to 1 and so has the shortest distance between neighboring cells.

Two other jump algorithms for choosing the destination cell were also tested: 1) Equal probability for all unoccupied neighbor cells, assigning jump probability zero to occupied cells, and 2) equal probability for choosing the destination cell from all neighbor cells. Respective results are reported in the main body of the manuscript.

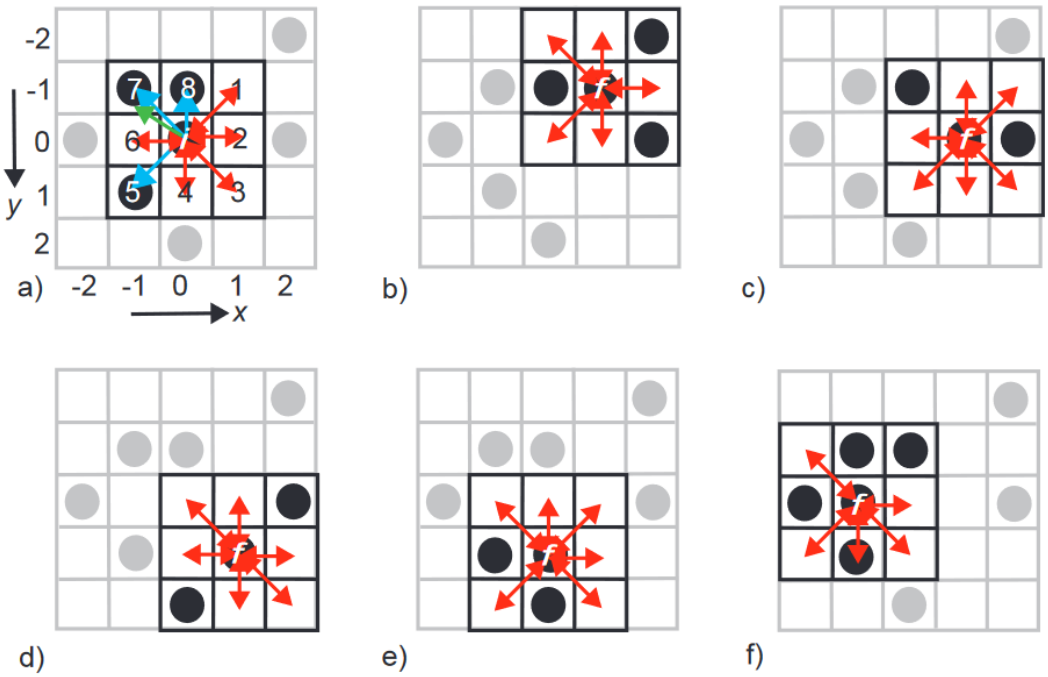

Figure S2. Checkerboard randomly occupied by particles represented by filled circles. a) The cells surrounding the initial particle position i are numbered clockwise from 1 to 8. Cells 5,7, and 8 are occupied, the others are empty. The force (green arrow) on the center particle is calculated as the sum of forces exerted from all particles in the occupied nearest neighbor cells (blue arrows). The entropy is estimated from the sum of distances to all neighboring free cells (red double arrows). b-f) The center particle in a) can jump to any of the free cells 1, 2, 3, 4, and 6, each of which has its own entropy. The final position f of the jump is identified with a bias given by the jump probability based on a simple heuristic model of the free jump-energy difference.

C.3 Temperature and pressure dependences of exchange in the complex pore

Relevant results for the pore structure of Fig. 6.3a are summarized in six graphs in Fig. S3. All parameters are relative quantities without units. The top three graphs a), b) and c) show the variation of a_{sy} with temperature for a population fraction of 0.2 corresponding that of a gas. The asymmetry parameter assumes positive and negative values in a seemingly erratic but reproducible manner in the range of -0.7% $< a_{sy} <$ 0.4% for repulsive interaction (Fig. S3a), i. e. for the definition of the force between particles as illustrated in Fig. 6.2a. The interaction can be changed to attractive by changing the sign of ΔU in the expression for the free energy. In this case the asymmetry parameter varies as well, however, only between $0\% < a_{sy} < 0.5\%$ (Fig. S3b). In either case, up to roughly 0.5% of all jumps on the checkerboard proceed in a circular fashion between the three sites. With reference to Fig. 6.1, positive a_{sy} reports that the straight

entry route from the bulk into the small pore is preferred over the detour via the grain surface. This is the case for attractive interaction at $T < 2$ (Fig. S3b). For repulsive interactions and temperatures $T > 1$, a_{sy} is negative and the opposite route is preferred (Fig. S3a). If the destination cell is chosen at random from all free neighbor cells, then the simulation produces largely noise for a_{sy} (Fig. S3c). The noise level is two orders of magnitude smaller than the maximum absolute values of a_{sy} obtained with either repulsive (Fig. S3a) or attractive interaction (Fig. S3b).

At the extrema of the $a_{sy}(T)$ curves in Figs. S3a,b the dependences of the asymmetry parameters on pressure corresponding to population density were investigated (Figs. S3d-f). The variations with population density are smoother than those with temperature. Positive and negative values of a_{sy} result at a low temperature of $T = 0.2$ for repulsive interaction (Fig. S3d), whereas either negative or positive Asymmetry in three-site exchange NMR relaxometry values arise for repulsive (Fig. S3e) and attractive (Fig. S3f) interactions at higher temperatures of $T = 2.2$ and 1.3, respectively. Interestingly, two well developed positive modes result for attractive interaction at $T = 1.3$.

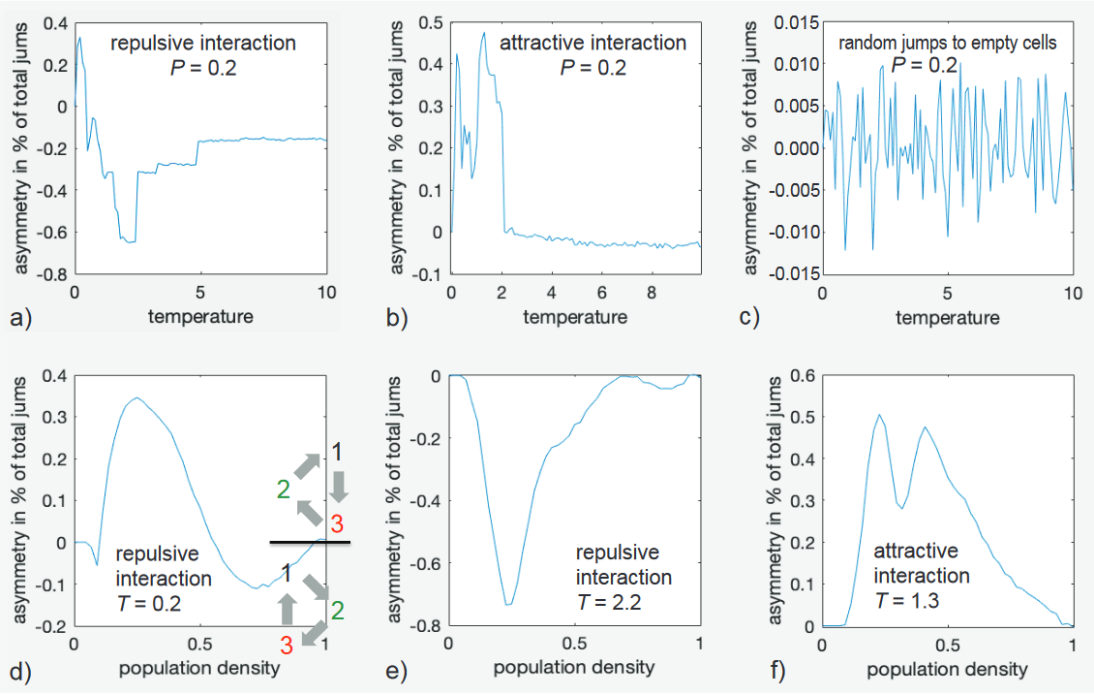

Figure S3. Asymmetry parameters a_{sy} for diffusion in and out of the grain pore depicted in Fig. 3a as a function of relative temperature T (top row) at a population density of 0.2 and relative pressure or population density P (bottom row) at different temperatures. a) $a_{sy}(T)$ for repulsive interaction. b) $a_{sy}(T)$ for attractive interaction. c) $a_{sy}(T)$ for jumps chosen randomly from all free neighbor cells. d) $a_{sy}(P)$ for repulsive interaction at $T = 0.2$. e) $a_{sy}(P)$ for repulsive interaction at $T = 2.2$. f) $a_{sy}(P)$ for attractive interaction at $T = 1.3$.

C.4 Population density distributions for different pores and thermodynamic parameters

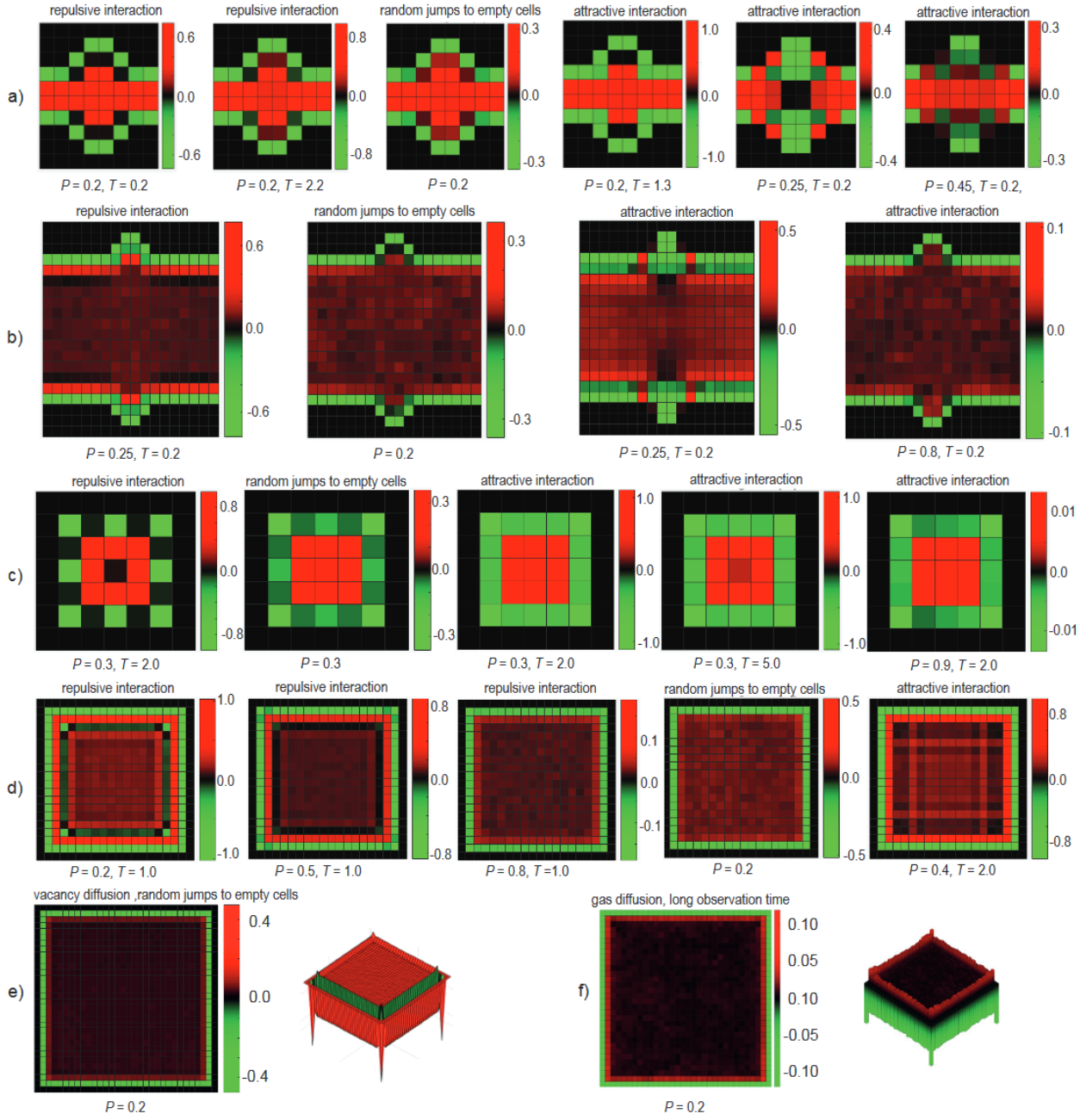

Figure S4. Maps showing the deviations of the particle density from its mean across the pore. a,b) Model for a porous solid, 10^7 jumps. c-e) Square pore, 10^7 jumps. The color scales are different in each plot. The particle concentrations vary more strongly with pressure *P* than with temperature *T*. e) Vacancy diffusion in a 32 × 32 pore with random jumps to empty neighbor cells. f) Gas diffusion in a 32 × 32 pore at a long observation time of 1, 108 jumps.

C.5 Matlab code for vacancy-diffusion simulations

```
% Restricted Diffusion
%
% Define input parameters
ScanP = 0; % 0 = single pass; 1 = scan Pop; 2 = scan T
pore = 2; % 1: dent pore (8 x 10); 2: box pore (7 x 7); 3:
parallel planes
Pop = 0.3; % population-density parameter
T = 0.8; % temperature parameter
propflag = 0; % 1: active jump probability, 0: random jumps
Thermo = 0; % 1: positive DU; 0: DA = 0; else: negative DU
f1 = 1; % scale factor for force among particles
f2 = 1; % scale factor for force by wall
f3 = 1; % scale factor for force by active site
Ny = 7; % number of cells in y direction
Nx = 7; % number of cells in x direction
DeltaP = 0.04; % population-density increment
kB = 1; % thermal energy constant
DeltaT = 0.04; % temperature increment150 Njump = 10000000; % number of jumps
% Constants and derived parameters
Nx1 = round(Nx/2);
Ny1 = round(Ny/2);
Nyc = 3; % detection cell number in y direction
Nxc = 3; % detection cell number in x direction
Nya = 1; % active site cell number in y direction
Nxa = 4; % acive site cell number in x direction
root2 = sqrt(2);
fc = 1/(2*root2); % scale factor for force from corner cells
nix=zeros(2,1);
% SuperLoop for parameter variation
SLcount = 0; % number of parameter variations: default is 0
SLn0 = 1; % parameter-variation counter
if ScanP == 1 SLcount = 25; end % vary Pop
if ScanP == 2 SLcount = 50; end % vary T
SLp = zeros(6,SLcount+1);
if ScanP == 1 % population scan
Pop = 0;
SLn0 = 2;
end
if ScanP == 2 % temperature scan
T = 0;
SLn0 = 2;
end
for SLn = SLn0:SLcount+1% parameter-variation loop starts here *****
if ScanP == 1
Pop = Pop + DeltaP;
SLp(1,SLn) = Pop;
```

```
end
if ScanP == 2
T = T + DeltaT;
SLp(1,SLn) = T;
end
k = zeros(3,3); % kinetic matrix
tau = 0; % initiate calculation of autocorrelation function
taumax = 18*Nx;
if Ny > Nx taumax = 18*Ny; end
p2 = 2; % determine next power of 2 larger than taumax
while p2 < taumax p2 = p2*2; end
taumax = p2;
acorr = zeros(taumax,1);
noisevec = zeros(taumax,1);
% Set up pore space with boundaries
space = zeros(Ny,Nx);
if pore > 2 % parallel planes
space(1,:) = 2;
space(Ny,:) = 2;
space(1,Nxa) = 3; % active site
space(Ny,Nxa) = 3; % active site
end
if pore == 2 % box pore202 space(1,:) = 2;203 space(Ny,:) = 2;204 space(:,1) = 2;205
space(:,Nx) = 2;
space(Nya,Nxa) = 3; % active site
end
if pore < 2 % dent pore
space(1,:) = 2;
space(2,:) = 2;
space(3,:) = 2;
space(Ny-2,:) = 2;
space(Ny-1,:) = 2;
space(Ny,:) = 2;
if Ny >= 8 % define holes
if Nx >= 6
space(3,Nx1-1) = 0;
space(3,Nx1) = 0;
space(3,Nx1+1) = 0;
space(3,Nx1+2) = 0;
space(2,Nx1-1) = 3;
space(2,Nx1) = 0;
space(2,Nx1+1) = 0;
space(2,Nx1+2) = 3;
space(1,Nx1-1) = 3;
space(1,Nx1) = 3;
space(1,Nx1+1) = 3;
space(1,Nx1+2) = 3;
space(Ny-2,Nx1-1) = 0;
space(Ny-2,Nx1) = 0;
space(Ny-2,Nx1+1) = 0;
space(Ny-2,Nx1+2) = 0;
```

```
space(Ny-1,Nx1-1) = 3;
space(Ny-1,Nx1) = 0;
space(Ny-1,Nx1+1) = 0;
space(Ny-1,Nx1+2) = 3;
space(Ny,Nx1-1) = 3;
space(Ny,Nx1) = 3;
space(Ny,Nx1+1) = 3;
space(Ny,Nx1+2) = 3;
end
end
end
emptypore = space; % keep empty pore for reference
% Count and populate available cells
nc0 = 0; % count available cells
for nx = 1:Nx
for ny = 1:Ny
if space(ny,nx) == 0 nc0 = nc0 + 1; end
end
end
noc = round(Pop*nc0); % number of cells to be occupied
if noc == nc0 noc = nc0-1; end
if noc == 0 noc = 1; end
cellvec = zeros(noc,3); % track occupied cells
n = 0;
while n < noc
nxi = randi(Nx);
nyi = randi(Ny);
if space(nyi,nxi) == 0
space(nyi,nxi)=1; % populate
n = n+1;
cellvec(n,1) = n; % track occupied cells
cellvec(n,2) = nyi;
cellvec(n,3) = nxi;
end
end
poc = -noc/nc0;
puc = 1+poc;
avspace = space; % initiate summing occupation maps
% Display cell population
subplot(3,2,1)
heatmap(space);
colormap(redgreencmap)
title('initial population');
pause(0.1);
njactive = 0; % number of active jumps
for njump = 1:Njump % BEGIN JUMP LOOP
ncell0 = randi(noc);
nyi = cellvec(ncell0,2);
nxi = cellvec(ncell0,3);
% Determine force on cell
f = [0,0]; % force from all neighbors proportional to 1/(r*r)
```

```
nxip1 = nxi+1; if nxip1 > Nx nxip1 = 1; end
nxim1 = nxi-1; if nxim1 < 1 nxim1 = Nx; end
nyip1 = nyi+1; if nyip1 > Ny nyip1 = 1; end
nyim1 = nyi-1; if nyim1 < 1 nyim1 = Ny; end
nocn = 0; % count occupied neighbor cells
ki = 1; % identify initial jump environment
c1 = space(nyim1,nxip1); % possible final position 1
c2 = space(nyi,nxip1); % possible final position 2
c3 = space(nyip1,nxip1); % possible final position 3
c4 = space(nyip1,nxi); % possible final position 4
c5 = space(nyip1,nxim1); % possible final position 5
c6 = space(nyi,nxim1); % possible final position 6
c7 = space(nyim1,nxim1); % possible final position 7
c8 = space(nyim1,nxi); % possible final position 8
if c1 > 0 nocn=nocn+1;
if c1 < 2 f = f + [1,-1]*fc*f1; end
if c1 == 2 f = f + [1,-1]*fc*f2; end
if c1 > 2 f = f + [1,-1]*fc*f3; end
if c1 > ki ki = c1; end
end
if c2 > 0 nocn=nocn+1;
if c2 < 2 f = f + [1,0]*f1; end
if c2 == 2 f = f + [1,0]*f2; end
if c2 > 2 f = f + [1,0]*f3; end
if c2 > ki ki = c2; end
end
if c3 > 0 nocn=nocn+1;
if c3 < 2 f = f + [1,1]*fc*f1; end
if c3 == 2 f = f + [1,1]*fc*f2; end
if c3 > 2 f = f + [1,1]*fc*f3; end
if c3 > ki ki = c3; end
end
if c4 > 0 nocn=nocn+1;
if c4 < 2 f = f + [0,1]*f1; end
if c4 == 2 f = f + [0,1]*f2; end
if c4 > 2 f = f + [0,1]*f3; end
if c4 > ki ki = c4; end
end
if c5 > 0 nocn=nocn+1;
if c5 < 2 f = f + [-1,1]*fc*f1; end
if c5 == 2 f = f + [-1,1]*fc*f2; end
if c5 > 2 f = f + [-1,1]*fc*f3; end
if c5 > ki ki = c5; end
end
if c6 > 0 nocn=nocn+1;
if c6 < 2 f = f + [-1,0]*f1; end
if c6 == 2 f = f + [-1,0]*f2; end
if c6 > 2 f = f + [-1,0]*f3; end
if c6 > ki ki = c6; end
end
if c7 > 0 nocn=nocn+1;
```

```
if c7 < 2 f = f + [-1,-1]*fc*f1; end
if c7 == 2 f = f + [-1,-1]*fc*f2; end
if c7 > 2 f = f + [-1,-1]*fc*f3; end
if c7 > ki ki = c7; end
end
if c8 > 0 nonc=nocn+1;
if c8 < 2 f = f + [0,-1]*f1; end
if c8 == 2 f = f + [0,-1]*f2; end
if c8 > 2 f = f + [0,-1]*f3; end
if c8 > ki ki = c8; end
end
% Determine displacement-energy and -entropy changes
DU = zeros(8,1);
DS = zeros(8,1);
p = zeros(8,2); % track cell numbers and jump probabilities
nx = nxi; ny = nyi; % initial position
Sinitial = myentropy(space,Nx,nx,ny,root2);
space(nyi,nxi) = 0; % jump from here
if c1 == 0
DU(1) = f*[1;-1];
nx = nxip1; ny = nyim1; % final position 1
DS(1) = myentropy(space,Nx,nx,ny,root2)- Sinitial;
end
if c2 == 0
DU(2) = f*[1;0];
nx = nxip1; ny = nyi; % final position 2
DS(2) = myentropy(space,Nx,nx,ny,root2)- Sinitial;
end
if c3 == 0
DU(3) = f*[1;1];
nx = nxip1; ny = nyip1; % final position 3
DS(3) = myentropy(space,Nx,nx,ny,root2)- Sinitial;
end
if c4 == 0
DU(4) = f*[0;1];
nx = nxi; ny = nyip1; % final position 4
DS(4) = myentropy(space,Nx,nx,ny,root2)- Sinitial;
end
if c5 == 0
DU(5) = f*[-1;1];
nx = nxim1; ny = nyip1; % final position 5
DS(5) = myentropy(space,Nx,nx,ny,root2)- Sinitial;
end
if c6 == 0
DU(6) = f*[-1;0];
nx = nxim1; ny = nyi; % final position 6
DS(6) = myentropy(space,Nx,nx,ny,root2)- Sinitial;
End
if c7 == 0
DU(7) = f*[-1;-1];
nx = nxim1; ny = nyim1; % final position 7
```

```
DS(7) = myentropy(space,Nx,nx,ny,root2)- Sinitial;
end
if c8 == 0
DU(8) = f*[0;-1];
nx = nxi; ny = nyim1; % final position 8
DS(8) = myentropy(space,Nx,nx,ny,root2)- Sinitial;
end
space(nyi,nxi) = 1; % jump from here
% Calculate displacement probabilities
if Thermo ~= 0 % with thermodynamic constraints
if Thermo == 1 DA = DU - T*DS;
else DA = -DU - T*DS; end
else DA = zeros(8,1);
end
p(:,1) = exp(-DA/(kB*T));
p(:,2) = 1:8;
if propflag ==1
if c1 ~= 0 p(1,1) = 0; end % exclude occupied destination cells
if c2 ~= 0 p(2,1) = 0; end
if c3 ~= 0 p(3,1) = 0; end
if c4 ~= 0 p(4,1) = 0; end
if c5 ~= 0 p(5,1) = 0; end
if c6 ~= 0 p(6,1) = 0; end
if c7 ~= 0 p(7,1) = 0; end
if c8 ~= 0 p(8,1) = 0; end
end
% Sort displacement probabilities and determine destination-cell number
P = sortrows(p,'descend');
kf = ki;
n1 = 1;
if P(1,1) >= 1 % if no energetic constraints for jump
for nc = 2:8
if P(nc,1) >= 1 n1 = n1+1; end
end
else
for nc = 2:8
if P(1,1) == P(nc,1) n1 = n1+1; end
end
end
ncell = P(randi(n1),2); % randomly pick the destination cell
% Identify destination cell
space(nyi,nxi) = 0; % jump from here *******
if ncell > 0
if ncell == 1 nyi=nyim1; nxi=nxip1; end
if ncell == 2 nxi=nxip1; end
if ncell == 3 nyi=nyip1; nxi=nxip1; end
if ncell == 4 nyi=nyip1; end
if ncell == 5 nyi=nyip1; nxi=nxim1; end
if ncell == 6 nxi=nxim1; end
if ncell == 7 nyi=nyim1; nxi=nxim1; end
if ncell == 8 nyi=nyim1; end
```

```
end
jumpflag = 1; % default: jump is possible
if space(nyi,nxi) ~= 0 % jump not possible
nyi = cellvec(ncell0,2);
nxi = cellvec(ncell0,3);
jumpflag = 0;443 end
space(nyi,nxi) = 1; % jump to there *******

cellvec(ncell0,2) = nyi; % update cell vector
cellvec(ncell0,3) = nxi;
% Display cell population
njactive = njactive +1;
if njactive <= 10
subplot(3,2,1)
heatmap(space);
colormap(redgreencmap)
title(['jump ',num2str(njump)]);
pause(0.1);
end
% Identify destination-cell environment
nxip1 = nxi+1; if nxip1 > Nx nxip1 = 1; end
nxim1 = nxi-1; if nxim1 < 1 nxim1 = Nx; end
nyip1 = nyi+1; if nyip1 > Ny nyip1 = 1; end
nyim1 = nyi-1; if nyim1 < 1 nyim1 = Ny; end
kf = 1;
c1 = space(nyim1,nxip1); if c1 > kf, kf = c1; end
c2 = space(nyi,nxip1); if c2 > kf, kf = c2; end
c3 = space(nyip1,nxip1); if c3 > kf, kf = c3; end
c4 = space(nyip1,nxi); if c4 > kf, kf = c4; end
c5 = space(nyip1,nxim1); if c5 > kf, kf = c5; end
c6 = space(nyi,nxim1); if c6 > kf, kf = c6; end
c7 = space(nyim1,nxim1); if c7 > kf, kf = c7; end
c8 = space(nyim1,nxi); if c8 > kf, kf = c8; end
% Update kinetix matrix
if propflag == 0 k(kf,ki) = k(kf,ki) + 1;
else if jumpflag ~= 0 k(kf,ki) = k(kf,ki) + 1; end
end
if ScanP == 0 % compute noise autocorrelation
if space(Nyc,Nxc) > 0
noise = puc; % default: position autocorrelation
else noise = poc;
end
avspace = avspace + space; % determine mean population map
for ntau = 2:taumax noisevec(ntau-1) = noisevec(ntau); end
noisevec(taumax) = noise; % record noise
for ntau = 1:taumax % update autocorrelation function
acorr(ntau)=acorr(ntau)+noisevec(taumax)*noisevec(taumax+1-ntau);
end
end
end %%%%%% END JUMP LOOP
% Show results
```

```
pco = 100*noc/nc0; % percentage of occupied cells
ksum = sum(sum(k)); % total number of jumps
k = k*100/ksum; % normalize kinetic matrix to % of jumps
disp(num2str(datestr(now,'dd/mm/yy-HH:MM'))); % show date & time
disp(['occupied cells: # ',num2str(noc),', % ',num2str(pco)]);
disp(['# jumps: ',num2str(ksum)]);
disp(['P: ',num2str(Pop),', T: ',num2str(T)]);
asy1 = k(1,2)-k(2,1); asy2 = k(1,3)-k(3,1); asy3 = k(2,3)-k(3,2);
disp(['k12-k21=',num2str(asy1),', k13-31=',num2str(asy2),', k23-
k32=',num2str(asy3)]);
disp('normalized kinetic matrix (number of jumps in %)');499 disp(k);
SLp(2,SLn) = asy1; % wrap up parameter-variation loop
if ScanP == 0
acorr = acorr/ksum;
avspace = avspace*nc0/(ksum*noc);
spacesum = 0;
for ny = 1:Ny
for nx = 1:Nx
if emptypore(ny,nx) == 0 spacesum = spacesum + avspace(ny,nx);
end
end
end
spacesum = spacesum/nc0;
maxocc = 0; % extrema of avspace
minocc = 0;
for ny = 1:Ny % set boundary to 1
for nx = 1:Nx
if emptypore(ny,nx) > 0, avspace(ny,nx) = 0; end
if emptypore(ny,nx) == 0 avspace(ny,nx) = avspace(ny,nx) –
spacesum; end
if avspace(ny,nx) < minocc minocc = avspace(ny,nx); end
if avspace(ny,nx) > maxocc maxocc = avspace(ny,nx); end
end
end
absmax = maxocc;
if -minocc > maxocc absmax = -minocc; end
subplot(3,2,2)
heatmap(avspace);
caxis([-absmax,absmax]);
colormap(redgreencmap)
title('variation of average cell population');
xlabel(['Thermo ',num2str(Thermo),', Pop ',num2str(Pop),', T
',num2str(T),', asy ',num2str(asy3)]);
subplot(3,2,3) % plot autocorrelation function
ylim([0,0.3]); % ****************
plot(acorr);
xlabel('time delay');
ylabel('autocorrelation');
ntau = 2^nextpow2(taumax);
as = fft(acorr,ntau);
ass = complex(zeros(ntau));
```

```
for n = 1:ntau/2 % reshuffle
ass(n) = as(ntau/2 + n);
ass(ntau/2 + n) = as(n);
end
xaxis = zeros(1,ntau);
for n=1:ntau xaxis(n) = n-ntau/2-1; end % xaxis for subplots
ylim([0,0.3]); %****************
subplot(3,2,4) % plot FFT of autocorrelation function
plot(xaxis,real(ass)); % real part
xlabel('frequency');550 ylabel('spectral amplitude');
xlim([-ntau/2-1 ntau/2]);
subplot(3,2,5) % plot FFT of autocorrelation function
plot(xaxis,imag(ass)); % imaginary part
xlim([-ntau/2-1 ntau/2]);
xlabel('frequency');
ylabel('spectral amplitude');
xlim([-ntau/2-1 ntau/2]);
subplot(3,2,6) % plot nothing
avs = zeros(Ny+2,Nx+2);
for nx=1:Nx
for ny=1:Ny
avs(ny+1,nx+1) = avspace(ny,nx);
end
end
surf(avs);
end
end
%%%%%% End parameter-variation loop and show result %%%%%%
if ScanP > 0
x = zeros(SLcount+1);
y = zeros(SLcount+1);
for SLn = 1:SLcount+1
x(SLn) = SLp(1,SLn); % poulation or temperature
y(SLn) = SLp(2,SLn); % asymmetry of exchange matrix
end576 subplot(3,2,2) % plot nothing
plot(nix);
xlabel('nix');
ylabel('nix');
title(['Thermo ',num2str(Thermo),' Pop ',num2str(Pop),' T
',num2str(T),' asy ',num2str(asy3)]);
subplot(3,2,3)
plot(x,y);
if ScanP == 1 xlabel('population density'); end
if ScanP == 2 xlabel('temperature'); end
ylabel('asymmetry in % of total jums');
end
function S = myentropy(space,Nx,nx,ny,root2)
S = 0;
nxp1 = nx+1; if nxp1 > Nx nxp1 = 1; end
nxm1 = nx-1; if nxm1 < 1 nxm1 = Nx; end
nyp1 = ny+1;
```

```
nym1 = ny-1;
if space(nym1,nxp1) == 0 S = S + root2; end
if space(ny,nxp1) == 0 S = S + 1; end
if space(nyp1,nxp1) == 0 S = S + root2; end
if space(nyp1,nx) == 0 S = S + 1; end
if space(nyp1,nxm1) == 0 S = S + root2; end
if space(ny,nxm1) == 0 S = S + 1; end
if space(nym1,nxm1) == 0 S = S + root2; end
if space(nym1,nx) == 0 S = S + 1; end
end
```

C.6 Matlab code for gas-diffusion simulations

```
function [exchangemat,population,asy] =
gasdifsim(speedscale,numparticles,numsteps,dt,diameter,center,numbins)

%%%%% This simulation generates an exchange matrix and population density
%%%%% map for gas particles undergoing elastic collisions. In order the
%%%%% input variables are the scaling factor for the inital velocity
%%%%% profile, the number of particles, the number of time steps, the
%%%%% duration of the time step in arbitrary time units, the diameter of
%%%%% the particles in arbitrary length units, an array of the coordinates
%%%%% for the center of each defect site (i.e. for 7 defects [-0.1 0.1 0.3
%%%%% 0.5 0.7 0.9 1.1], and the number of bins.



%%%%% Initial condition inputs %%%%%

radius(1:numparticles,1) = diameter/2; % same radius for all particles
initialspeed = speedscale.*randn([numparticles 1]);
% each particle has a random initial speed

t = 0; % start time
timearray = (t:dt:(t+dt*numsteps))'; % full time array
step = 1 % iteration step
exchangemat(3,3,numbins+2) = 0;
% creates a set of 3x3 matrices, one for each defect site

bincenter = (1/(2*numbins)):(1/numbins):1;


%%%%% Generates randomized particles %%%%%

%Randomizing initial positions and ensuring no overlap of particles

initialpos = round(rand(numparticles,1)*(numbins^2-1))+1;
for ii = 2:numparticles
while any(initialpos(ii)==initialpos(1:(ii-1)))
```

```
initialpos(ii) = round(rand*(numbins^2-1))+1;
end
end

initialpos = initialpos/numbins;
binx = ceil(initialpos);
biny = round((initialpos-(binx-1))./diameter);

for ii = 1:numparticles
initialx(ii,1) = bincenter(binx(ii));
initialy(ii,1) = bincenter(biny(ii));
end

positionx = initialx; positiony = initialy; % Tracking current positions

theta = 2.*pi.*randn([numparticles 1]); % randomized initial angle of travel
velocityx = cos(theta).*initialspeed; velocityy = sin(theta).*initialspeed;
% x and y velocity components assigned based on random angle calculation

particles = [positionx,positiony,velocityx,velocityy];
% each row defines a particle with initial positions, velocities, and radius
pos2d = [positionx,positiony];
% Tracking both current position components in one array


population = zeros(numbins); % empty matrix to track particle locations at each step
binlimits = [-0.05 (bincenter(2)-bincenter(1)):(bincenter(2)-bincenter(1)):(1-(bincenter(2)-
bincenter(1))) 1.05];
% Boundary definitions for each grid element, total length of x and y
% walls goes from 0 to 1 in arbitrary length units. Each grid element is
% the length of one particle diameter or 1/numbins


% Populates the population density count with the initial positions.
% Takes the inital x and y coordinate of each particle and determines
% which grid element it falls into and updates cooresponding matrix
% element by +1
for pp = 1:numparticles
for ff = 1:(numbins)
for gg = 1:(numbins)
if pos2d(pp,1)>binlimits(ff) && pos2d(pp,1)<=binlimits(ff+1)...
      && pos2d(pp,2)>binlimits(gg) && pos2d(pp,2)<=binlimits(gg+1)
population(ff,gg) = population(ff,gg) + 1;
end
end
end
end


%%%%% Moving the particles %%%%%
```

```
for hh = 1:numsteps %looping through each step

step = step+1 %increment to the next time step
t = t+dt; %current time
collisionpair = [];


% Compares the positions of each possible pair of particles. When
% the coordinates are within 1 particle diameter of each other they
% are considered to have collided. A list of all colliding pairs is
% generated.
for gg = 1:(numparticles-1)
collidingparticle1 = particles(gg,1:2);
for jj = (gg+1):numparticles
collidingparticle2 = particles(jj,1:2);
if norm(collidingparticle2-collidingparticle1) < diameter
collisionpair = [collisionpair;gg jj];
end
end
end

for ll = 1:size(collisionpair,1)

collidingposition1 = particles(collisionpair(ll,1),1:2); % current position of colliding particle 1
collidingposition2 = particles(collisionpair(ll,2),1:2); % current position of colliding particle 2
collidingvelocity1 = particles(collisionpair(ll,1),3:4); % current velocity of colliding particle 1
collidingvelocity2 = particles(collisionpair(ll,2),3:4); % current velocity of colliding particle 2


% Calculation of new velocities for the elastic collision of particles
dr = collidingposition2 - collidingposition1;
dv = collidingvelocity2 - collidingvelocity1;
dvdotdr = dot(dv,dr);
d = norm(dr)^2;

newvelocity1 = collidingvelocity1 - dvdotdr./d.*(collidingposition1-collidingposition2);
newvelocity2 = collidingvelocity2 - dvdotdr./d.*(collidingposition2-collidingposition1);


% Replacing the pre-collision velocities with the
% post-collision velocities
velocityx(collisionpair(ll,1)) = newvelocity1(1); velocityx(collisionpair(ll,2)) = newvelocity2(1);
velocityy(collisionpair(ll,1)) = newvelocity1(2); velocityy(collisionpair(ll,2)) = newvelocity2(2);
particles = [positionx,positiony,velocityx,velocityy];
end

for kk = 1:numparticles
%checking x boundaries, deflect if collision
if ((particles(kk,1) - 0) < radius(1) && velocityx(kk) < 0) ||...
      ((1 - particles(kk,1)) < radius(1) && velocityx(kk) > 0)
velocityx(kk) = -1.*velocityx(kk);
```

```
%checking y boundaries, deflect if collision
elseif ((particles(kk,2) - 0) < radius(1) && velocityy(kk) < 0)...
      || ((1 - particles(kk,2)) < radius(1) && velocityy(kk) > 0)
velocityy(kk) = -1.*velocityy(kk);
end
end


% Move particles to their next position and record
positionx = positionx + velocityx.*dt; positiony = positiony + velocityy.*dt;
particles = [positionx,positiony,velocityx,velocityy];
pos2d((numparticles+1):(2*numparticles),:) = [positionx positiony];




for jj = 1:numparticles

% Update population density matrix with the new positions (see
% line 46)
for ff = 1:numbins
for gg = 1:numbins
if pos2d(jj+numparticles,1)>binlimits(ff) && pos2d(jj+numparticles,1)<=binlimits(ff+1)...
      && pos2d(jj+numparticles,2)>binlimits(gg) && pos2d(jj+numparticles,2)<=binlimits(gg+1)
population(ff,gg) = population(ff,gg) + 1;
end
end
end



%%%%% Counting for the Exhange matrix %%%%%

% Site 1 is in the body of the pore, Site 2 is the wall, and Site 3
% is the defect site.

for defectsite = 1:(numbins+2)

% Particle is found at a Site 3 grid space at previous time step
if (pos2d(jj,1)<diameter && (pos2d(jj,2)<(center(defectsite)+3*diameter/2)...
      && pos2d(jj,2)>(center(defectsite)-3*diameter/2)))

% Particle is still in a Site 3 grid space on current step
if (pos2d(numparticles+jj,1)<diameter &&
(pos2d(numparticles+jj,2)<(center(defectsite)+3*diameter/2)...
      && pos2d(numparticles+jj,2)>(center(defectsite)-3*diameter/2)))
exchangemat(3,3,defectsite) = exchangemat(3,3,defectsite) + 1;

% Particle moved to a Site 1 grid space on current step
elseif (pos2d(numparticles+jj,1)>=diameter && (1-pos2d(numparticles+jj,1))>=diameter)...
      && (pos2d(numparticles+jj,2)>=diameter && (1-pos2d(numparticles+jj,2))>=diameter)
```

```
exchangemat(3,1,defectsite) = exchangemat(3,1,defectsite) + 1;

% Particle moved to a Site 2 grid space on current step
else
exchangemat(3,2,defectsite) = exchangemat(3,2,defectsite) + 1;
end


% Particle is found at a Site 1 grid space at previous time step
elseif (pos2d(jj,1)>=diameter && (1-pos2d(jj,1))>=diameter) && (pos2d(jj,2)>=diameter && (1-
pos2d(jj,2))>=diameter)

% Particle is still in a Site 1 grid space on current step
if (pos2d(numparticles+jj,1)>=diameter && (1-pos2d(numparticles+jj,1))>=diameter)...
&& (pos2d(numparticles+jj,2)>=diameter && (1-pos2d(numparticles+jj,2))>=diameter)
exchangemat(1,1,defectsite) = exchangemat(1,1,defectsite) + 1;

% Particle moved to a Site 3 grid space on current step
elseif (pos2d(numparticles+jj,1)<diameter &&
(pos2d(numparticles+jj,2)<(center(defectsite)+3*diameter/2)...
&& pos2d(numparticles+jj,2)>(center(defectsite)-3*diameter/2)))
exchangemat(1,3,defectsite) = exchangemat(1,3,defectsite) + 1;

% Particle moved to a Site 2 grid space on current step
else
exchangemat(1,2,defectsite) = exchangemat(1,2,defectsite) + 1;
end


% Particle is found at a Site 2 grid space at previous time step
else

% Particle moved to a Site 1 grid space on current step
if (pos2d(numparticles+jj,1)>=diameter && (1-pos2d(numparticles+jj,1))>=diameter) &&
(pos2d(numparticles+jj,2)>=diameter && (1-pos2d(numparticles+jj,2))>=diameter)
exchangemat(2,1,defectsite) = exchangemat(2,1,defectsite) + 1;

% Particle moved to a Site 3 grid space on current step
elseif (pos2d(numparticles+jj,1)<diameter &&
(pos2d(numparticles+jj,2)<(center(defectsite)+3*diameter/2) &&
pos2d(numparticles+jj,2)>(center(defectsite)-3*diameter/2)))
exchangemat(2,3,defectsite) = exchangemat(2,3,defectsite) + 1;

% Particle is still in a Site 2 grid space on current step
else
exchangemat(2,2,defectsite) = exchangemat(2,2,defectsite) + 1;
end
end
end

end
```

```
% Current time step is moved to previous time step for next iteration
pos2d(1:numparticles,:) = pos2d((numparticles+1):(2*numparticles),:);

end


% Heat map for the population density, normalized by the average
% population and centered about 0
figure
heatmap(population./mean(population,'all')-1)
colorbar

for ii = 1:7
asy(ii,1) = (exchangemat(1,2,ii)-exchangemat(2,1,ii)).*100./sum(exchangemat(:,:,ii),'all');
asy(ii,2) = (exchangemat(2,3,ii)-exchangemat(3,2,ii)).*100./sum(exchangemat(:,:,ii),'all');
asy(ii,3) = (exchangemat(1,3,ii)-exchangemat(3,1,ii)).*100./sum(exchangemat(:,:,ii),'all');
end

end
```